DEXTERITY ENHANCEMENT IN MICROSURGERY USING A MICROGRIPPER AND MOTION-SCALING SYSTEM

By

Shyan Ku

B.Eng. (Electrical, Honours) McGill University, 1989

A THESIS SUBMITTED IN PARTIAL FULFILLMENT OF

THE REQUIREMENTS FOR THE DEGREE OF

MASTER OF APPLIED SCIENCE

in

THE FACULTY OF GRADUATE STUDIES

ELECTRICAL ENGINEERING

We accept this thesis as conforming

to the required standard

THE UNIVERSITY OF BRITISH COLUMBIA

April 1996

In presenting this thesis in partial fulfilment of the requirements for an advanced degree at the University of British Columbia, I agree that the Library shall make it freely available for reference and study. I further agree that permission for extensive copying of this thesis for scholarly purposes may be granted by the head of my department or by his or her representatives. It is understood that copying or publication of this thesis for financial gain shall not be allowed without my written permission.

Department of ELECTRICAL ENGINEERING

The University of British Columbia
Vancouver, Canada

Date APRIL 17, 1996

Abstract

The design and control of a six-degree-of-freedom (6-DOF) force-reflecting motion-scaling teleoperation system was presented in [1]. In this thesis, a remotely controlled microgripper is developed as an end-effector for this system. The device features small size and weight, and large stroke and force compared to other designs. A stylus-shaped teleoperation master that measures the force at the fingers of the operator provides an intuitive means for operating the microgripper. This design also enables the microgripper to be used as a hand-held instrument. Force sensing enables the accurate measurement and control of tool-tissue forces, as well as the emulation of different mechanical devices. Issues concerning the design, control, and application to microsurgical tasks are addressed here.

6-DOF force/torque sensing has also been added to the teleoperation system, enabling the use of hand and environment forces to improve teleoperation transparency, and enabling the measurement of forces during microsurgery. Several methods for teleoperation control have been implemented, and their potential use in microsurgery is discussed. In addition, experiments have been conducted to quantify the effects of scaled motion and scaled force feedback on teleoperation performance in tasks involving sub-millimetre motions and contact forces from 3 to 15 grams. Significant improvements in accuracy of task execution as well as operator confidence and fatigue were observed when scaled motion and scaled force feedback were provided.

Table of Contents

List of Tables

List of Figures

Acknowledgements

This work brings together many aspects of previous work on the design and control of high-performance manipulators for robotics and teleoperation, carried out by Tim Salcudean and former graduate students at the Robotics and Control Laboratory. I am greatly indebted to these people for their assistance. Special thanks to Chia-Tung Chen, Tim Vlaar, and Leo Stocco for the discussions, and for the much needed distractions. I am also grateful to research engineers Niall Parker and Alison Taylor for their help throughout.

I would like to express my appreciation to Dr. Betty Pearson for helping me to understand microsurgery, and I would like to thank Donald Dawson, Dave Fletcher, and Leiff Kjolby for their patience, advice, and excellent machining work.

Finally, this research would not have been possible without the ideas, inspiration, encouragement, and support of Tim Salcudean. This work is dedicated to Mariam, my parents, and my sisters who have always given me unconditional love and encouragement. This work was supported by the Science Council of British Columbia.

Chapter 1

Introduction

1.1 Microsurgery

In the past half century, most breakthroughs in microsurgery can be attributed to technological advances in microsurgical instrumentation in conjunction with improved techniques developed by innovative microsurgeons [2]. The operating microscope, microinstruments, and microsutures are a few examples. However, the manual dexterity of the surgeon still poses a great limitation on the range of tasks that can be performed. Hand tremor, fatigue, and lack of kinesthetic feedback are some of the limiting factors.

Presently, hand-held forceps and needle holders are the primary instruments used to grip and manipulate tissues, needles, sutures, and other small objects in microsurgery[1]. In order to control the instruments, a microsurgeon depends primarily on visual information through an operating microscope. However, smooth, accurate sub-millimetre motions are difficult to achieve and even more difficult to sustain over a period of several hours. Furthermore, small tool-tissue forces cannot be felt, making the task of safely manipulating delicate tissues challenging and time intensive.

As a result, maintaining good manual dexterity becomes progressively more difficult during the span of an operation. Imprecise or unnecessary hand and finger motions waste time and energy, and can result in unnecessary trauma to tissues either directly, or indirectly by prolonging the operating time. Therefore, there would be considerable

[1]For those unfamiliar with microsurgery, a brief overview of standard microsurgical instrumentation and practices is provided in Appendix A. A more comprehensive treatment can be found in [2].

merit in any new microsurgical devices that could improve a microsurgeon's ability to perform fine manipulation.

1.2 Teleoperation in Microsurgery

Over the years, several microsurgeons have developed actively powered instruments to perform the functions of traditional instruments such as needle drivers, forceps, and microscissors [3, 4]. However, these electrically, hydraulically, and pneumatically powered hand-held devices, with their added complexity, did not improve the precision or quality of vascular anastomosis [2]. Furthermore, surgeons found the devices awkward to operate, and thus none are currently in mainstream use.

Now, more than two decades later, robotic teleoperation systems have begun to show considerable promise in enabling the manipulation of objects as small as single cells [5] and atoms [6] by scaling down the motions from the operator's hand to the tool tip. Thus, if this motion-scaling teleoperation technology were to become inexpensive and easy to use, it could provide a practical means for improving the scale, precision, and efficiency of fine-motion manipulation in microsurgery and other areas.

1.2.1 Teleoperation Systems

Motion-scaling teleoperation systems have recently been proposed for microsurgery and micro-manipulation. Scaled motion and scaled force feedback offer the ability to control tool motions and "feel" environment forces at a scale not normally possible with conventional instruments.

The "Bimanual Telemicrorobotics System" under development by Charles, Schenker, *et al.* [7, 8] consists of 6-DOF master and slave serial-link manipulators driven by tendons. The system is intended for microsurgical use, providing scaled motion from master to

slave at a factor of up to 3:1. The prototype slave manipulator was reported to have a large workspace (400 cm^3) and a motion resolution around 25 μm. The use of tendons to transmit force and motion makes it possible to have more compact and lightweight manipulators at the operating site. However, the tradeoffs are manifested in actuation mechanism complexity and performance. For example, the compliance of the manipulator is determined to a great extent by the stiction, friction, and other characteristics of the joint and drive mechanisms.

Mitsuishi *et al.* [9] have also developed a teleoperation system intended for microsurgery. The slave manipulator uses a hydraulically actuated x-y-z positioning stage, DC motors, and pantograph linkages. The force-feedback master consists of a series of "rotation rings" mounted on an x-y-z positioning platform actuated by lead screws. Although performance specifications of this system were not reported, there appear to be some drawbacks in its mechanical design. For example, the master is not backdriveable, and would not be capable of producing high-fidelity force or position feedback.

A system developed by Hunter *et al.* [5] was designed to manipulate single living muscle cells under a microscope. Both master and slave manipulators possessed 2-limbs capable of producing motions resembling the pinching of a human thumb and forefinger. Actuation was provided by a dual-stage coarse-fine configuration of electromagnetic and piezoelectric actuators. The workspace of each limb was a sphere of diameter 100 mm for the master, and 1 mm for the slave. The system was designed to enable the operator holding onto the master to control small motions (10 nm) at the slave, and to receive magnified kinesthetic feedback of small forces experienced at the slave (scaled by a factor of up to 10^6).

Another system designed for micromanipulation was developed by Sato *et al.* [10]. The slave robot consists of two manipulators: a 5-DOF work table holding the specimen, and a 2-DOF "arm" equipped with a force sensor. The master is a stylus (resembling a

pencil) whose tip can be lengthened or shortened using a linear actuator built into the body. The tip of the stylus is instrumented with a single-axis force sensor. To control the position of the slave robot, the operator moves the tip of the stylus across the surface of a touch-sensitive panel behind which a stereoscopic display is mounted. The display shows a view through the microscope. The position and orientation of the stylus are estimated from the touch-panel and from images taken by two video cameras. The stylus is easy to use and unencumbered by weight or the long kinematic chain typical of other telerobotic systems. However, the system would have limited application to situations requiring more dextrous manipulation in three-dimensional space. Furthermore, the 1-DOF force feedback is dependent on the grasp and orientation of the operator's hand

These systems offer steadier and more accurate tool positioning and force application than conventional hand-held tools. Areas such as microscopy, micro-machining, and assembly could also benefit from this technology. Other applications should become apparent as the technology matures. For example, a motion-scaling robotic system could also be valuable as a steady "third hand" tool for microsurgery. Recent work has demonstrated the merit of using robotic devices to hold objects such as a laparoscopic camera [11, 12, 13]. In order to provide traction, microsurgeons presently rely on guide sutures anchored in place by lead weights, hemostats (a.k.a. "mosquito clamps"), slits in the background material, cleats in the clamp-approximator, or trained assistants. A "third-hand" tool equipped with interchangeable end-effectors could enable safe traction, retraction, clamping, and manipulation of delicate tissues, particularly for solo-surgery.

1.2.2 Microgripper End-Effectors

In order for teleoperation systems to be practical for tasks such as microsurgery, useful end-effectors must be available. In particular, an end-effector that provides gripping (i.e., a "microgripper") would be essential, since gripping motions are required to hold

and manipulate vessels, tissues, microsutures, microneedles, and other small objects. In existing microgripper designs, sacrifices in size, weight, and performance are quite apparent, and can be attributed mostly to the scarcity of small, lightweight actuators that are capable of producing substantial force with reasonable speed.

For example, many microgripper designs use piezoelectric actuation because of its simplicity, compact size, and ability to produce large forces. However, piezoelectric materials are also relatively heavy and produce very limited motion. Moreover, they require driving voltages typically on the order of several hundred volts, which may be a concern in the operating room. A prototype microgripper developed by Fukuda [14] was reported to produce a maximum of 1 g force over a 390 μm displacement. Another design developed by Maruyama for wire assembly tasks [15] possessed much larger force (60 g) and stroke (3 mm) capabilities at the expense of weight (200 g). One design that became a commercial product, the *Microflex MG-1000* [16], used piezoelectric bimorphs to achieve a relatively large motion range (2 mm), but was limited to 0.4 g gripping force.

Piezoelectric motors offer greater stroke and retain most of the force-to-weight and size-to-weight benefits of piezoelectric actuation. However, actuation is more complicated both mechanically and electronically, and smooth control of gripping force would be difficult with this type of "stepped" actuator. Microgrippers actuated with piezoelectric motors have been proposed by Ikuta *et al.* [17] and Schoenwald *et al.* [18].

Shape-memory alloy (SMA) actuators are extremely light and are capable of exerting relatively large forces when heated with an electric current. However, response speed is severely limited by the rate of ambient heat dissipation. A microgripper actuated by small SMA springs was built by Ikuta [19]. The device weighed 27 g and measured 40 mm in length; however, it could achieve at best a response time of 0.7 s.

Clearly, there is a great need for new actuation technologies that are capable of delivering large force and fast response without imposing impractical constraints in terms of

size and weight. Alternatively, there exists a significant opportunity for innovative design in developing practical microgripper devices that use existing actuation technologies.

1.3 The UBC Motion-Scaling Teleoperation System for Microsurgery

A 6-DOF teleoperation system is being developed at UBC with the objective of providing the microsurgeon with scaled motion and scaled force feedback [1, 20]. The system uses a dual-stage coarse-fine motion architecture to achieve fine-motion teleoperation over a large workspace (see Figure 1.1).

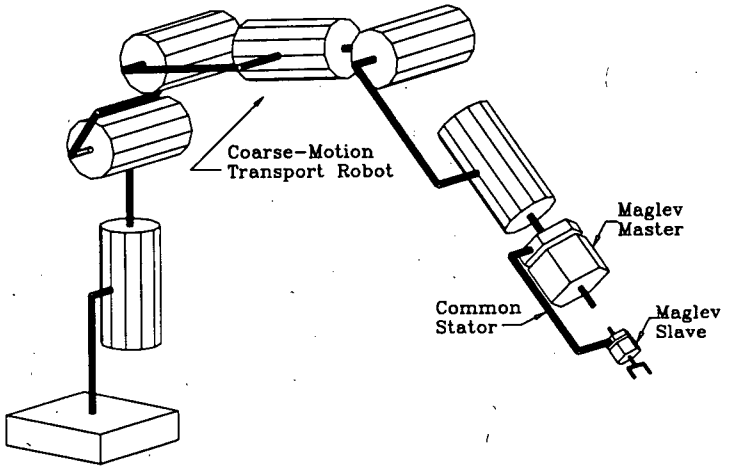

Figure 1.1: UBC Motion-Scaling System for Microsurgery (after Yan [20])

Coarse motion is provided by a 6-DOF robot, and would primarily be used to manoeuvre the fine-motion stage to and from the operating site. The fine-motion stage consists of a hand-held master manipulator and a teleoperated slave manipulator that track each other's motions (see Figure 1.2). With the master manipulator located directly above the slave, the motion-scaling system provides a simple, intuitive surgeon-machine interface in a natural operating environment.

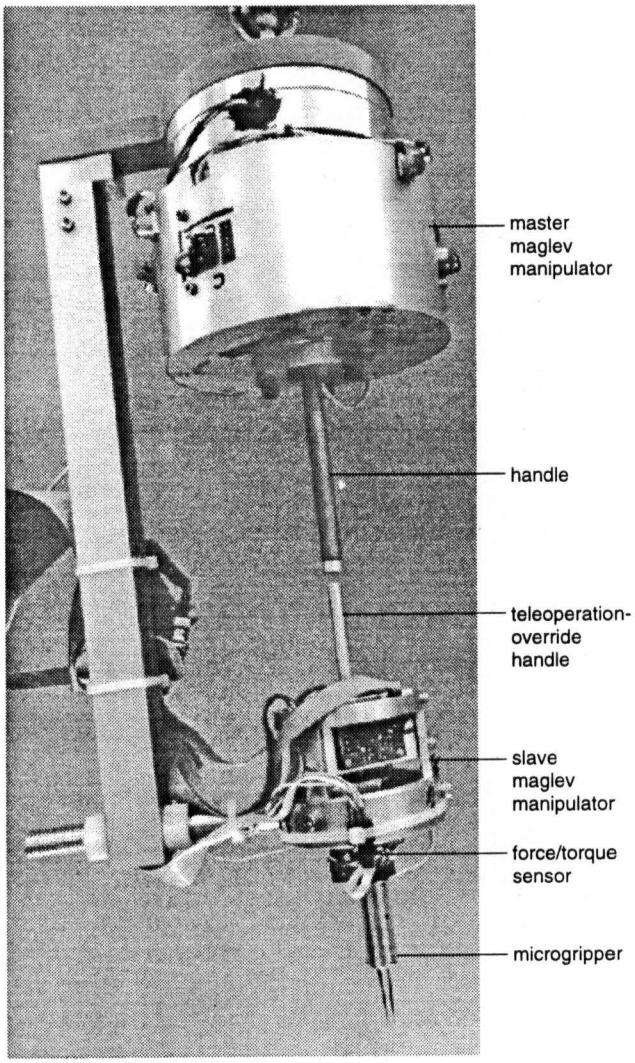

Figure 1.2: Fine-motion stage

Both master and slave manipulators are 6-DOF magnetically levitated (maglev) devices that share a common stator. Figures 1.3 and 1.4 illustrate their design and Table 1.1 lists some characteristics. Each maglev manipulator uses six Lorentz actuators to achieve controllable motion in six degrees of freedom. As illustrated in Figure 1.5, each actuator is composed of a coil located in a magnetic field produced by permanent magnets. The six coils are located on the moving "flotor", and the corresponding permanent magnets are located on the stator. Stator-mounted position-sensing devices ("PSDs"—actually two-dimensional lateral effect photodiodes) are used to locate the light beams emitted by LEDs on the flotor. Flotor position and orientation can then be computed. Although the manipulators possess a limited motion range, they are capable of providing fast, frictionless, high-resolution, backdriveable motion with programmable compliance.

The teleoperation system actively scales motions and forces: motions at the microsurgeon's hand are scaled down to the slave manipulator, and small tool-tissue forces are magnified and fed back to the hand. Position and force scaling factors are programmable, as is digital filtering of undesirable motions such as hand tremor. The motion scaling together with the kinesthetic feedback should enable microsurgeons to achieve better control of fine motions and delicate tool-tissue forces, thereby increasing efficiency, reducing fatigue, and reducing the possibility of damage to tissues.

Coarse-fine motion coordination of the teleoperation system was demonstrated in [20] and previously in [22]. In addition, an H_∞-optimization approach to controller design was proposed to provide teleoperation transparency *vs.* stability robustness tradeoffs [20].

This thesis addresses the issues of end-effector design, teleoperation control, and performance evaluation. A novel microgripper design is presented, and various methods of control are demonstrated here using the working prototype. Force sensing on the microgripper enables the accurate measurement and control of gripping force as well as the

emulation of different useful mechanisms.

Teleoperation control requires both position and force sensing at the master and slave to achieve perfect transparency. Therefore, force sensing has been added to the fine-motion stage of the teleoperation system, and bilateral control using both position and force sensing is demonstrated in six degrees of freedom.

Experiments have been conducted to determine the effects of motion scaling and force scaling on the performance of tasks related to microsurgery. In addition, performance in microsurgery can be evaluated by measuring the actual instrument motions and tool-tissue forces during microsurgery. This would help to identify areas where unnecessary force or motion have been used, and would also provide a better understanding of microsurgery.

Table 1.1: Maglev Manipulator Characteristics

UBC Maglev Manipulators	*Master*	*Slave*[1]
Flotor Mass	630 g	35 g
Flotor Dimensions:		
Diameter	130 mm	70 mm
Height	110 mm	60 mm
Nominal Motion Range:		
z translation	±4.5 mm	±2.25 mm
x and y translation	±4.5 mm	±1.7 mm
z rotation	±7 °	±10 °
x and y rotation	±7 °	±4 °
Single Actuator:		
Max. continuous current:	3 A	0.8 A
Force/Current	2 N/A	1.15 N/A
Max. continuous axial force	18 N	2.8 N
Force Bandwidth	3.7 kHz	32 kHz
Position Resolution	5 μm	1.0 μm
Force Resolution	0.1 N	0.001 N

[1] with permanent magnets added to the stator core

1.4 Thesis Overview

The structure of this thesis is as follows:

- Chapter 2 describes the design of the new microgripper;
- Chapter 3 demonstrates some practical methods for microgripper control, describes the force sensing that has been added to the fine-motion stage of the teleoperation system, and demonstrates several different controllers that have been implemented in six degrees of freedom;
- Chapter 4 describes several experiments that provide an evaluation of teleoperation performance during simulated microsurgical tasks, as well as a better understanding of the motions and forces used in microsurgery;
- finally, Chapter 5 summarizes the contributions of this work, and outlines some directions for future work.

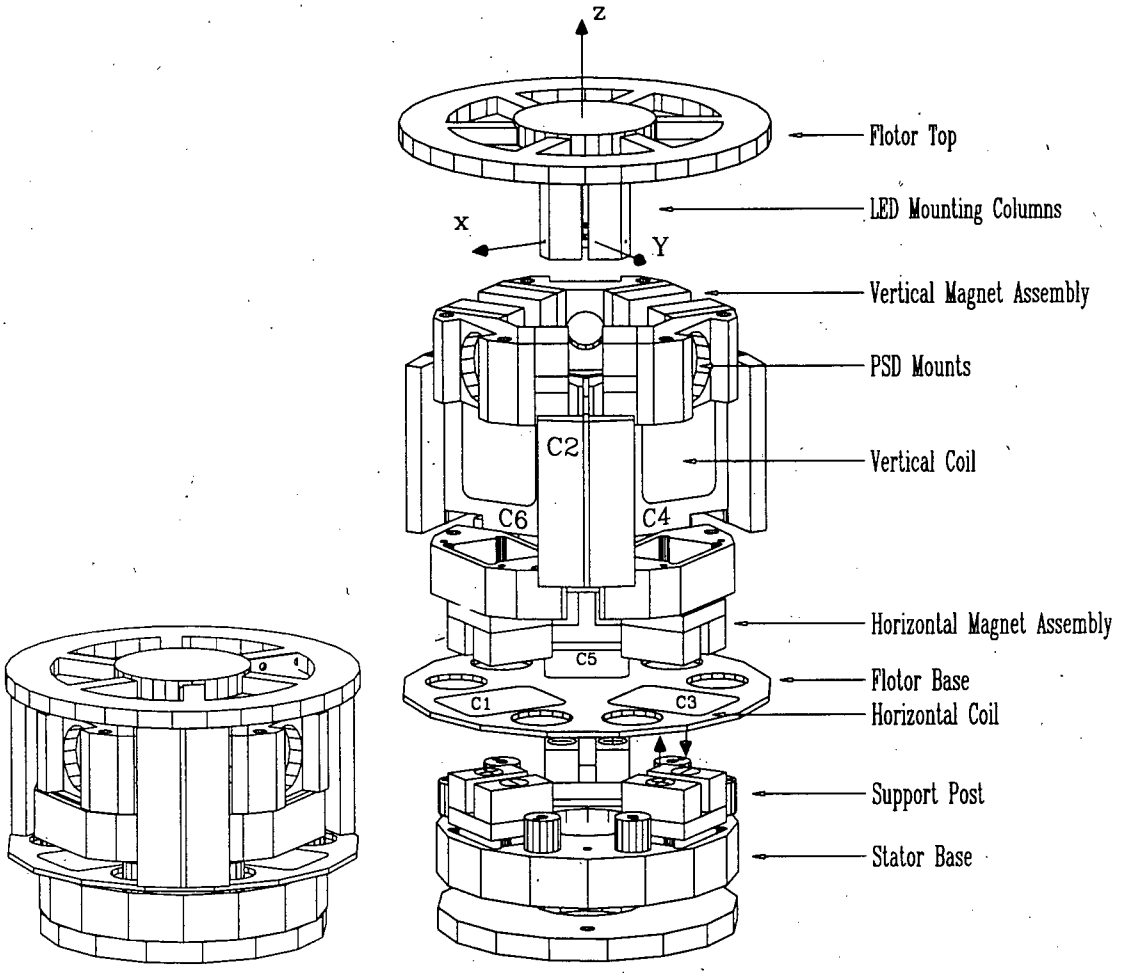

Figure 1.3: Master maglev manipulator (after Chen [21])

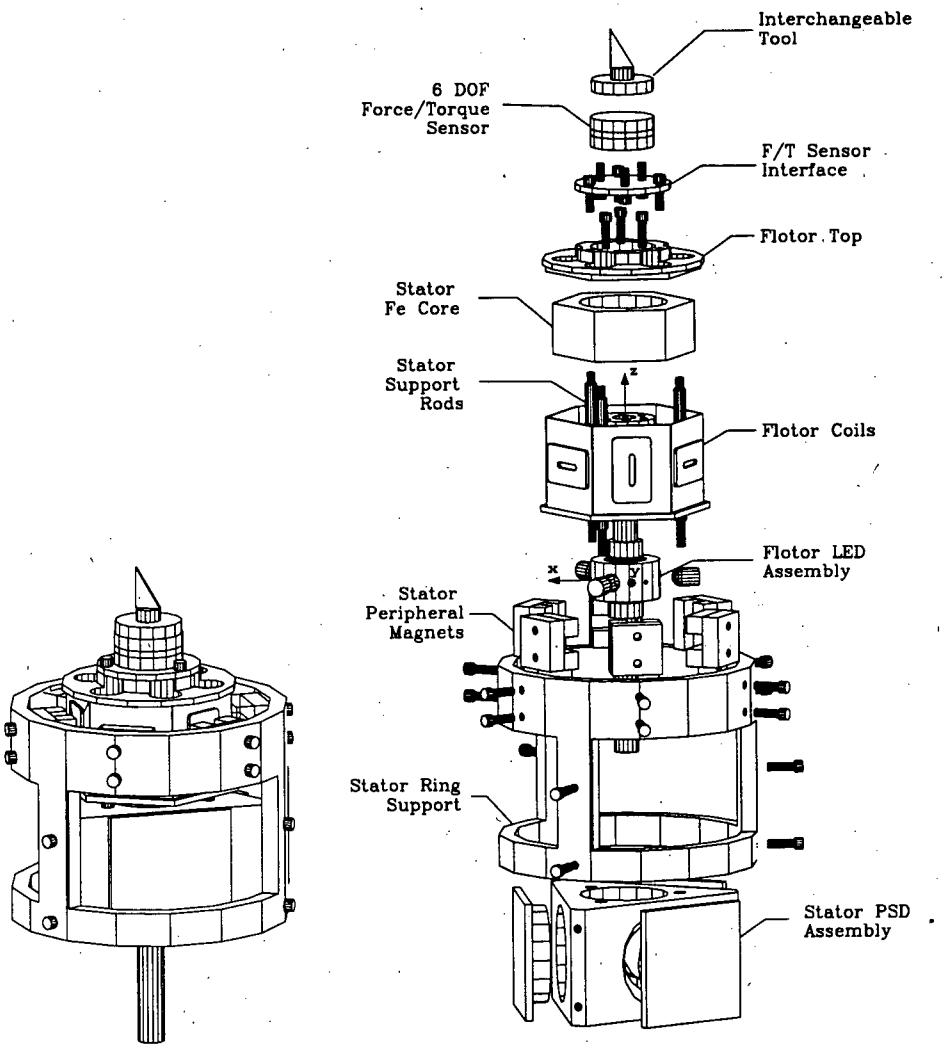

Figure 1.4: Slave maglev manipulator (after Yan [20])

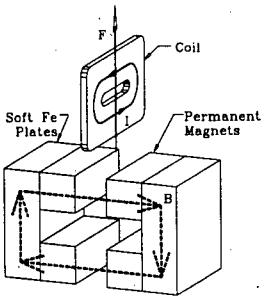

Figure 1.5: Lorentz actuator (after Yan [20])

Chapter 2

Microgripper Design

2.1 Requirements

A remotely operated microgripper has been developed as an end-effector for the motion-scaling teleoperation system developed at UBC. This chapter gives an overview of the requirements and a description of the new microgripper design. The requirements can be categorized into three main areas: mechanical design, performance, and safety.

2.1.1 Mechanical Design

The microgripper must be compact in order to minimize the obstruction of the operating site. Its size must also be minimized because the amount of force applied at the tool tip and the ability to control this force decrease as the tool tip is displaced from the actuators of the slave maglev manipulator. The microgripper must also be lightweight, and any mechanical couplings (e.g., wiring or tubing) must be designed such that mechanical loading of the maglev slave manipulator is minimized.

2.1.2 Performance

The microgripper must possess a motion range close to the 0–4.5 mm of conventional microsurgical forceps (e.g., *Dumont* #5). With respect to gripping force, a previous study of vitreoretinal microsurgery reports typical tool-tissue forces up to 16 grams [23]. In addition, the commonly used *Acland* vascular clamp is available with a clamping force of

10, 15, or 25 grams. Therefore, the microgripper must be capable of producing a similar range of forces, and should be equipped with sensors to enable accurate measurement and control of this force. The actuation method used must enable smooth and easy control over gripping motion and force.

Slow response and time delay have detrimental effects on teleoperation performance. Therefore, an operating bandwidth comparable to the bandwidth of human finger motion typically exercised in microsurgery would be desirable. It is expected that a bandwidth of 5 to 10 Hz should provide adequately fast response.

2.1.3 Safety

Actuation should not produce any electrical, electromagnetic, thermal, or other type of interference with body potentials, instrumentation, or general safety. In addition, the parts of the microgripper that could come into contact with living tissue must be made of materials that are not harmful and that would not react adversely to substances or environmental conditions normally encountered in microsurgery. Furthermore, particles or substances must not be released into the environment. International standards and guidelines for biocompatibility can be found in [24] and [25].

In order for the microgripper to be used safely on living tissue, it must be sterilizable, and its materials and performance must not be adversely affected by the sterilization process. Here, it shall be assumed that a sterility assurance level (SAL) of 10^{-6} is required. This means that the probability of a microbial contaminant (bioburden) surviving is no more than 10^{-6}. An overview of current sterilization methods is given in Appendix B.

2.2 New Design

A new microgripper design has been developed in order to meet the requirements of the present application. The design is compact, lightweight, and scalable. Stroke and force are relatively high compared to other designs, and control of gripping force is fast and simple. The microgripper employs a flexural suspension and a single unidirectional actuator to achieve bilateral gripping action (see Figure 2.1). Two actuation methods have been investigated: a miniature solenoid actuator, and an enclosed hydraulic transmission. The hydraulic transmission system uses miniature electro-formed nickel bellows and flexible tubing (see Figure 2.2). This actuation method is simple, lightweight, and compact, and possesses the additional advantage of being self-contained, requiring no external power sources.

Although the master and slave bellows are mechanically coupled, the motion of the operator's hand could be decoupled from the system by using a conventional actuator to squeeze the master bellows. Majima and Matsushima describe a 1-DOF teleoperation system that uses a hydraulic transmission system to transmit motion from a D.C. motor to a microgripper, in order to measure mechanical properties of different tissues [26]. A tendon-driven microgripper (see Figure 2.1) could be used in a similar manner to distinguish tissues possessing different mechanical properties during minimally invasive surgery (MIS). This could facilitate tasks such as the location of the ureter in laparoscopic hysterectomy operations, since laparoscopic surgeons, like microsurgeons, receive virtually no kinesthetic feedback of the tissues that they manipulate.

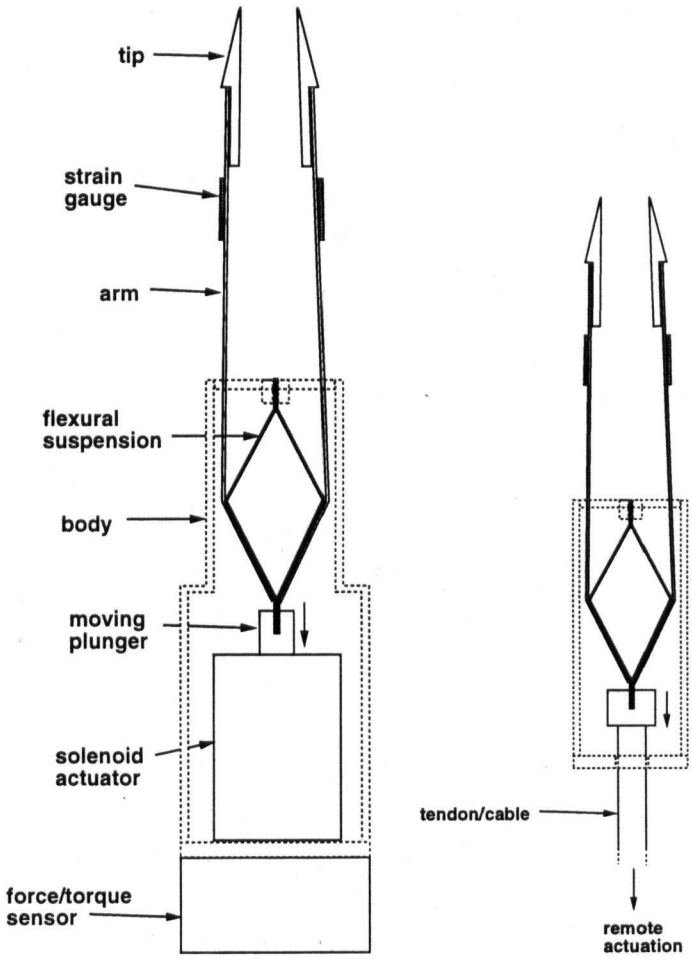

Figure 2.1: Microgripper actuated by solenoid (left) or tendon (right); cross-sectional views

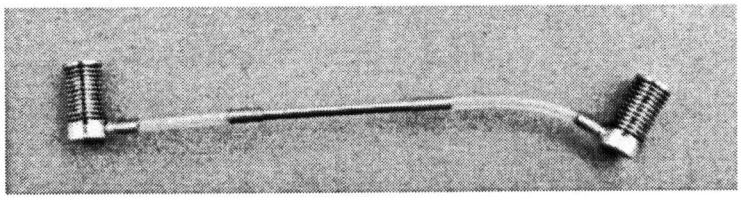

Figure 2.2: Hydraulic actuation/transmission system

2.3 Flexural Suspension

The microgripper design relies on the diamond-shaped flexural suspension to provide friction-free translation and amplification of unidirectional motion from a single linear actuator into symmetric, bilateral gripping motion. The next sections provide a description of its kinematics and an examination of its bending characteristics.

2.3.1 Kinematics

The microgripper is a planar mechanism. As a first approximation, the flexural suspension and gripper arms are modelled as rigid links (see Figure 2.3). The actuator pulls on the flexural suspension at point O, causing the point P to trace a small arc about O. The lever arm L amplifies this motion to the tip of the gripper arm. In the case where $l = m$ $(\theta = \phi)$,

$$\Delta z = 2l(\cos\phi - \cos\phi_0) \tag{2.1}$$

$$\Delta D = L\sin(\phi - \phi_0) \tag{2.2}$$

and it can be shown that

$$\Delta D = -\frac{1}{2}\left(\frac{L}{l}\right)\left(\frac{\cos\frac{\phi-\phi_0}{2}}{\sin\frac{\phi+\phi_0}{2}}\right)\Delta z \quad . \tag{2.3}$$

At rest, $\phi = \phi_0$, and this becomes

$$\Delta D = -\frac{1}{2}\left(\frac{L}{l}\right)\left(\frac{1}{\sin\phi_0}\right)\Delta z \quad . \tag{2.4}$$

As ϕ_0 decreases, $\frac{\Delta D}{\Delta z}$ increases; i.e., position gain increases with smaller angles. However, at smaller angles, greater force is also required to overcome the stiffness of the

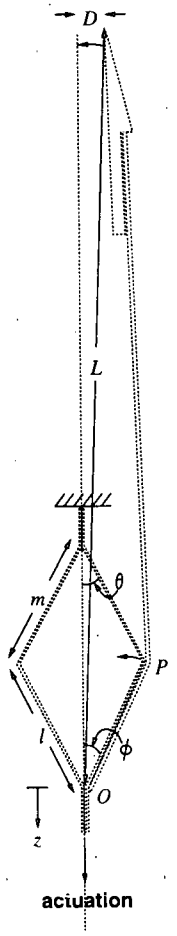

Figure 2.3: Microgripper kinematics

material. Therefore, the force capability of the actuator affects the choice of ϕ_0. This tradeoff of position gain *vs.* force also affects the choices of l, m, and L. Furthermore, as the actuator pulls on the flexural suspension, z increases, ϕ and θ decrease, and greater force is required to further extend the flexural suspension. As will be seen in Section 2.4, this characteristic matches well with the force-displacement properties of a solenoid actuator. Table 2.1 gives the dimensions of the flexural suspension that was used for the microgripper prototype.

Table 2.1: Microgripper characteristics

UBC Microgripper	
Mass	5.4 g
Dimensions:	
Length	45 mm
Diameter at base	12.5 mm
Flexural suspension:	
Material	Brass
Thickness	0.06 mm
Dimensions:	
$l = m$	5 mm
$\phi_0 = \theta_0$	30 °
L	25 mm
Max. gripping force:	
Continuous	10 g
Peak	20 g
Tip displacement	0 – 2.5 mm

2.3.2 Bending Characteristics

The previous section discussed the motion required by the actuator to produce a particular displacement at the microgripper tips. In order to know how much actuation force is needed to produce this motion, it is important to understand the bending behaviour of the flexural suspension. Several flexural suspensions of different dimensions were constructed, and traditional flat-spring design equations were used to model their bending characteristics.

Each half of the flexural suspension can be modelled as a combination of three curved flat springs (see Figure 2.4). Once one half has been modelled, its mechanical stiffness can be combined (in parallel) with the other half to obtain the stiffness of the overall structure. The flat spring model used is shown in Figure 2.4, and was originally referred to by Palm and Thomas as a "type B" spring [27]. *Spring2* clearly falls into this category;

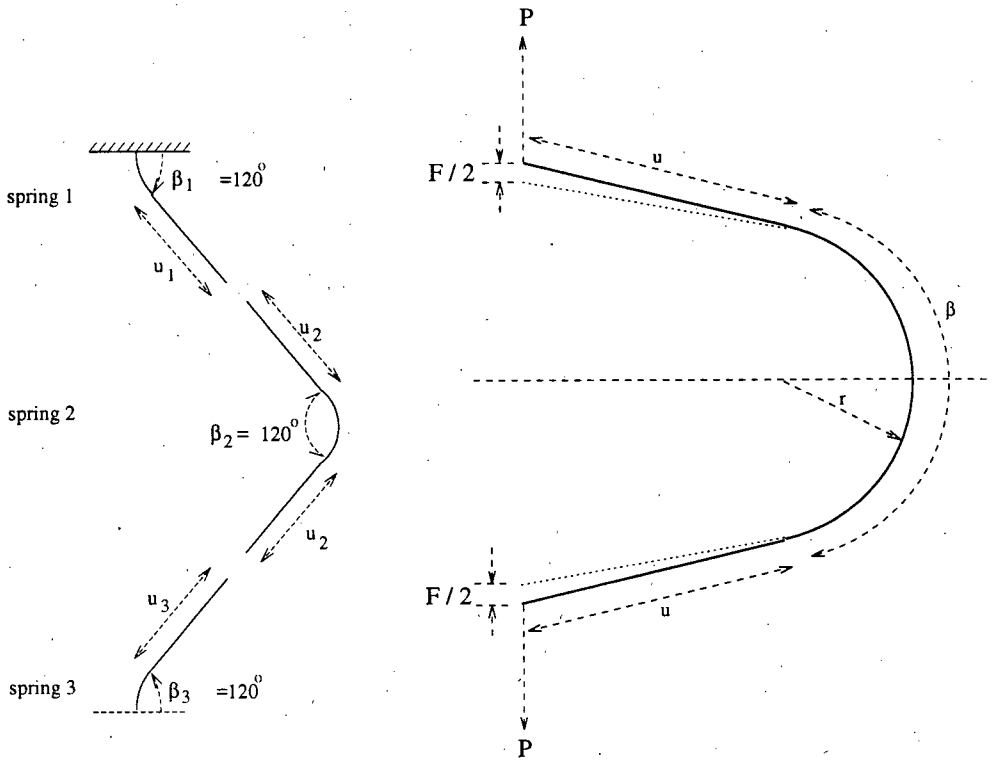

Figure 2.4: Half of the flexural suspension (left) modelled as a combination of curved "type B" springs (right)

spring1 and *spring3* are each simply half of a "type B" spring.

In the spring model, the load P is applied to the lever arms as shown in Figure 2.4, resulting in a displacement F in the direction of the applied load. Two parameters describe the curve in the spring: angle of curvature, β, and radius of curvature, r. For all flexural suspensions tested, $\beta_1 = \beta_2 = \beta_3 = 120°$(refer to Figure 2.4). The length of the straight segments are denoted by the variable u. For the sake of consistency, the naming convention of all variables used here follows that used in [27]. According to this model, the deflection of a "type B" spring should follow

$$F = \frac{2KPr^3}{3EI}(m + \frac{\beta}{2})^3 \tag{2.5}$$

and the deflection of *spring1* and *spring3* should simply be half of this. The following is a description of the variables used:

β is the angle of curvature in radians;

r is the radius of curvature;

u is the length of the straight section;

$m = u/r$;

h is the thickness of the spring material;

b is the width of the spring material;

P is the applied force;

F is the deflection;

E is Young's modulus;

I is the moment of inertia;

and K is the "correction factor".

The general definition of the correction factor, K, is given as

$$K = \frac{0.333m^3 + (m^2 + 0.5)\alpha + 2m(1 - \cos\alpha) - 0.25\sin(2\alpha)}{0.333m^3 + m^2\alpha + m\alpha^2 + 0.333\alpha^3} \tag{2.6}$$

where $\alpha = \beta/2$ for "type B" springs [27].

For the three springs, (2.5) simplifies to

$$\begin{aligned} F_2 &= \frac{2KP}{3EI}(u + \frac{\beta}{2}r)^3 \\ F_1 = F_3 &= \frac{F_2}{2} \end{aligned} \tag{2.7}$$

Since the material is rectangular in cross-section, $I = bh^3/12$, (2.7) becomes

$$F_2 = \frac{8KP}{Ebh^3}(u + \frac{\beta}{2}r)^3 \quad . \tag{2.8}$$

The total displacement of all three springs connected in series is

$$\begin{aligned} F_{half} &= F_1 + F_2 + F_3 \\ &= 2F_2 \\ &= \frac{16KP}{Ebh^3}(u + \frac{\beta}{2}r)^3 \quad , \end{aligned} \tag{2.9}$$

and the mechanical stiffness is $k_{half} = P/F_{half}$. Thus, the overall stiffness of both halves of the flexural suspension combined in parallel is:

$$k = 2k_{half} \quad . \tag{2.10}$$

Four flexural suspensions were constructed, and their force-displacement profiles were measured using a z-positioning stage and force sensor. One end of the flexural suspension was attached to the positioning stage, and the other end was attached to the sensor. As the flexural suspension was extended, its displacement and pulling force were recorded.

In each of the four flexural suspensions tested, the curvatures of all bends were approximately equal in radius ($r_1 = r_2 = r_3$), and u was taken to be 2.2 mm. All were constructed from brass shim stock ($E = 17.0 \times 10^6$ psi). Other physical characteristics are listed in Table 2.2.

Table 2.2 shows the values of mechanical stiffness measured experimentally, as well as those predicted by the flat spring model. Error in the expected results could be attributed to inaccurate modelling of the physical characteristics of the flexural suspension. For instance, since (2.9) is dependent on h^3 and u^3, the results are very sensitive to small modelling errors in these two parameters. Table 2.2 shows that a 10% increase in h and

Table 2.2: Stiffness of Flexural Suspensions (Brass)

Test	h (in)	r (in)	b (mm)	k (g/mm) *Measured*	*Predicted*	*Predicted*[1]
k_1	0.003	0.003	2.8	331	157	279
k_2	0.002	0.006	2.8	190	42	73
k_3	0.002	0.002	2.8	124	48	86
k_4	0.002	0.002	2.5	77	43	77

[1] h increased by 10%, and u decreased by 10%

a 10% decrease in u yield results much closer to those measured experimentally. Since $u >> \frac{\beta}{2}r$ here, small changes in β and r have much less influence on the results.

2.4 Actuation

A prototype microgripper that uses solenoid actuation has been built, and is shown in Figure 2.5. A miniature solenoid actuator was chosen because of its light weight, small size, rectilinear motion, and relatively high force capabilities. The *Electro-Mechanisms PO-25* weighs 2.8 grams, is readily available for under $10, and could be easily sterilized using dry heat. The actuator is shown in Figure 2.6, and its characteristics are summarized in Table 2.3. At full voltage, stray magnetic fields at the microgripper tips were measured to be 0.5 G, and did not interfere with steel microsuture needles.

The actuator is a unidirectional, variable-reluctance device whose force depends on the position of the plunger. With constant current, the pulling force of the actuator increases as the plunger approaches the end plug. However, a return spring of a certain stiffness can be used to oppose the motion of the plunger, making it possible to achieve repeatable bidirectional motions (refer to Figure 2.7).

The force-displacement profiles of the solenoid actuator and the flexural suspension were individually measured using a z-positioning stage and a force sensor. Figure 2.8

shows the stiffness curve of the flexural suspension superimposed on the region of the force-displacement curve of the actuator that was used for the prototype microgripper. This 0.3 mm region corresponds to an offset of the plunger from the end plug by 0.32 mm (when at rest), and the measurement of z as shown in Figure 2.7. Once the flexural suspension is joined to the plunger, the resulting usable force would be as indicated in Figure 2.8.

This solenoid force along with the geometry of the flexural suspension determine the resulting gripping force exerted at the microgripper tips. The resulting force gain is inversely proportional to the position gain provided by the flexural suspension. As the tips of the microgripper close together, position gain increases, and force gain decreases. In the case of the microgripper described in Table 2.1, the position gain at $\phi = \phi_0$ is given by:

$$\frac{\Delta D}{\Delta z} = -\frac{L}{l} = -5 \quad . \tag{2.11}$$

Therefore, at this position, the gripping force (at maximum solenoid voltage) would be $75/5 = 15$ g. The maximum continuous gripping force of the prototype microgripper was measured to be 10 g, as shown in Table 2.1. This difference could be due to imprecise positioning of the solenoid actuator, resulting in a plunger offset (at rest) different from the required 0.32 mm.

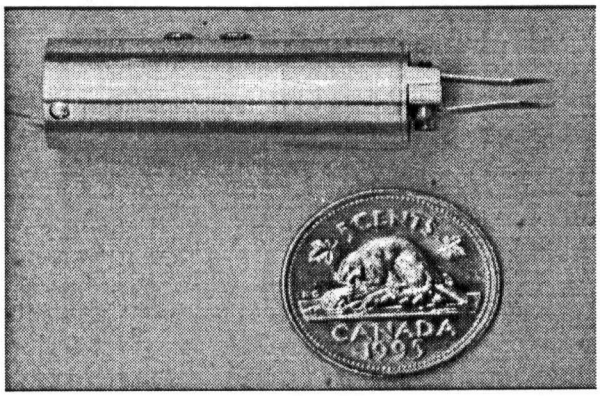

Figure 2.5: Solenoid-actuated microgripper

Figure 2.6: Solenoid actuator: plunger (left) and coil (centre)

Table 2.3: Solenoid Actuator Characteristics

EMI PO-25 Miniature Solenoid Actuator	
Mass	2.8 g
Dimensions:	
Length (without plunger)	13.9 mm
Width	6.0 mm
Height	7.6 mm
Max. voltage (100% duty cycle)	3.0 V
Power consumption at max. voltage	2.0 W
Holding force at max. voltage[1]	220 g
Max. temperature	180 °C

[1] plunger located against end plug

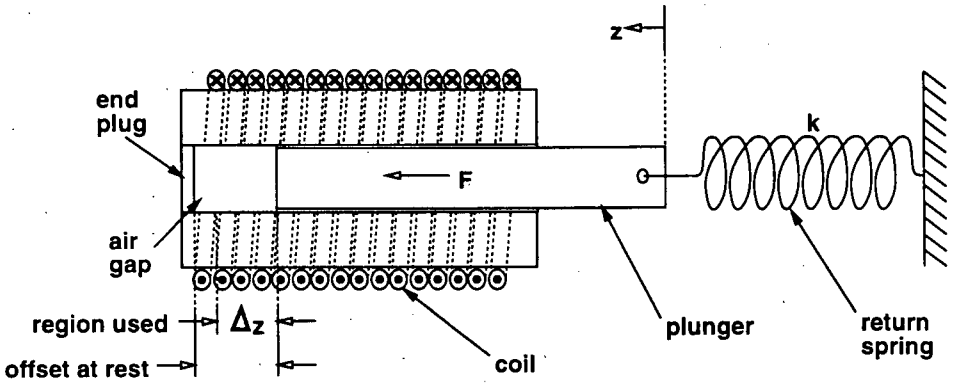

Figure 2.7: Solenoid actuator with return spring

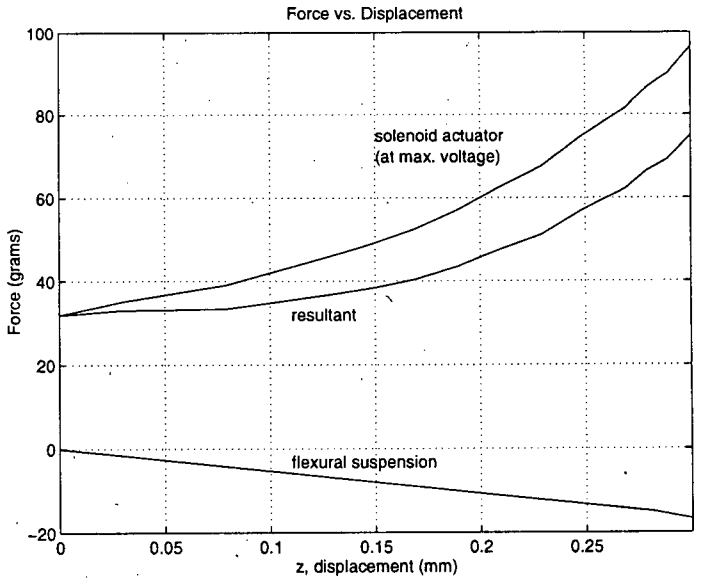

Figure 2.8: Force *vs.* Displacement for solenoid actuator and flexural suspension

2.5 Sensing

Gripping force is measured using metal-foil strain gauges (refer to Figure 2.1). Each gauge forms one arm of a lead-wire temperature-compensated quarter-bridge arrangement, with the strain signal amplified by an instrumentation amplifier circuit (see Figure 2.9). Resistance values used were as follows: $R_g = 350\ \Omega$, $R_0 = 350\ \Omega$, $R = 5.11\ k\Omega$, $R_1 = 500\ k\Omega$, $R_2 = 523\ k\Omega$, $R_3 = 5.11\ k\Omega$, and $R_4 = 523\ k\Omega$.

In order to further reduce the affects of temperature on strain measurements, the bridge excitation is pulsed; i.e., using a positive square wave with a 7.25% duty cycle. This is achieved through software by pulsing one channel of the DVME-628 D/A board, and buffering this signal using an op-amp voltage-follower circuit (see Figure 2.10). Gripping force was calibrated by hanging known weights off the tip of each microgripper arm, and steady-state bias in the sensor signals was removed in the real-time software using a periodic nulling procedure.

The microgripper and miniature force/torque sensor have been wired with 34 AWG silicone-jacketed ribbon cable in order to reduce mechanical loading on the flotor of the slave manipulator. For details on wiring and interface issues, please refer to Appendix C.

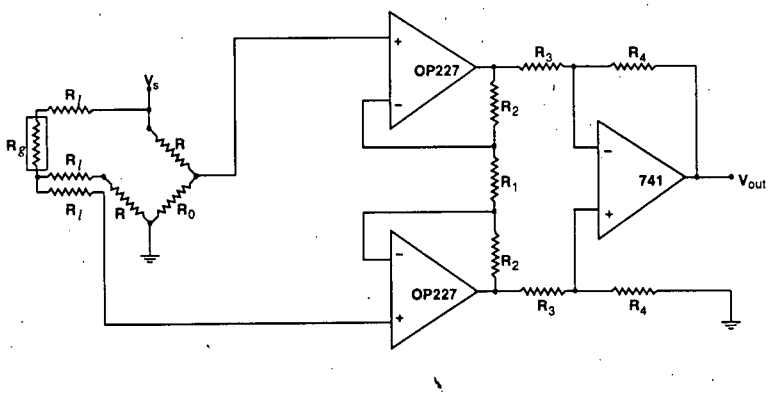

Figure 2.9: Strain gauge signal conditioning schematic

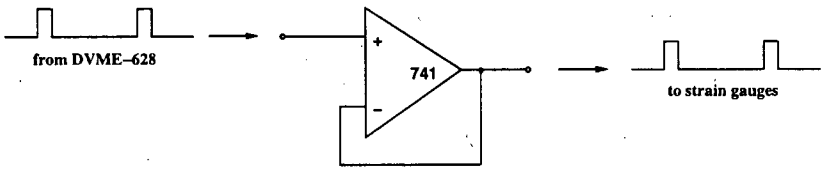

Figure 2.10: Pulsed strain gauge excitation

2.6 Microgripper Master

In order to remotely control the gripping motion of the microgripper, a tool handle that senses the force of the microsurgeon's grasp has been built (see Figure 2.11). Held like a pencil, it provides an intuitive surgeon-machine interface that can be mounted either directly onto the base of the microgripper for a hand-held instrument (Figure 2.12), or onto the master manipulator for motion scaling in six degrees of freedom (Figure 1.2).

The handle uses one strain gauge mounted on a stiff stainless steel beam to measure the gripping force at the surgeon's fingers (see Figure 2.13). Its characteristics are listed in Table 2.4. Because the handle provides a stiff interface to the fingers, it should enable steadier finger force with reduced fatigue [28]. Furthermore, the mechanical decoupling of the surgeon's finger motion from that of the microgripper makes it possible for the surgeon to employ different grasps of the tool, enabling control of the instrument over a much greater motion range. Conventional forceps limit the positions of the thumb and forefinger to a 180° configuration, although some manufacturers have attempted to compensate for this by incorporating rounded handles and other design modifications into their instruments [29].

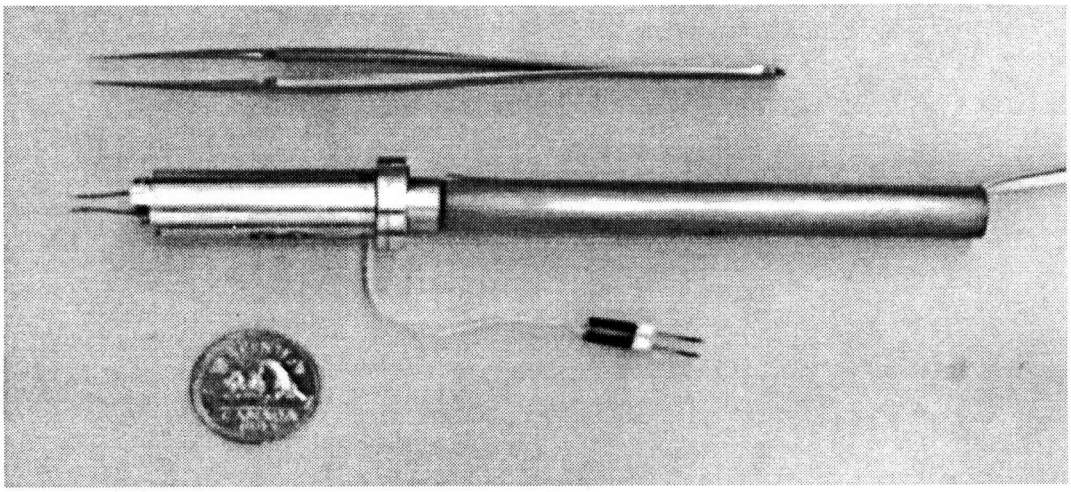

Figure 2.11: Hand-held microgripper and conventional forceps

Table 2.4: Microgripper master characteristics

Microgripper Master	
Mass	20 g
Dimensions:	
Length	90 mm
Diameter	9.5 mm
Force sensing:	
Finger force measured	0 – 150 g
Finger force used	10 – 100 g
Finger travel	0 – 1.25 mm

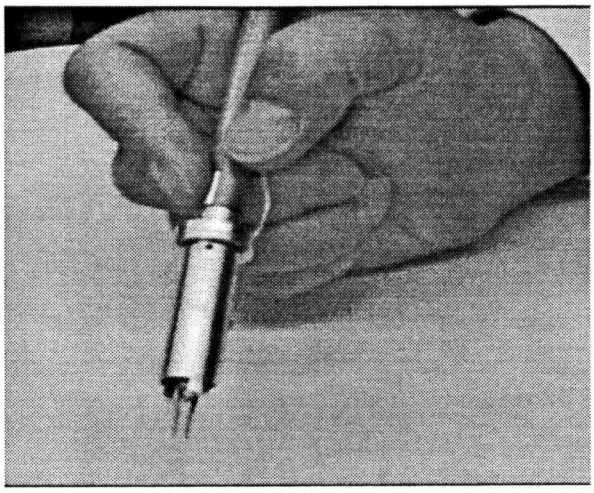

Figure 2.12: Hand-held microgripper

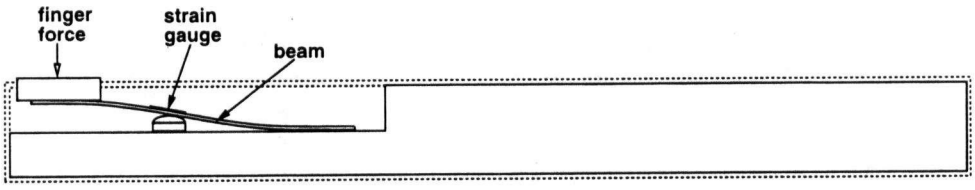

Figure 2.13: Microgripper master

Chapter 3

Control

3.1 System Overview

Real-time control of the microgripper and motion-scaling teleoperation system is performed by software that executes on a SPARC-1e CPU which resides on a VME bus along with various interface boards. The CPU operates under VxWorks, a real-time operating system (OS). For additional resources such as a shared filesystem, the CPU is networked to a SPARCstation host, on which all software development is performed. Figure 3.1 illustrates the hardware configuration. Real-time control follows a *sensing–control–actuation* cycle:

Sensing Strain gauges measure gripping force at the microgripper and master; PSDs measure the position of each maglev manipulator; and a force/torque sensor measures environment forces at the slave manipulator. Signals from the strain gauges and PSDs are simultaneously sampled and held (S/H), and then converted into digital form using an analog-to-digital (A/D) conversion board. At the same time, signals from the force/torque sensor are sampled and converted, and the digital data is transmitted to the CPU via a digital input/output (DIO) board (note: the interface between the force/torque sensor and the DIO board is described in more detail in Appendix C).

Control Software executing on the real-time CPU uses the measurements to determine the amount of current to supply to each actuator.

Actuation The desired currents are converted to analog voltages using digital-to-analog (D/A) conversion boards. The resulting signals are used to control the current amplifiers that supply current to each actuator.

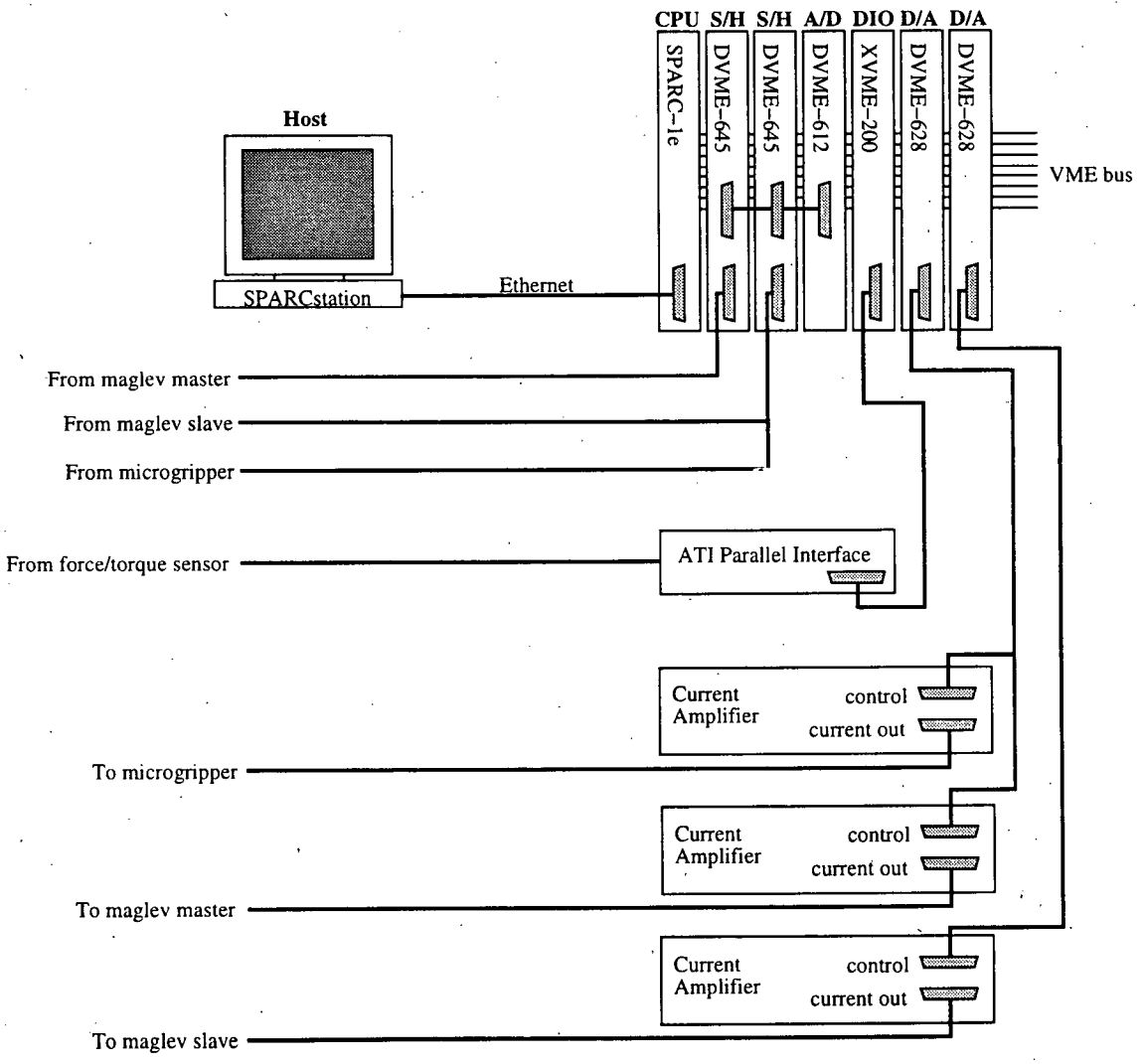

Figure 3.1: Hardware Configuration

3.2 Microgripper Control

3.2.1 Open-Loop Control

Simple open-loop control of the microgripper has been implemented as shown in Figure 3.2. Digital signal conditioning of the finger force, F_{master}, consists of deadband and low-pass filter functions. A current directly proportional to F_{master} drives the solenoid actuator of the microgripper. Open-loop shaping of this F_{master}-to-current relationship could also be done. The resulting solenoid force is balanced by the flexural suspension, resulting in an equilibrium position of the gripper arms.

A programmable scaling factor, n_g, enables the translation of large finger forces into small microgripper motions and forces. This down-scaling of force from the surgeon's fingers, together with the deadband and low-pass filtering, reduces the affects of hand tremor on tool motion. This alone could decrease the possibility of slippage or unintentional application of excessive gripping force. Figure 3.3 shows the finger force and the resulting gripping force when the microgripper controlled in open-loop was used to grip and release a piece of surgical tubing. The scaling factor, n_g, was set to 0.05.

Closed-loop position control is unnecessary since the microgripper would be used under an operating microscope, with the visual feedback of the microsurgeon closing the control loop. However, the relationship between finger force and gripping force depends on the mechanical compliance of the object being held. Moreover, it is difficult to judge tool-tissue forces from visual information alone. Therefore, a hybrid control scheme that uses open-loop position control and closed-loop force control has been implemented.

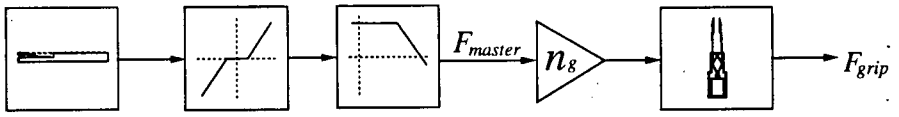

Figure 3.2: Open-loop control

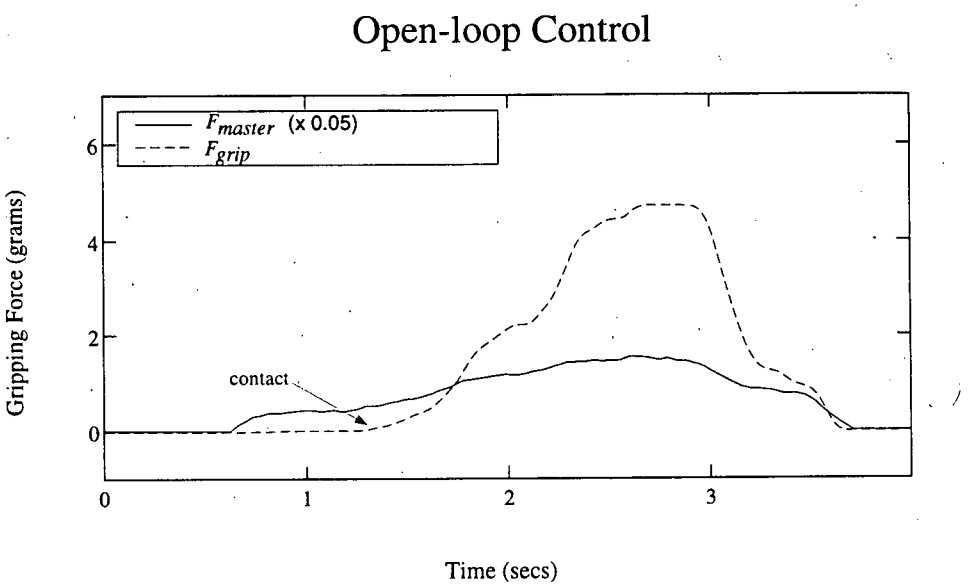

Figure 3.3: Gripping force under open-loop control

3.2.2 Hybrid Control

The hybrid controller uses open-loop control when the microgripper is in free motion, and uses a closed-loop PID control approach to enforce force tracking during contact. To obtain a smooth transition between the two control modes, the controller uses a linear combination of open-loop and closed-loop control, as shown in Figure 3.4.

The weighted contributions of open-loop and closed-loop control are determined by the weighting factors, w_o and w_c. If the gripping force F_{grip} is less than $F_{contact}$, the threshold of the deadband in Figure 3.4, then $w_c = 0$ and $w_o = 1$; therefore, open-loop control is employed when the microgripper is in free motion. As the gripping force increases beyond the contact threshold, the contributions from open-loop and closed-loop control are shifted until eventually, w_c saturates at 1, and $w_o = 0$. Therefore, during contact, closed-loop control is used. Figure 3.5 shows the force tracking of the microgripper operating under closed-loop control.

In addition, a saturation function can be imposed on F_{master} in order to set a programmable limit on the gripping force (refer to Figure 3.4). Figure 3.6 illustrates the behaviour of the hybrid controller with $F_{contact} = 0.1$ g and a force limit set to $F_{limit} = 4.0$ g. Such a feature could enable steady gripping at a constant force, and reduce the possibility of unnecessary trauma to tissues.

Bidirectional control of gripping force is also possible, albeit limited by the stiffness of the flexural suspension. The null point of F_{master} could be changed, and the deadband function could be modified as shown in Figure 3.7. Thus, gripping force would be controllable in both directions. This has been implemented, and control of bidirectional gripping force is shown in Figure 3.8. In this experiment, the tips of the microgripper were inserted into the orifice of a piece of surgical tubing.

Clearly, this type of control could be useful for controlling the force with which a delicate vessel is cannulated (i.e., dilated). Alternatively, the size of small orifices could be measured by closing together the gripper tips, inserting the tips into the centre of the orifice, and slowly spreading the tips apart until contact with the edges of the orifice has been detected. The displacement of the gripper tips could then be inferred either from a position sensor or from the relationship between actuation current and gripper position.

3.2.3 Frequency Response

The performance of the microgripper has been measured experimentally. A step response is shown in Figure 3.9. The force limit is set to 4 g. Note that because the force of the solenoid actuator is dependent on plunger displacement, gains can be scheduled to optimize response. The closed-loop force frequency response was measured with no objects in the microgripper's grasp; environment impedance was provided by the microgripper tips closing against each other. A white noise signal low-pass filtered at 20 Hz was input to the microgripper, and the resulting response is shown in Figure 3.10.

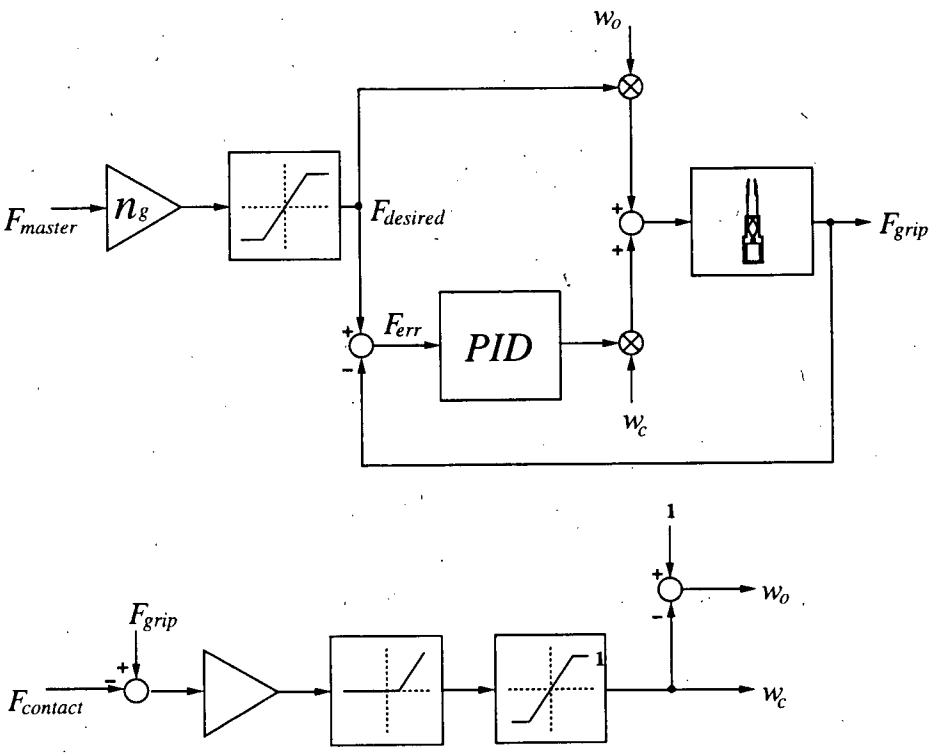

Figure 3.4: Hybrid control

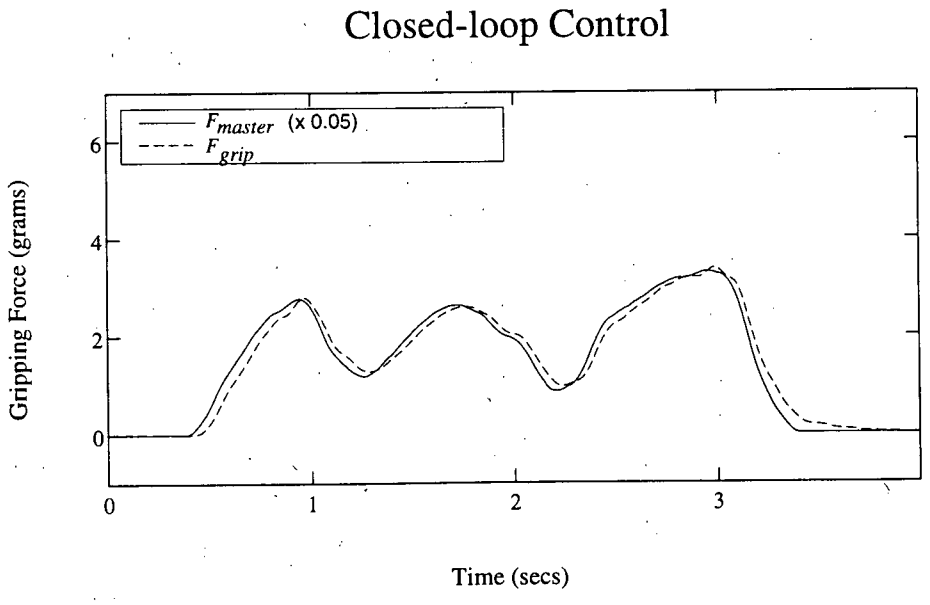

Figure 3.5: Gripping force under closed-loop control

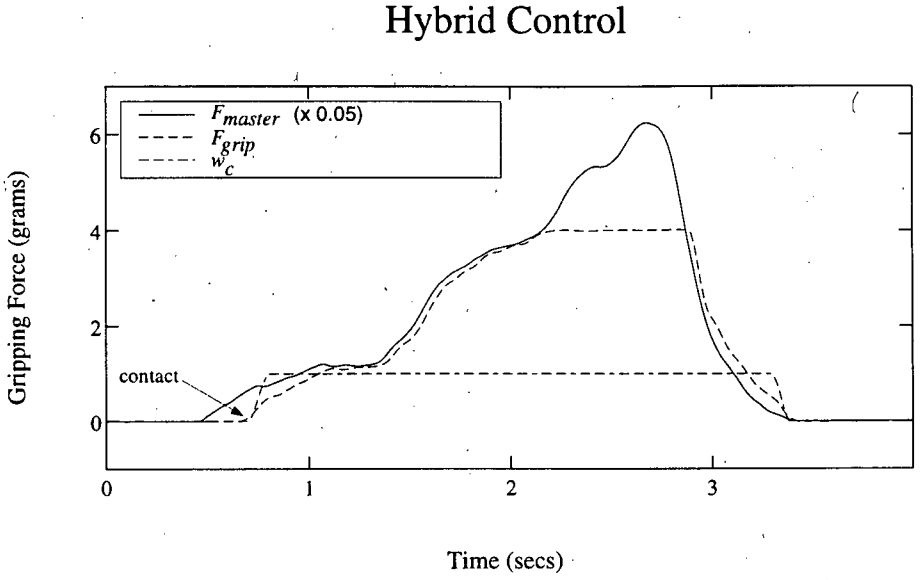

Figure 3.6: Gripping force under hybrid control

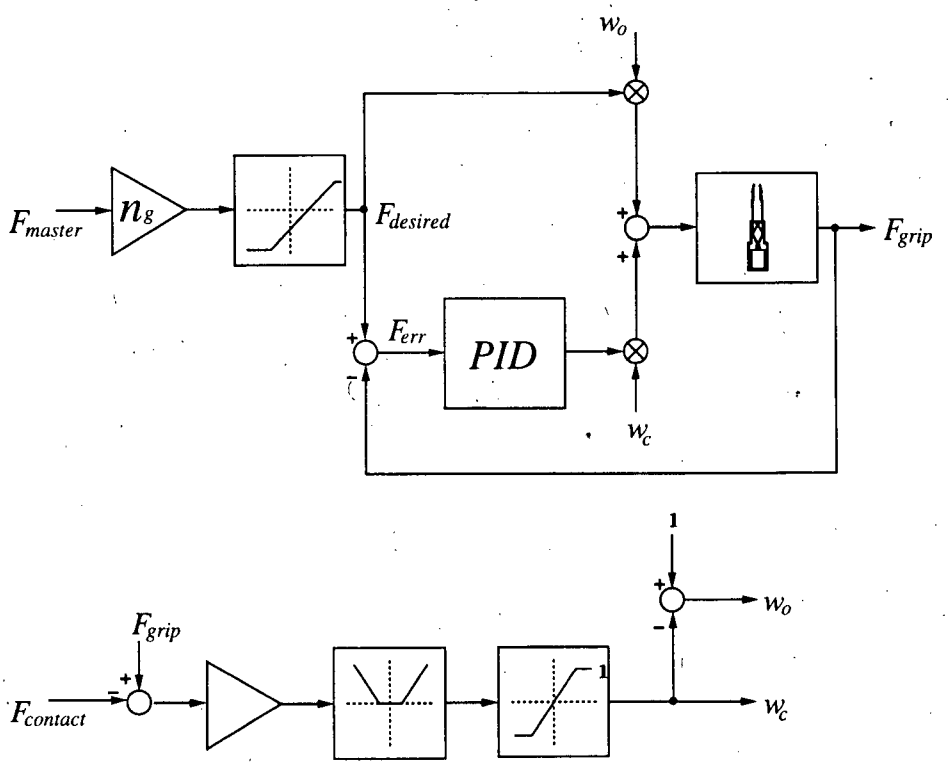

Figure 3.7: Hybrid control of bidirectional gripping force

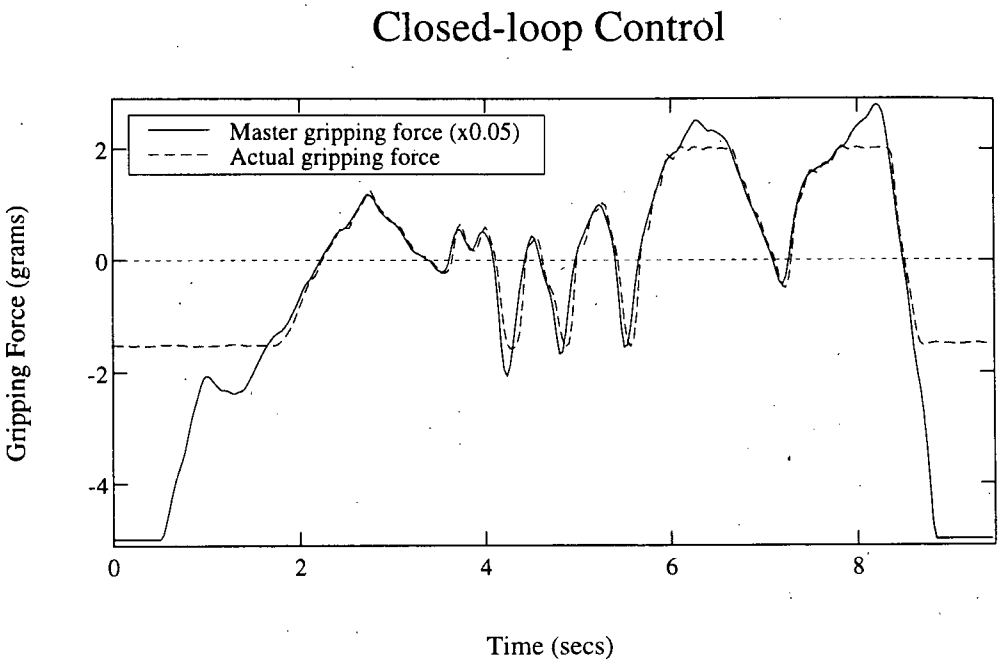

Figure 3.8: Bidirectional gripping force

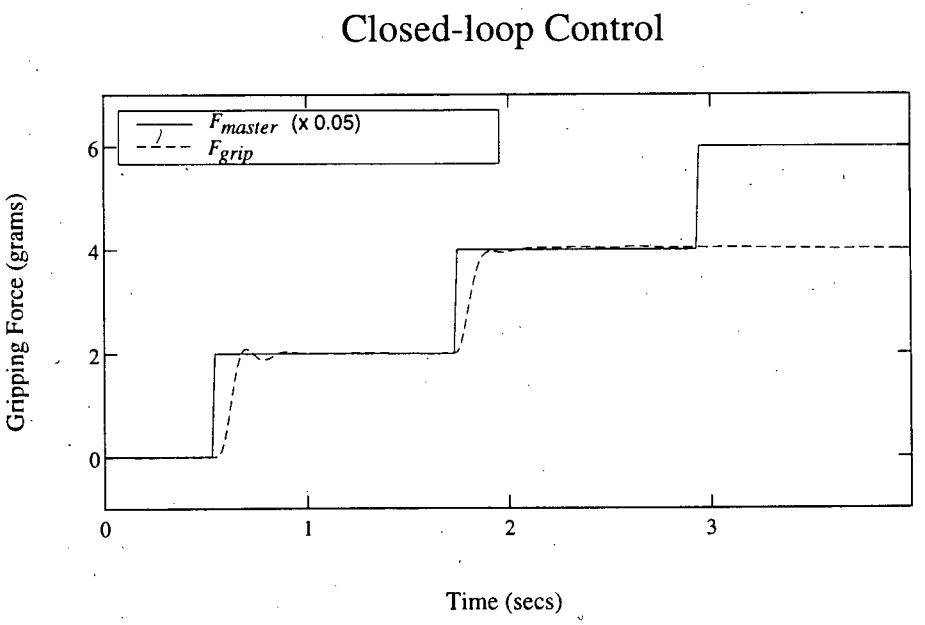

Figure 3.9: Step response and force limit

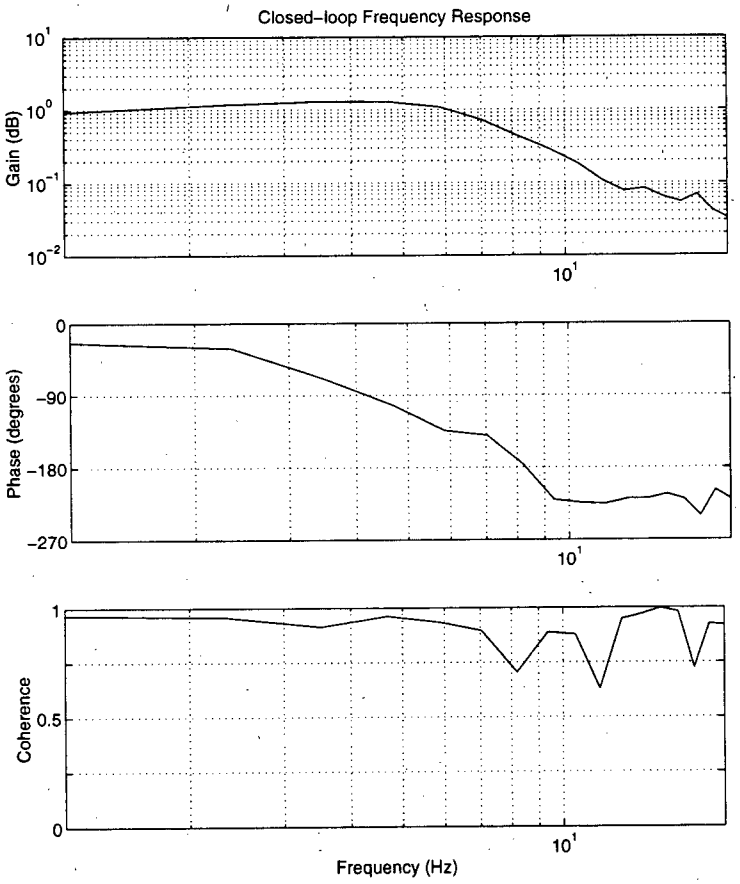

Figure 3.10: Microgripper closed-loop frequency response

3.2.4 Device Emulation

The microgripper can be changed so that it can be useful for a greater variety of tasks. For example, an obvious physical modification might be to change its jaws in accordance with standard microsurgical instruments such as needle drivers, clamps, or bipolar coagulator forceps. However, other physical mechanisms can be emulated by simply altering the control scheme implemented in software. For example, a 6-DOF maglev manipulator was used to emulate different mechanisms such as plunger, slider, translator, rotator, and RCC devices [30]. A similar maglev manipulator was used to emulate static friction and contact with a hard surface [31].

Here, the single degree of freedom of the microgripper can also be controlled in different ways to yield other useful devices. For example, the hybrid control scheme described in Section 3.2.2 could be modified so that the microgripper servoes to the greatest force applied so far (see Figure 3.11). Thus, the microgripper would emulate a hemostat. Figure 3.12 shows the behaviour of the microgripper under hemostat emulation control with a force limit at 4.0 grams.

Not only would this hemostat possess more stops than any conventional instrument with mechanical stops, but it would also enable much more gentle actuation and release. Release could be accomplished by adding a button to the microgripper handle. The constant force of this microgripper hemostat reduces the pressure required to maintain a firm hold on tissue and other objects; therefore, it could be useful as a needle driver, clamp, or "third-hand" tool.

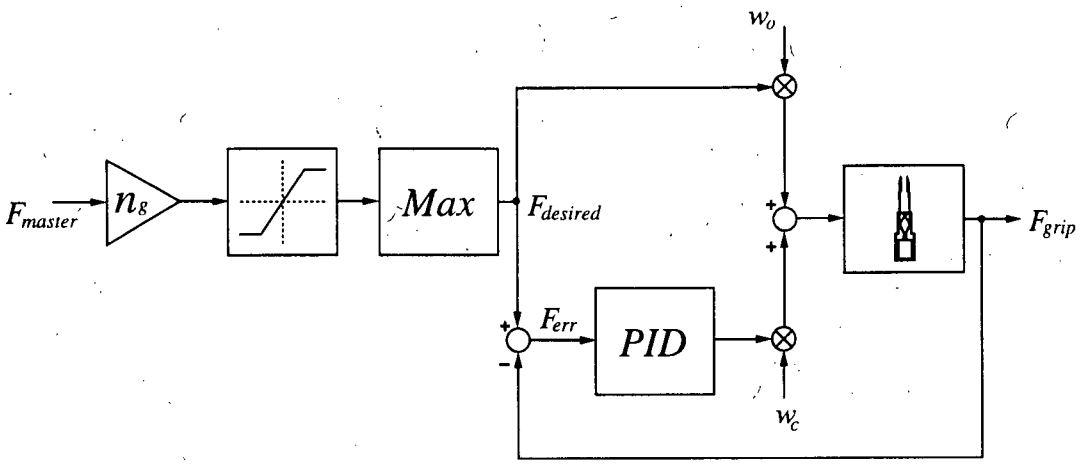

Figure 3.11: Hemostat emulation control

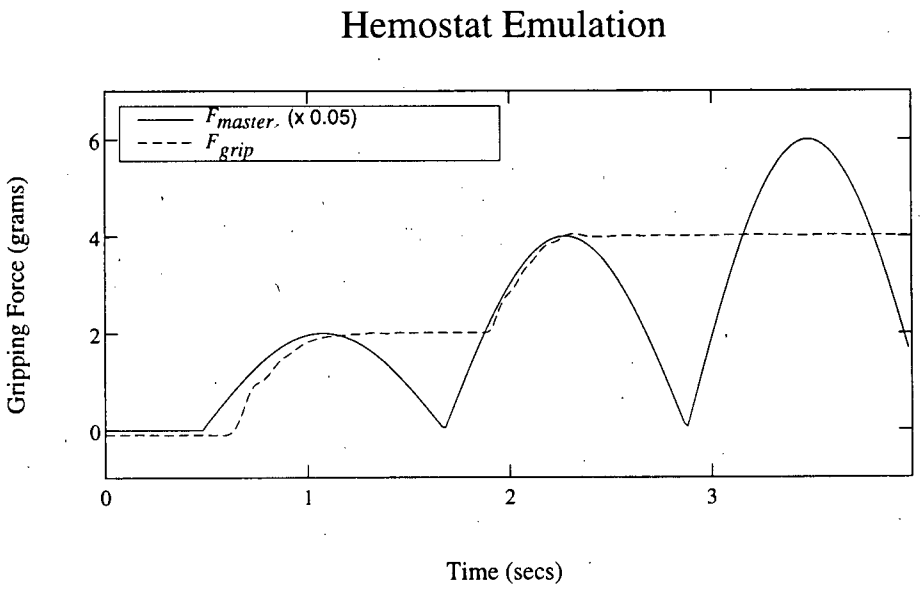

Figure 3.12: Gripping force under hemostat emulation control

3.3 6-DOF Force-Reflecting Motion-Scaling Teleoperation Control

6-DOF bilateral motion scaling of the fine-motion stage was demonstrated experimentally by Yan [20], and an H_∞-optimization approach to controller design was proposed to provide teleoperation system transparency *vs.* stability robustness tradeoffs. However, for perfect transparency, both position and force sensing are required at the master and at the slave. Therefore, force sensing at both the master and slave manipulators has been implemented here.

The slave manipulator has been equipped with a miniature force/torque sensor, and a force/torque observer has been implemented at the master. On-line parameter identification has been used to estimate the inertial parameters of the manipulators for control. Three controllers for bilateral motion-scaling and force-scaling teleoperation of the fine-motion stage have been implemented to demonstrate some different control strategies that could be valuable for microsurgical applications. Henceforth, for convenience, they will be referred to by the following names: PID, computed torque feedforward, and static friction emulation. All are essentially PD or PID-based controllers that share the same teleoperation control framework.

These types of controllers have each been demonstrated previously by others [22, 32, 31]; however, they are implemented here in the context of bilateral motion-scaling teleoperation with scaled force feedback. The basic PID controller is used later on in Chapter 4 for some human-factors experiments. The other two controllers offer additional features such as remote centre of compliance and hands-free operation. Future experiments should reveal their practical merits for manipulation in microsurgery.

The issue of performance evaluation is not addressed in depth here; the emphasis is on the integration of the system components and the implementation of control methods in order to explore and suggest potentially useful ways for controlling and using the

teleoperation system, particularly in a microsurgery environment. The next few sections describe the force/torque sensor, the force/torque observer, and parameter identification. The remaining sections present the control methods implemented and discuss their potential uses in microsurgery.

3.3.1 Force/Torque Sensor

An ATI 6-axis force/torque sensor has been mounted on the slave maglev manipulator to measure tool-tissue forces (see Figure 3.13). Its characteristics are summarized in Table 3.1. The sensing system consists of a transducer, a multiplexer (MUX) box, and an interface box which contains both serial and parallel interfaces. The XVME-200 digital I/O board was used to communicate with the parallel interface. With software executing on a SPARC 1-e CPU, a maximum sampling rate of 1 kHz for 6-axis measurements was obtained. Even faster sampling rates should be possible using faster hardware. The sensor wiring and interface are described in more detail in Appendix C.

Figure 3.13: ATI "nano" force/torque sensor (with wiring collar) mounted on the flotor of the slave manipulator

Table 3.1: Force/Torque Sensor Characteristics

ATI "Nano" Force/Torque Sensor	
Mass[1]	10 g
Dimensions:	
Diameter	17 mm
Height	12 mm
Resolution:	
Force	0.5 g
Torque	0.5 g·cm
Maximum:	
Force	1.5 kg
Torque	500 g·cm
Max. sampling frequency[2]	1 kHz

[1] with end plates and wiring harness
[2] 6-DOF force/torque measurements via parallel interface, XVME-200 digital I/O, and SPARC-1e CPU

3.3.2 Force/Torque Observer

A force observer and a torque observer have been implemented in order to measure hand forces at the master manipulator. The observers are based on the force/torque estimation methods described previously by Hacksel and Salcudean [33].

Both force and torque observers essentially rely on position information and knowledge of the physical characteristics of the manipulator to derive an estimate of external forces. With the flotor modelled as a free-moving rigid body of mass m, a steady-state estimate, f_{est}, of the environment force acting on the flotor can be obtained using knowledge of the known force, f, applied to the flotor, and its measured position:

$$f_{est} = k_p \tilde{x} = k_p(x - \hat{x}) \tag{3.12}$$

where x is the position of the flotor, and $\hat{x}$ is the expected value of x. $\hat{x}$ can be computed

by filtering f and x as follows:

$$\hat{X} = \frac{1}{s^2 + \frac{k_v}{m}s + \frac{k_p}{m}} \left(\frac{1}{m}F\right) + \frac{\frac{k_v}{m}s + \frac{k_p}{m}}{s^2 + \frac{k_v}{m}s + \frac{k_p}{m}}X \tag{3.13}$$

where k_p and k_v are positive gains.

In a similar manner, environment torque acting on the flotor can be estimated by:

$$\tau_{est} = \frac{1}{2}Jk_p(\beta - \hat{\beta}) \tag{3.14}$$

The orientation of the flotor has been parametrized by Euler quaternions, β, and $\hat{\beta}$ can be estimated by filtering β and the known torque, τ, applied to the flotor:

$$\hat{\beta} = \frac{1}{s^2 + \frac{1}{2}k_v s + \frac{1}{4}k_p}\mu + \frac{\frac{1}{2}k_v s + \frac{1}{4}k_p}{s^2 + \frac{1}{2}k_v s + \frac{1}{4}k_p}\beta \tag{3.15}$$

where

$$\mu = \frac{1}{2}J^{-1}\tau \quad . \tag{3.16}$$

Implementation

The transfer functions in (3.13) and (3.15) were implemented as digital filters, in the form:

$$\begin{aligned} \hat{X} &= \frac{1}{s^2 + 2\rho\omega_0 s + \omega_0^2}\left(\frac{1}{m}F\right) + \frac{2\rho\omega_0 s + \omega_0^2}{s^2 + 2\rho\omega_0 s + \omega_0^2}X \\ \hat{\beta} &= \frac{1}{s^2 + 2\rho\omega_0 s + \omega_0^2}\mu + \frac{2\rho\omega_0 s + \omega_0^2}{s^2 + 2\rho\omega_0 s + \omega_0^2}\beta \quad . \end{aligned} \tag{3.17}$$

The Matlab function `tf2ss()` was used off-line to convert the transfer functions into state-space form, and the function `c2dm()` was used to convert the continuous-time system into a discrete-time system. Parameter values $\omega_0 = 40\pi$ and $\rho = 1$ were used. The filters were then implemented in C and executed along with the control software, in real time under VxWorks.

In practice, the force and torque observers implemented on the master maglev manipulator performed quite well. Figure 3.14 illustrates the accuracy and speed of convergence of the results while a known force (0.49 N) and torque (0.33 N·dm) were produced by hand-placing a 50-gram weight onto a point on the flotor.

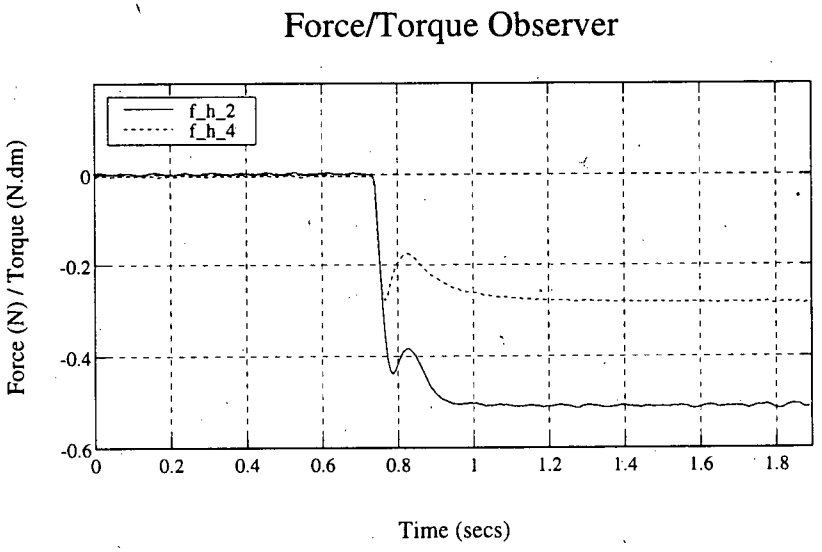

Figure 3.14: Force (f_z) and torque (τ_y) observed while weight is placed on edge of flotor

3.3.3 Parameter Identification

Parameter identification was used to obtain estimates of the parameters of the maglev manipulators. These are used for accurate gravity compensation and for the implementation of the force/torque observer and computed torque feedforward control. In contrast to the force/torque estimation method presented earlier (refer to Section 3.3.2), the parameter estimation method implemented here applies known forces and torques to the manipulator, and uses the resulting motions to determine estimates of the inertial parameters of the manipulator.

The method that has been implemented is based on the commonly used recursive least-squares (RLS) algorithm. The application of RLS estimation to a 6-DOF maglev manipulator was previously demonstrated by Hacksel [33], and a detailed description can be found in [32].

The algorithm yields the following parameters:

$$\theta = [m\ mc_1\ mc_2\ mc_3\ J_{11}\ J_{12}\ J_{13}\ J_{21}\ J_{23}\ J_{33}]^T \tag{3.18}$$

where m is the mass of the flotor, and c and J are its centre of mass and inertia matrix with respect to the flotor-attached coordinate frame whose origin is located at the centre of the LEDs. Using the Huygens-Steiner formula, the inertia matrix of the flotor can be easily expressed with respect to its centre of mass:

$$J_c = J + m[(c-o)\times]^2 \tag{3.19}$$

where, for a vector $a = [a_1\ a_2\ a_3]^T$,

$$a\times \triangleq \begin{bmatrix} 0 & -a_3 & a_2 \\ a_3 & 0 & -a_1 \\ -a_2 & a_1 & 0 \end{bmatrix} . \tag{3.20}$$

Implementation

On-line RLS estimation was implemented in C and executed under VxWorks. Position measurements were low-pass filtered using a second-order Butterworth filter with a 50 Hz cut-off frequency, before being double-differentiated to obtain accelerations. Since the accuracy of parameter estimates is dependent on the "persistency" or richness of the excitation, each degree of freedom was excited by a pseudo-random white noise signal, low-pass filtered at 20 Hz. A "forgetting factor" of $\gamma = 0.9999$ was used. Experimental results are shown below in Tables 3.2 and 3.3. Estimates derived from AutoCAD drawings are also given for comparison. As indicated in Figures 1.3 and 1.4, the coordinate system of each maglev manipulator is centred at the point where the axes of the three LED beams intersect.

Table 3.2: Master manipulator parameters

	m (g)	c (mm)	J_c $(g{\cdot}m^2)$
Computed from AutoCAD, Flotor only[1]	630.8	$\begin{bmatrix} 0 \\ 0 \\ -5.56 \end{bmatrix}$	$\begin{bmatrix} 1.04 & 0 & 0 \\ 0 & 1.04 & 0 \\ 0 & 0 & 1.26 \end{bmatrix}$
Experimental estimate, Flotor only	621.6	$\begin{bmatrix} 1.27 \\ -0.596 \\ -3.93 \end{bmatrix}$	$\begin{bmatrix} 0.989 & 0.0258 & 0.0055 \\ 0.0258 & 0.950 & 0.0127 \\ 0.0055 & 0.0127 & 1.27 \end{bmatrix}$
Experimental estimate, Flotor with Handle	704.2	$\begin{bmatrix} 0.748 \\ -0.572 \\ 2.02 \end{bmatrix}$	$\begin{bmatrix} 1.256 & 0.0421 & 0.0281 \\ 0.0421 & 1.19 & 0.0135 \\ 0.0281 & 0.0135 & 1.27 \end{bmatrix}$

[1] coils modelled as solid copper

Table 3.3: Slave manipulator parameters

	m (g)	c (mm)	J_c $(g{\cdot}m^2)$
Computed from AutoCAD, Flotor only[1]	33.3	$\begin{bmatrix} 0.0517 \\ -0.0769 \\ 24.8 \end{bmatrix}$	$\begin{bmatrix} 0.0137 & 0.000000480 & 0.0000280 \\ 0.000000480 & 0.0138 & -0.0000079 \\ 0.0000280 & -0.0000079 & 0.00596 \end{bmatrix}$
Experimental estimate, Flotor only	34.0	$\begin{bmatrix} 2.46 \\ 0.377 \\ 21.1 \end{bmatrix}$	$\begin{bmatrix} 0.00995 & -0.0000415 & 0.0000311 \\ -0.0000415 & 0.0116 & -0.0000849 \\ 0.0000311 & -0.0000849 & 0.00634 \end{bmatrix}$
Experimental estimate, Flotor with ATI Sensor[2]	47.1	$\begin{bmatrix} 2.82 \\ 0.887 \\ 26.2 \end{bmatrix}$	$\begin{bmatrix} 0.0144 & -0.000749 & -0.000279 \\ -0.000749 & 0.0182 & -0.000641 \\ -0.000279 & -0.000641 & 0.00729 \end{bmatrix}$
Experimental estimate, Flotor with ATI Sensor and Microgripper[3]	54.4	$\begin{bmatrix} 2.98 \\ 1.05 \\ 30.6 \end{bmatrix}$	$\begin{bmatrix} 0.0204 & 0.000429 & -0.000436 \\ 0.000429 & 0.0265 & -0.000908 \\ -0.000436 & -0.000908 & 0.00751 \end{bmatrix}$

[1] coils modelled as solid aluminum

[2] including adapter plates; ATI sensor oriented with "rear plate" towards flotor $(-z)$, and rotated about z-axis by -120°

[3] gripping motion oriented along x-axis

3.3.4 PID Control

Bilateral motion-scaling and force-scaling teleoperation of the fine-motion stage using a PID-based controller was proposed in [1, 20]. Using position sensing only, motion scaling in six degrees of freedom was demonstrated. The addition of force sensing here now makes it possible to achieve improved teleoperation transparency by providing the operator with high-fidelity force feedback.

The controller implemented here follows from the approach described by Yan in [20]:

$$\begin{aligned} f_m &= n_f f_e - f_c \\ f_s &= \frac{1}{n_f}(f_h + f_c) \\ f_c &= k_c(x_m - n_p x_s) \end{aligned} \tag{3.21}$$

where f_m and f_s are the master and slave actuator forces, f_h and f_e are the hand and environment forces, and x_m and x_s are the master and slave positions. n_p and n_f are the position-scaling and force-scaling factors. The coordinating force, f_c, is implemented here using here using straight PID control:

$$k_c = k_p + k_v s + \frac{k_i}{s} \quad . \tag{3.22}$$

Implementation

Environment forces were measured using the ATI sensor, and hand forces were measured using the force/torque observer. Force-scaling was set to $n_f = 20$. A position-scaling factor of $n_p = 10$ was used; however, this ten-fold magnification of motion from the slave to the master resulted in the flotor of the master contacting its workspace limits while in free motion. Therefore, n_p was reduced to 2 for the slave-to-master position scaling.

In addition, the gains of the local coordinating-force controllers were individually tuned for each manipulator. The gains used were as follows:

$$
\begin{array}{ll}
master\ k_c & \left\{ \begin{array}{lcll} k_p & = & [0.7\ 0.7\ 0.7\ 10.0\ 10.0\ 10.0]^T & N/mm, N{\cdot}dm/rad \\ k_d & = & [0.015\ 0.015\ 0.015\ 0.5\ 0.5\ 0.5]^T & N/(mm/s), N{\cdot}dm/(rad/s) \\ k_i & = & [0.5\ 0.5\ 0.5\ 3.0\ 3.0\ 3.0]^T & N/(mm{\cdot}s), N{\cdot}dm/(rad{\cdot}s) \end{array} \right. \\
slave\ k_c & \left\{ \begin{array}{lcl} k_p & = & [0.1911\ 0.1911\ 0.65\ 2.73\ 2.73\ 1.68]^T \\ k_d & = & [0.0015\ 0.0015\ 0.009\ 0.0506\ 0.0506\ 0.0202]^T \\ k_i & = & [0.16\ 0.16\ 0.16\ 0.16\ 0.16\ 0.16]^T \end{array} \right.
\end{array}
\tag{3.23}
$$

Control of the slave manipulator was previously performed with respect to the origin of the flotor-attached coordinate frame (refer to Figure 1.4). However, unlike the master manipulator, the centre of mass of the slave manipulator flotor is displaced a significant distance from the sensing centre (refer to Table 3.3). Therefore, the centre of control was moved to the centre of mass in order to reduce coupling between the 6-DOF motions, thereby enabling stiffer control.

Position tracking of the manipulators without feedforward of hand and environment forces is shown in Figures 3.15 and 3.16. Figure 3.15 shows the position of the slave in free motion tracking the motion of the master. The master was driven by hand in an arbitrary trajectory. Similarly, Figure 3.16 shows the position of the master in free motion tracking the motion of the slave. Notice the slight oscillations in slave position due to inadequately tuned PID gains.

Feedforward of hand and environment forces is shown in Figures 3.17 and 3.18. Figure 3.17 shows arbitrary environment forces and torques applied to the slave, and the corresponding scaled forces and torques observed by the force/torque observer at the master. Similarly, Figure 3.18 shows arbitrary hand forces and torques applied to the

master, and the scaled-down forces and torques measured at the slave by the ATI sensor positioned against an infinitely stiff environment. Note that f_e is opposite in sign from f_h in Figure 3.18. Because the ATI sensor is positioned against an infinitely stiff environment, a positive force fed forward along, say, the positive z-axis results in a measured environment force in the opposite direction (along the negative z-axis).

These results illustrate how force sensing at the slave can be beneficial. Small environment forces at the slave can be magnified and fedforward to the master, giving the operator high-fidelity kinesthetic feedback of delicate tool-tissue forces.

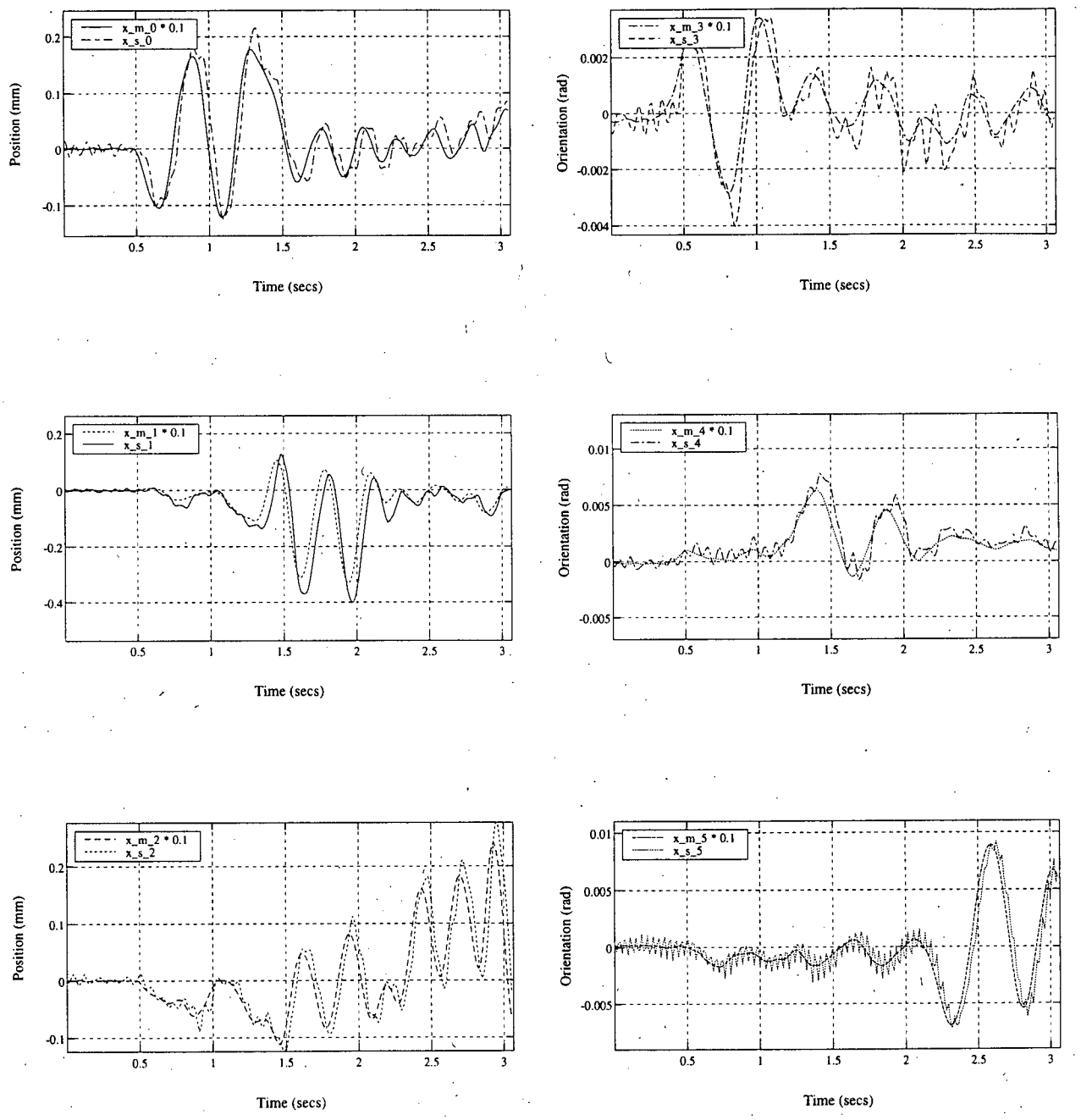

Figure 3.15: Slave in free motion tracking master: position (left) and orientation (right)

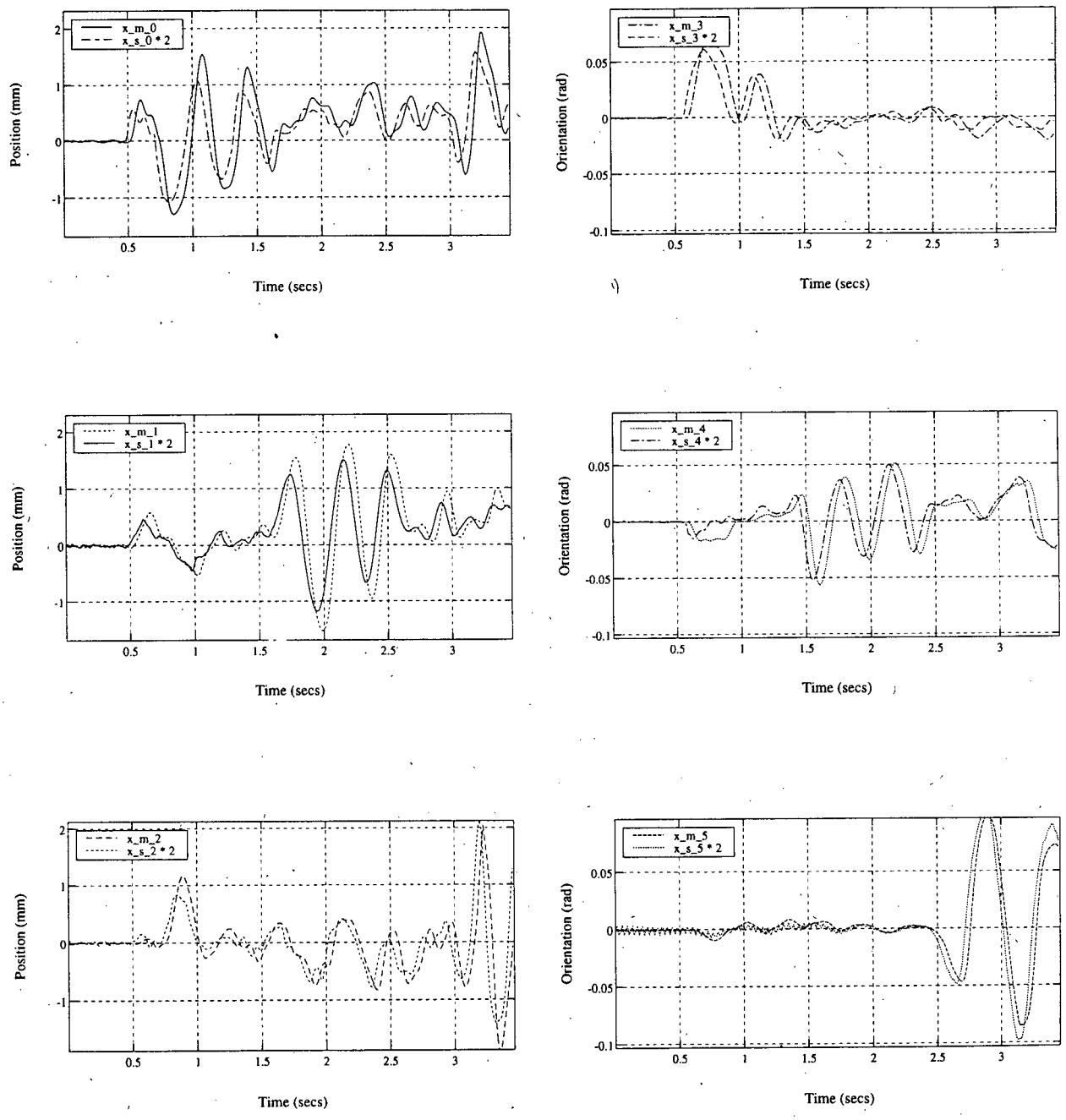

Figure 3.16: Master in free motion tracking slave: position (left) and orientation (right)

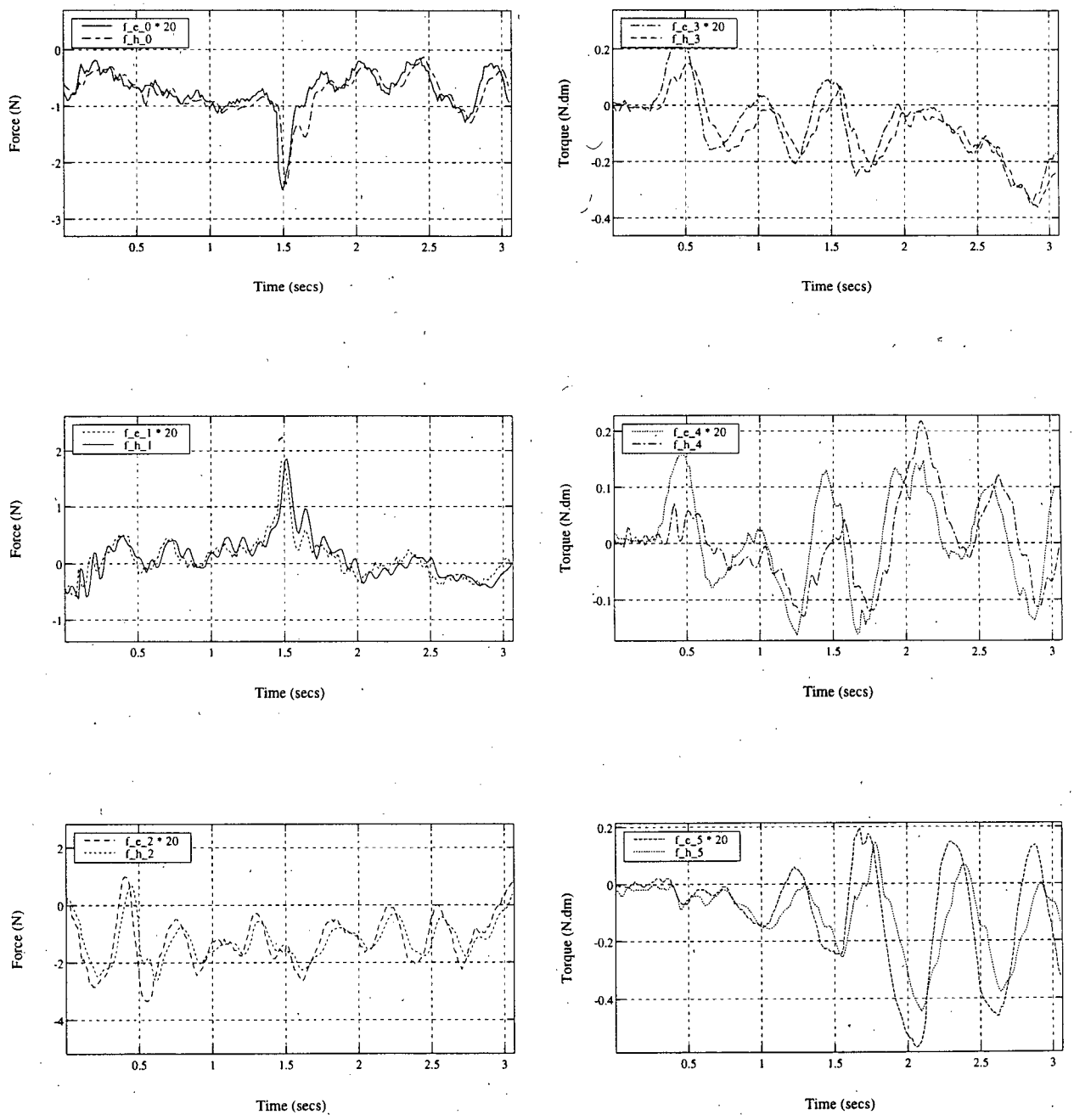

Figure 3.17: Environment forces (left) and torques (right) fed forward to master

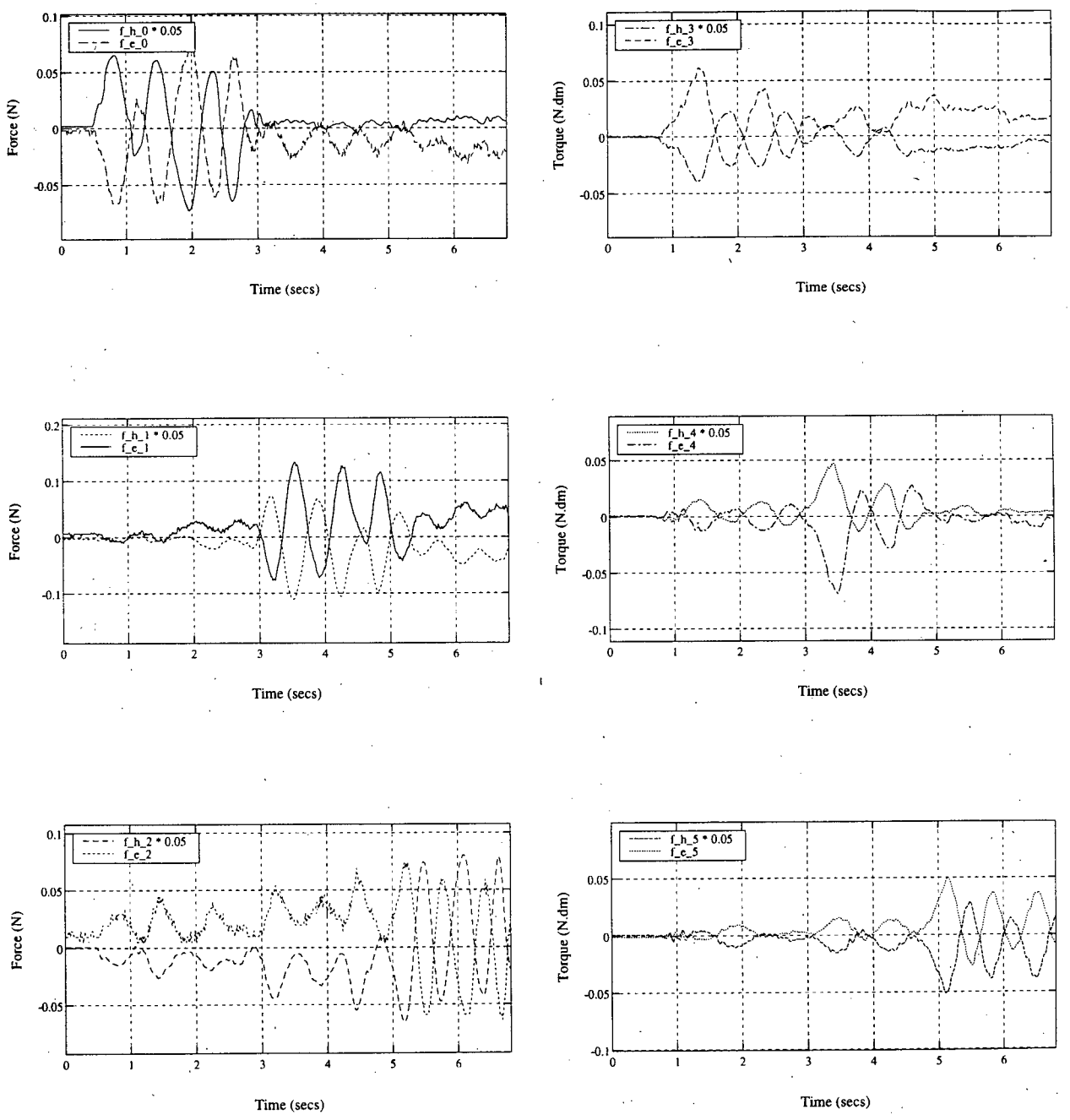

Figure 3.18: Hand forces (left) and torques (right) fed forward to slave

3.3.5 Computed Torque Feedforward Control

This controller follows the same teleoperation control approach described by (3.21). However, a linearized "computed torque feedforward" scheme proposed by Hollis, Salcudean, and Allan [30] is used for the local coordinating-force controller, k_c, instead of straight PID control. This control scheme was demonstrated previously on a 6-DOF maglev manipulator by Hacksel [33].

This controller enables the simple emulation of an arbitrary remote centre of compliance (RCC) at each maglev manipulator by displacing the tool point, r_T. This could improve the sense of teleoperation transparency conveyed to the operator since the centres of compliance for master-slave coordinated motion could be relocated to more intuitive locations. For example, the RCC of the master manipulator could be placed at the location of the operator's fingers on the handle, as it would be naturally on a hand-held stylus.

The following control law was used:

$$\begin{aligned} {}^{F}\tau &= 2\,{}^{F}J[K_p(\beta_d - \beta) - K_v\dot{\beta}] \\ f &= m[-g + {}^{F}r_T \times {}^{F}J^{-1}{}^{F}\tau + \tilde{K}_p(r_d - r_T) - \tilde{K}_v\dot{r}_T] \ , \end{aligned} \tag{3.24}$$

resulting in the following modified system dynamics:

$$\begin{aligned} \ddot{\beta} &= K_p(\beta_d - \beta) - K_v\dot{\beta} \\ \ddot{r}_T &= \tilde{K}_p(r_d - r_T) - \tilde{K}_v\dot{r}_T \ . \end{aligned} \tag{3.25}$$

f and τ are the force and torque applied to the flotor, m is its mass, β is its rotation parametrized by Euler quaternions, ω is its angular velocity, and J is its inertia matrix.

The superscript, ^{F}, denotes vectors or matrices that are expressed with respect to the flotor coordinate frame. r_T is the "tool-point", a point that is fixed to the flotor coordinate frame, and r_d and β_d are the desired tool position and orientation. g is the gravitational acceleration. The elements of the gain matrices, K_p, K_v, $\tilde{K}_p$, and $\tilde{K}_v$ can be chosen independently to emulate different physical mechanisms (e.g., slider, plunger, translator, rotator), and are defined with respect to arbitrarily chosen rotation matrices as follows:

$$\begin{aligned} K_p &\triangleq R^T diag(k_{p1}, k_{p2}, k_{p3}) R \\ K_v &\triangleq R^T diag(k_{v1}, k_{v2}, k_{v3}) R \\ \tilde{K}_p &\triangleq \tilde{R}^T diag(\tilde{k}_{p1}, \tilde{k}_{p2}, \tilde{k}_{p3}) \tilde{R} \\ \tilde{K}_v &\triangleq \tilde{R}^T diag(\tilde{k}_{v1}, \tilde{k}_{v2}, \tilde{k}_{v3}) \tilde{R} \; . \end{aligned} \tag{3.26}$$

Implementation

This controller was implemented on both master and slave manipulators. Mass, centre of mass, and inertial parameters were obtained using parameter identification (refer to Section 3.3.3), and the following gains were chosen to provide stiff control and good "feel".

$$master \begin{cases} k_p &= [300\ 300\ 300]^T & 1/s^2 \\ k_v &= [30\ 30\ 30]^T & 1/s \\ \tilde{k}_p &= [700\ 700\ 700]^T & 1/s^2 \\ \tilde{k}_v &= [30\ 30\ 30]^T & 1/s \end{cases}$$

$$
\begin{aligned}
& \\
slave \quad & \begin{cases} k_p &= [2100\ 2100\ 2100]^T & 1/s^2 \\ k_v &= [20.25\ 20.25\ 20.25]^T & 1/s \\ \tilde{k}_p &= [1470\ 1470\ 5000]^T & 1/s^2 \\ \tilde{k}_v &= [6.08\ 6.08\ 36]^T & 1/s \end{cases} \\
R &= I
\end{aligned}
\tag{3.27}
$$

Figure 3.19 shows the slave in free motion tracking the motion of the master driven by hand in an arbitrary trajectory. Likewise, Figure 3.20 shows the master in free motion tracking the motion of the slave. By cancelling the dynamics of the manipulator motion, this controller can provide better performance than the simple PID controller, using lower gains. However, inaccuracies in the estimates of the manipulator's inertial parameters can lead to biases, as shown in Figure 3.19.

Figure 3.21 demonstrates the motion of the remote centre of compliance while an arbitrary hand motion is applied to the flotor. Shown are the positions of three points: the RCC, set to $r_T = [0\ 0\ 40]^T$ mm; $point_1$, located 20 mm above r_T; and $point_2$, located 20 mm below r_T. As expected, r_T does not move significantly, and the two points on either side of r_T show much greater displacement in opposite directions.

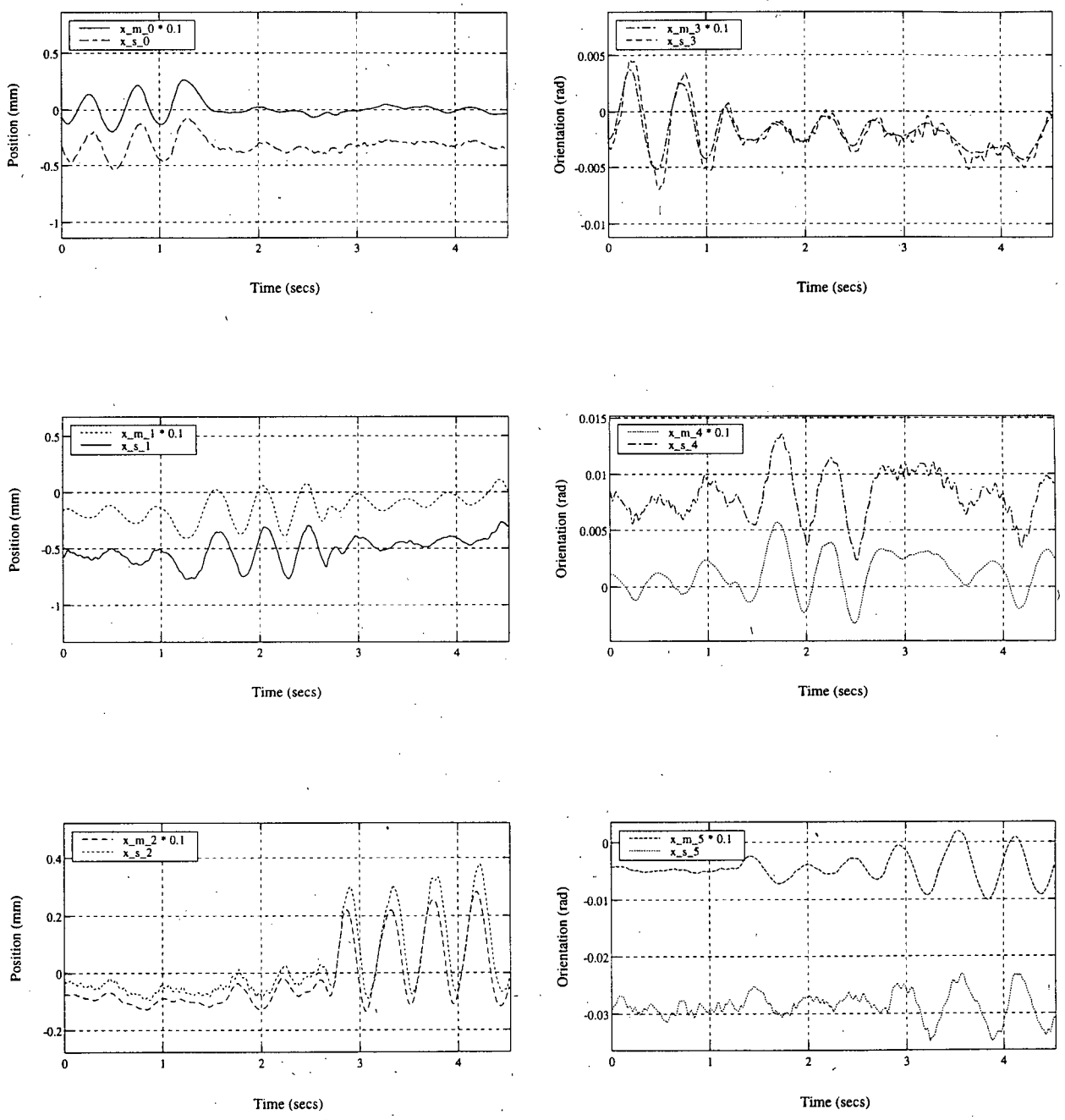

Figure 3.19: Slave in free motion tracking master: position (left) and orientation (right)

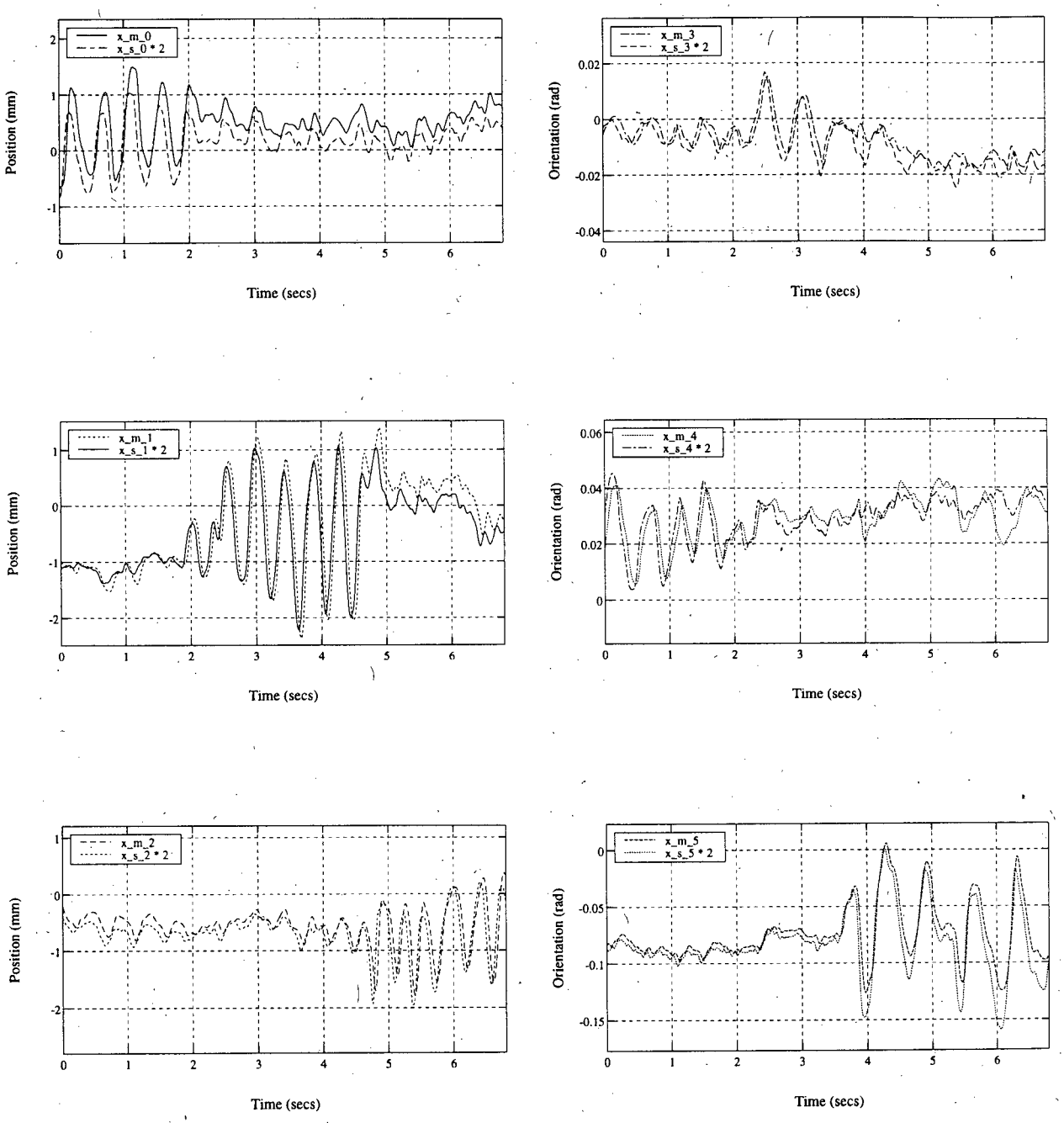

Figure 3.20: Master in free motion tracking slave: position (left) and orientation (right)

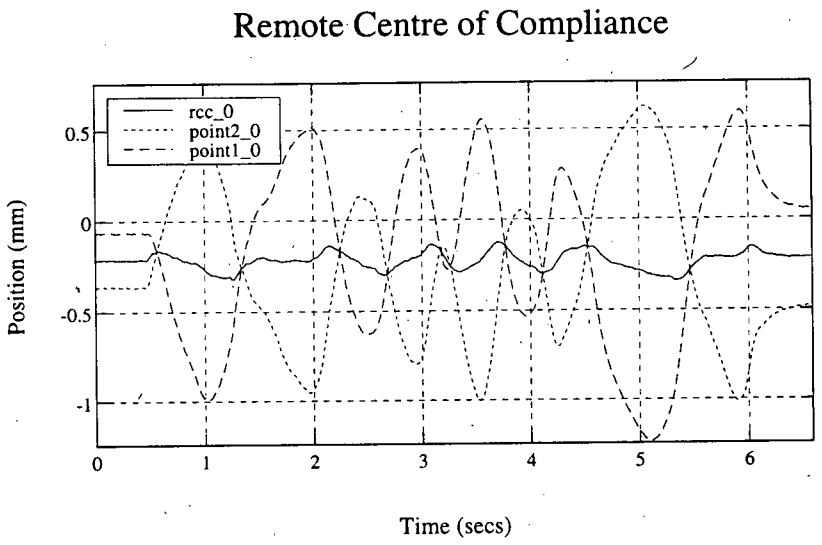

Figure 3.21: Positions of remote centre of compliance and two nearby points

3.3.6 Static Friction Emulation

This controller follows the same teleoperation control approach implemented earlier. Here, however, coordinating force is applied unilaterally to the slave only; i.e., the slave tracks the position of the master, and the master is controlled using a static friction emulation scheme. Environment force is also measured and fedforward to the master; that is,

$$\begin{aligned} f_m &= n_f f_e + f_{friction} \\ f_s &= k_c(x_m - n_p x_s) \quad . \end{aligned} \tag{3.28}$$

Emulation of static friction using a 6-DOF maglev manipulator was demonstrated previously by Vlaar [31, 34]. The approach taken is based on Karnopp's model of stick-slip friction in one degree of freedom, which uses two states (STUCK and SLIDING) to model static friction between a mass and the surface on which it is sliding. The motion of the mass is modelled as:

$$m\ddot{x} = f_{ext} - k_d\dot{x} + f_{stick} \tag{3.29}$$

where f_{ext} is an external force, $-k_d\dot{x}$ is an applied damping force, and f_{stick} is the applied stiction force:

$$\begin{aligned} f_{stick} &= f_{ext} \quad \text{, if STUCK} \\ f_{stick} &= 0 \quad \text{, if SLIDING.} \end{aligned} \tag{3.30}$$

The state transitions are defined as follows:

$$\text{STUCK} \underset{|\dot{x}|<v_{min}}{\overset{|f_{ext}|>f_{max}}{\rightleftarrows}} \text{SLIDING} \tag{3.31}$$

This model can be approximated using a PD controller and position sensing only as follows:

$$\begin{aligned} m\ddot{x} &= f_{ext} - k_d\dot{x} + f_{stick} \\ f_{stick} &= k_p(x_{STUCK} - x) \quad \text{, if STUCK} \\ f_{stick} &= 0 \quad \text{, if SLIDING} \end{aligned} \tag{3.32}$$

$$\text{STUCK} \underset{(set\ x_{STUCK}=x)}{\overset{|f_{stick}|>f_{max}}{\rightleftarrows}} \text{SLIDING} \tag{3.33}$$

Implementation

Applying the model described above to the local controller for the master manipulator, we obtain:

$$\begin{aligned} f_m &= n_f f_e + f_{stick} - k_d\dot{x}_m \\ f_s &= k_c(x_m - n_p x_s) \quad . \end{aligned} \tag{3.34}$$

Values used for n_f, n_p, and k_c are given in Section 3.3.4. Static friction emulation control was succesfully implemented for each of the six degrees of freedom of the master manipulator. The following parameters were used:

$$\begin{aligned}
k_p &= [3.5\ 3.5\ 3.5\ 15\ 15\ 15]^T & N/mm, N{\cdot}dm/rad \\
k_d &= [0.0225\ 0.0225\ 0.0225\ 0.75\ 0.75\ 0.75]^T & N/(mm/s), N{\cdot}dm/(rad/s) \\
f_{max} &= [0.6\ 0.6\ 0.6\ 0.3\ 0.3\ 0.3]^T & N, N{\cdot}dm \\
v_{min} &= [30\ 30\ 30\ 5\ 5\ 5]^T & mm/s, rad/s
\end{aligned} \tag{3.35}$$

Figure 3.22 shows the position and orientation of the slave in free motion tracking the master moved in an arbitrary trajectory. Notice that the position of the master, and thus the slave, remains stationary once the hand of the operator is released.

Under this teleoperation control scheme, the master manipulator provides a small frictional resistance to the motion of the operator's hand, and once released, active control keeps the manipulator stationary, regardless of its position or orientation. In the context of microsurgery, this type of control could make the teleoperation system particularly useful as a "third-hand" tool, where accurate positioning and "hands-free" operation are important.

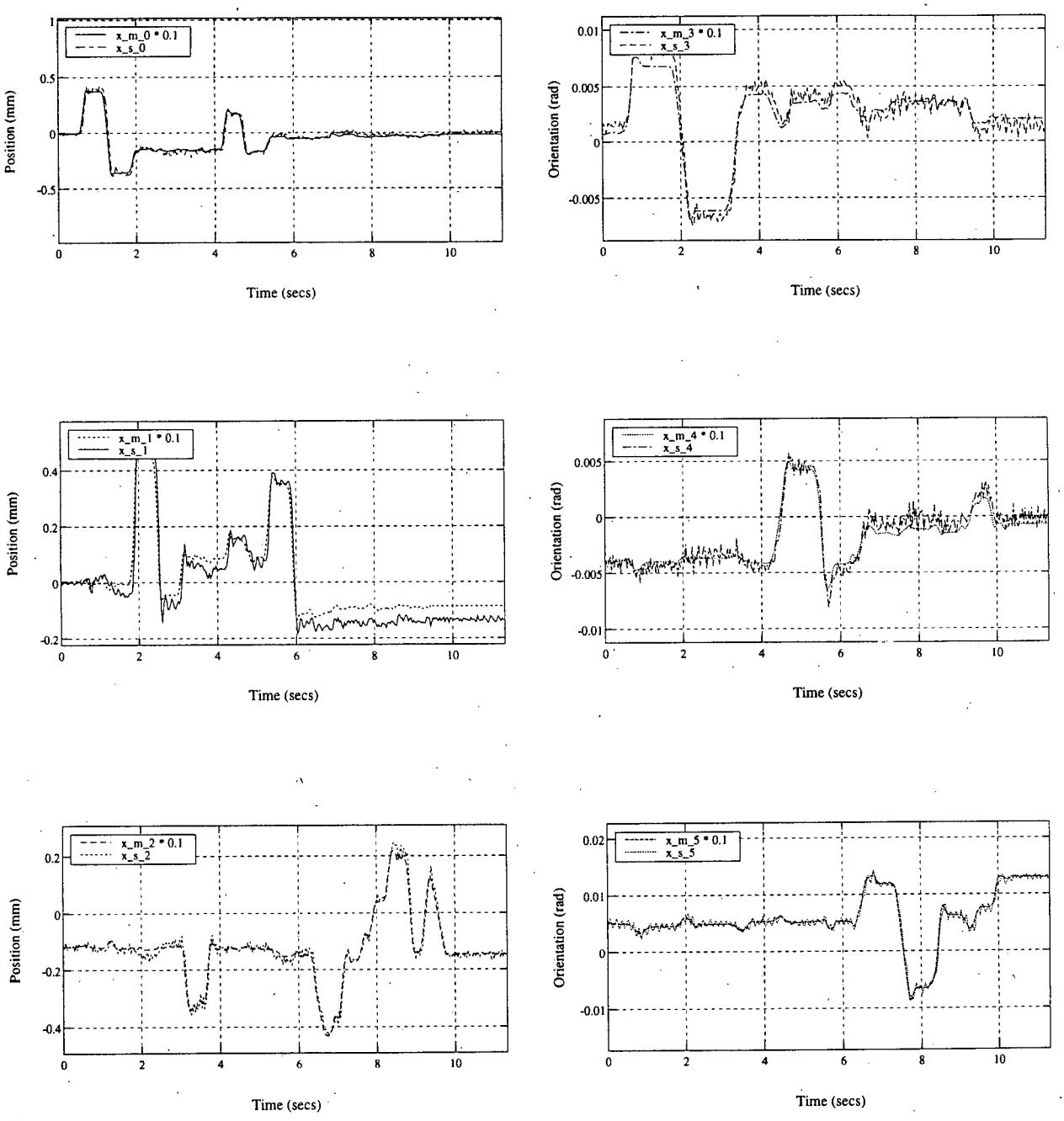

Figure 3.22: Slave in free motion tracking master: position (left) and orientation (right)

Chapter 4

Experiments

4.1 Overview

The previous chapters concentrated on the design and control of the microgripper and motion-scaling teleoperation system, with the objective of producing devices useful for microsurgery. The potential benefits of these devices include the ability to achieve much finer control over tool motions and tool-tissue forces, and the ability to measure tool-tissue forces in seven degrees of freedom. This chapter examines these two issues. The first part of this chapter discusses the issue of evaluating manual dexterity in teleoperation through experiments that simulate microsurgical conditions. The second part discusses the measurement of motions and forces during microsurgery using alternative microsurgical instruments such as the hand-held microgripper.

4.2 Manual Dexterity

The main purpose of the motion-scaling teleoperation system is to extend microsurgeons' ability to control fine motions. Therefore, it is important to determine how manual dexterity is affected by its use. One method of evaluating teleoperation performance involves executing a task in a controlled environment, and measuring the quality with which the task was performed. "Peg-in-hole"-type tasks are often used [35, 36, 37]. By executing the task under different conditions, one can obtain a relative measure of the performance achieved under each of the experimental conditions (e.g., teleoperation *vs.*

direct manipulation), thereby leading to a better understanding of the individual factors that may bear an influence on task performance.

4.2.1 Task Design

The experimental task itself could consist of simple, general motions involving a structured work environment. Some examples are listed in Table 4.1. These could be categorized as "generic tasks", following the terminology used by Hannaford *et al.* [35]. These types of tasks provide general results that can be extended to other application-specific manipulation tasks. Furthermore, the simplicity and structured nature of the tasks makes it easier to reproduce the experimental conditions and make fair comparisons of performance using different hardware.

Table 4.1: Generic tasks

Task	*Description*
Manoeuvre	Starting from home position, manoeuvre forceps to end position/orientation
Manoeuvre and grasp	Starting from home position, manoeuvre forceps and grip target object
Manoeuvre, grasp, and reposition	Starting from home position, manoeuvre forceps, grip target object, and move it to end position/orientation
Hold stationary	Hold forceps in a specific position and orientation for a prescribed period of time

Alternatively, the experimental task could involve more complex "application tasks" which, in this case, would be specific to microsurgery. Table 4.2 offers a few examples. While the data resulting from the execution of these types of tasks are less general, they are more likely to reveal valuable insights into application-specific issues (e.g., mechanical

design, performance limitations, and human-factors issues).

Table 4.2: Application tasks for microvascular surgery

Task	*Description*
Grasp adventitia	Starting from home position, manoeuvre forceps to vessel opening, grip adventitia, and pull it a prescribed amount
Cannulate vessel	Starting from home position, manoeuvre forceps to vessel opening, insert tips of forceps to a prescribed depth, and dilate vessel opening a specific amount
Place guide suture	With the tips of the forceps inside the cannulated vessel, pass the microneedle (held by needle-holders in the dominant hand) through the anterior wall of the vessel, between the tips of the forceps

4.2.2 Performance Measures

The quality with which the task is executed can be quantified in various ways. Task completion time, although crude, is relatively simple to measure; thus, it has been used in almost all human-factors studies to date as a measure of the ease with which a task can be performed. In fact, completion time would be an essential performance measure here, since task efficiency is paramount in microsurgical operations.

Tool-tissue force would also be an important measure, since it is important to minimize excess contact force in tasks involving delicate manipulation. Mean force is generally not a good measure since large positive and negative swings may not necessarily be reflected in the overall average. In "peg-in-hole" tasks, Hannaford *et al.* used the sum of squared forces (SOSF):

$$SOSF = \sum_{i=1}^{N} f_i^2 dt \quad . \tag{4.36}$$

SOSF is a general measure that can be combined among different axes. Furthermore, SOSF scores for tasks of different durations can be added together since the SOSF is weighted by time. In comparison, an RMS measure is normalized with respect to the time duration; therefore, the simple addition of several RMS scores leads to bias favouring the shorter tasks.

Alternative performance measures could include: peak force, task error or failure rate, range of tool motion, tool trajectory, and tool velocity. The next two sections present experiments that use performance measures to quantify the effects of scaled motion and scaled force feedback on fine manipulation.

4.3 Motion Scaling Experiment

An experiment was performed to determine how manual dexterity is affected by motion-scaling teleoperation. The task involves manoeuvering a microneedle such that its tip is dipped into a series of upright tubes. Since very fine motions are involved, it is expected that the operator's ability to perform the task will be improved by motion scaling. However, without perfectly transparent teleoperation, it is also expected that performance will be adversely affected by the indirection of the teleoperation itself. Therefore, this trade-off should yield improved performance at large scaling factors, and reduced performance as scaling is decreased.

4.3.1 Apparatus

The experimental apparatus consists of a "background material" made from a piece of white paper marked with a 3 mm $\times$ 3 mm grid ruled every 0.5 mm, with tick marks every 0.2 mm. The background material is mounted onto a stiff cardboard backing which is secured by adhesive tape to the operating table. Standing in the middle of the grid

are three segments of surgical tubing mounted upright, and fixed in place using rubber cement (see Figure 4.1). Each segment of tubing is 1 mm tall, with an outside diameter of 0.5 mm and an inside diameter of 0.3 mm. A spatula microneedle from an *Ethicon TG140-6 Plus* microsuture is parked in a piece of soft foam just above the grid. The body of the microneedle is coated with a thin layer of rubber cement to improve the grip.

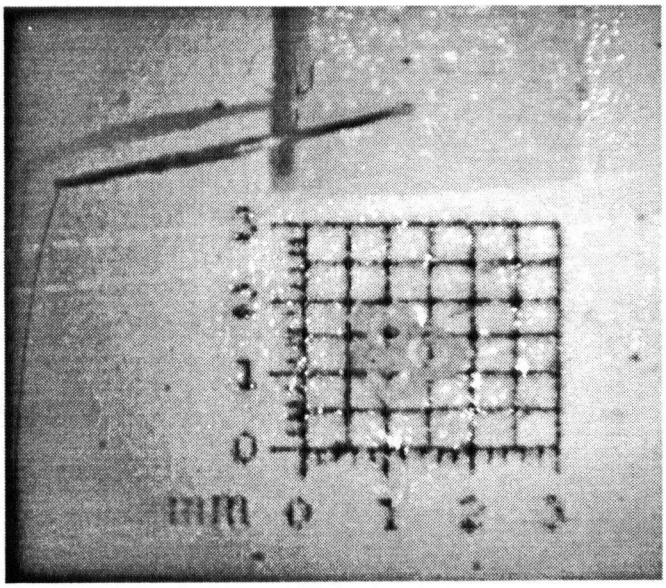

Figure 4.1: Apparatus for motion-scaling experiment

4.3.2 Task

The test subject picks up the microneedle, holding the tip downward in an approximately vertical orientation, and positions it below the level of the tube openings, at least one grid-square away. This is the home position.

When instructed to begin, the subject dips the tip of the microneedle into the opening of each of the three tubes, avoiding contact with the tubes and background material. The depth to which the tip of the microneedle is inserted is not important, as long as it actually enters the opening of the tube. The tubes may be traversed in any order.

Visual feedback is provided through a Carl Zeiss OpMi-8 stereo operating microscope, and magnification is up to the discretion of the test subject.

The task is performed for a prescribed number of repetitions under the following experimental conditions (not necessarily in this order):

- Teleoperation system, position scaling = 6:1;
- Teleoperation system, position scaling = 4:1;
- Teleoperation system, position scaling = 2:1;
- and Conventional forceps (Dumont #5).

The manipulators of the fine-motion stage of the motion-scaling teleoperation system are fixed to the operating table as shown in Figure 4.2. The coarse-motion stage is not used. The PID-based controller described in Section 3.3.4 is used without feedforward of hand and environment forces since contact force is not an issue in this experiment. Hand tremor is low-pass filtered at 10 Hz.

Since the teleoperation system is fixed to the table in this experiment, the workspace is limited. Therefore, when using the teleoperation system, the grid/tubing apparatus is mounted on an x-y-z positioning platform which can be adjusted by the experimenter prior to task execution, according to the instructions of the test subject.

4.3.3 Performance Evaluation

To measure manual dexterity, performance is evaluated in two ways: *completion time* measures the ease and efficiency with which the task is performed, and the number of *task errors* reflects the quality or accuracy of the task execution. Completion time is measured using a real-time software timer activated by a start/stop switch operated by

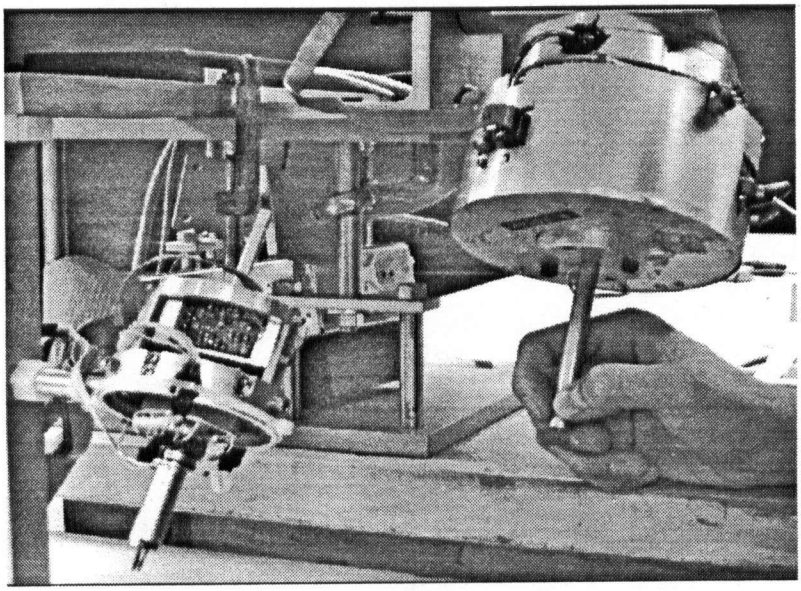

Figure 4.2: Fine-motion stage fixed to operating table

the experimenter. Task errors are scored visually by the experimenter: one task error is counted for each tube that comes into contact with the microneedle. Therefore, the test subject could score a minimum of 0 and maximum of 3 task errors for each execution of the task.

Timing starts when the experimenter instructs the subject to begin, and stops once all three tubes have been traversed. The experimenter monitors progress through the assistant microscope, and records the number of task errors. Unlimited practice time is allowed. The task is performed to the subject's satisfaction, and the best five performances (those with the least number of task errors) are used.

4.3.4 Results

Ten subjects were tested, 3 women and 7 men, mostly graduate students in robotics. Average age was 29.1 years. None were trained in microsurgery, and most had no experience using teleoperation systems. For each subject and experimental condition, the

best five performances were averaged to yield a single mean performance for each experimental condition. Figures 4.3 and 4.4 show the mean number of task errors and mean task completion times averaged over all subjects. The error bars represent the standard deviation in task completion time among subjects.

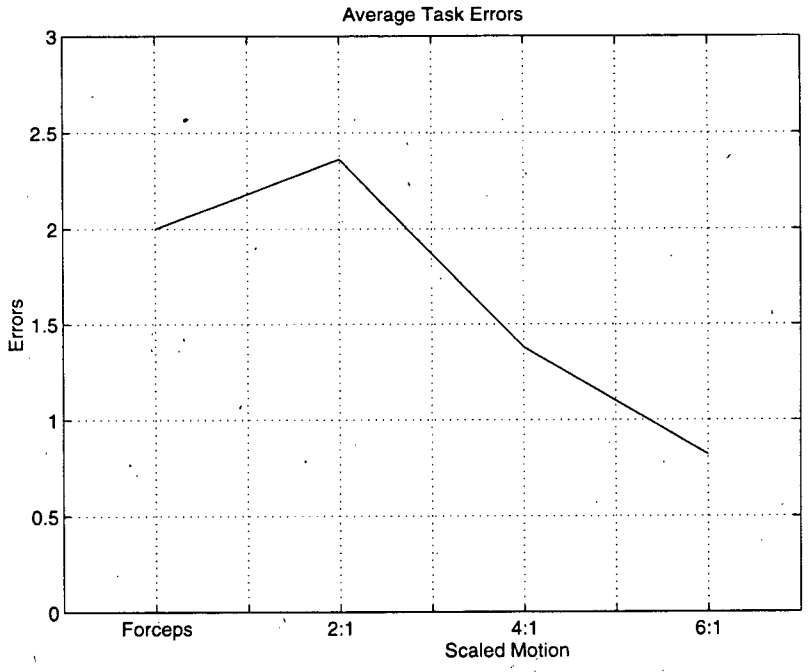

Figure 4.3: Average number of task errors in motion-scaling experiment

The quality of task execution was significantly improved in the presence of motion scaling. Indeed, the average number of task errors with 6:1 motion scaling was 59% less than the that using hand-held forceps. As expected, the performance gain provided by motion scaling decreases as motion scaling is also decreased. At a scaling of 2:1, performance was actually worse than that using conventional forceps, suggesting that under the given experimental conditions, the benefit provided by motion scaling was superseded by the encumbrance of teleoperation.

The effect of motion scaling on task efficiency is not as clear. However, it is apparent that teleoperation had a negative effect on the efficiency of task execution, as

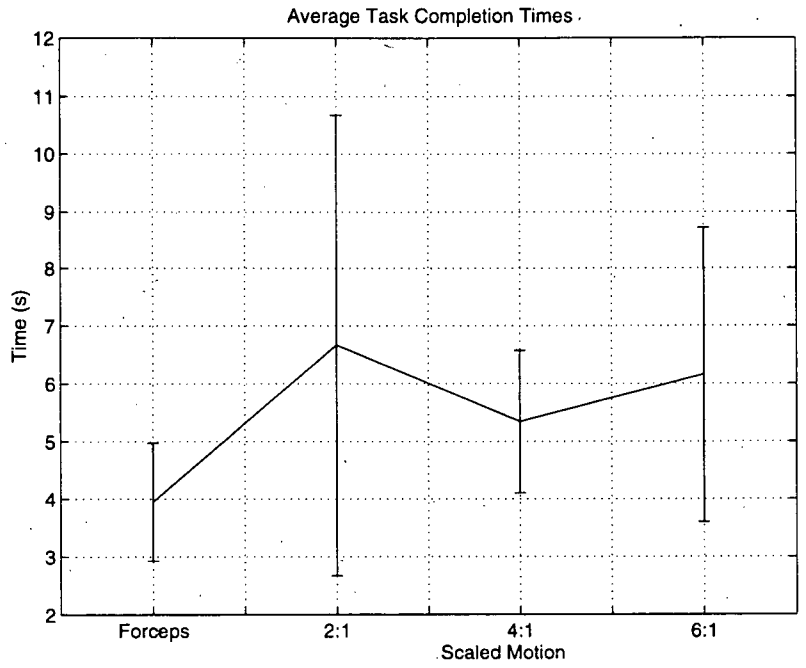

Figure 4.4: Average task completion times in motion-scaling experiment

expected. This effect should be reduced with the development of teleoperation controllers that provide improved transparency. Nevertheless, the improved manipulation capabilities provided by motion scaling should have an indirect impact on the efficiency of microsurgery through reduced tissue trauma and improved first-time success of various fine-motion tasks.

This experiment also demonstrates that completion time taken alone as a measure of performance is not necessarily adequate for mission-critical tasks where quality of task execution is also important. Other factors such as fatigue, ergonomics, and tool-tissue forces are also relevant, but are much more difficult to measure and quantify. The following experiment addresses some of these issues by investigating how scaled force feedback affects the control of small tool-tissue forces.

4.4 Scaled Force Feedback Experiment

The previous experiment illustrated how scaled motion and teleoperation can affect one's ability to control fine motions. This section describes an experiment that measures the effects of scaled force feedback on the control of small tool-tissue forces. The experiment involves applying a prescribed amount of tool-tissue force using either the hand-held microgripper or the motion-scaling teleoperation system. The tool-tissue force is measured using the ATI force/torque sensor, and the difference between the intended force and the actual applied force is recorded over a time interval of approximately 6 seconds.

4.4.1 Apparatus

The "tissue" is simulated by a thin piece of latex rubber (taken from a surgical glove) stretched over an aluminum ring. The latex possesses a compliance similar to that of real tissue, and is commonly used by microsurgeons to practice suturing. The tools used were the hand-held microgripper (shown in Figure 2.11), and the motion-scaling teleoperation system with microgripper (shown in Figure 4.2). Both instruments were equipped with the ATI force/torque sensor to measure tool-tissue force.

4.4.2 Task

The test subject is instructed to apply a prescribed amount of force to the "tissue", and to maintain that force for at least 6 seconds. The force is applied and measured along one axis only—the axis of the instrument, in a vertical orientation. The subject practices applying 3, 9, and 15 grams force while provided with a graphical display of the tool-tissue force, in the form of an oscilloscope-type display on a CRT. Unlimited practice time is allowed.

During testing, the graphical display is removed. Detailed visual feedback is provided

through an operating microscope, and both practice and testing are performed on the same area of latex. The experiment is designed in this way to simulate the situation of a surgeon who is intimately familiar with his or her operating environment. The relatively simple task of becoming familiar with the "look and feel" of applying a few different forces to a single object enabled the test subjects to become very proficient in a short period of time.

4.4.3 Performance Evaluation

During testing, the subject is asked to apply either 3, 9, or 15 grams force using either the hand-held microgripper or the motion-scaling teleoperation system. Once the subject feels that the intended force has been attained, the experimenter records the tool-tissue force for a period of 6.7 seconds (sampling period $dt = 6.7$ ms, $N = 1000$). This data is used to gauge the accuracy with which the subject is able to reproduce the intended force. The subject is then asked to rate the experience as far as confidence and fatigue, where:

Confidence:	10 =	Fully confident that the intended force was attained
	0 =	Not confident that the intended force was attained
Fatigue:	10 =	Not tiring
	0 =	Tiring

This procedure is repeated twice, each time using a different level of force in a randomized sequence. Then, the entire process is repeated using the other instrument.

4.4.4 Results

Ten subjects were tested, 2 women and 8 men, mostly graduate students in robotics. Average age was 28.2 years. None were trained in microsurgery, and most had no experience using teleoperation systems. The sum of squared error (SOSE) was used to measure

the error in applied force for each subject:

$$SOSE = \sum_{i=1}^{N} (f_i - f_{intended})^2 dt \quad . \tag{4.37}$$

This is similar to the SOSF measure (refer to Section 4.2.2). Figure 4.5 shows the mean and standard deviation over all subjects' SOSE scores. The plot shows that the average SOSE scores are much lower where scaled force feedback has been provided. The statistical significance of the results was evaluated using a one-tailed, two-correlated-sample t test. This was used to test the null hypothesis, H_0: that the SOSE without scaled force feedback is in reality at least as small as that *with* scaled force feedback. For the 9 g and 15 g tasks, H_0 was rejected at the 5% level[1]. There was insufficient evidence to reject the null hypothesis for the 3 g case.

When subjects used the hand-held instrument, control of tool-tissue force relied almost entirely on visual feedback alone. Virtually no kinesthetic feedback was available. Based on subjects' testimonies, this dependency placed more strain on both the hand and the eyes. This is reflected in the confidence and fatigue scores. The average confidence and fatigue levels among all test subjects are shown in Figure 4.6. Scaled force feedback appears to have had a marked affect here as well. Again, using the one-tailed, two-correlated-sample t test, the statistical significance of the results was confirmed. The null hypothesis—that the confidence and fatigue scores in the absence of scaled force feedback are at least as good as those *with* scaled force feedback—was rejected at the 5% level in all cases.

Although the mapping of test subjects' qualitative sensations to quantitative scores is imperfect, the results nonetheless illustrate the dramatic effect that scaled force feedback can have on a simple, one-degree-of-freedom task. Similar results can be expected for

[1] A *significance level* of $\alpha = 0.05$ represents the probability level at which the null hypothesis, H_0, can be rejected

manipulation in six or more degrees of freedom, where the magnified feedback of small forces and torques can aid the operator in controlling small motions and contact forces.

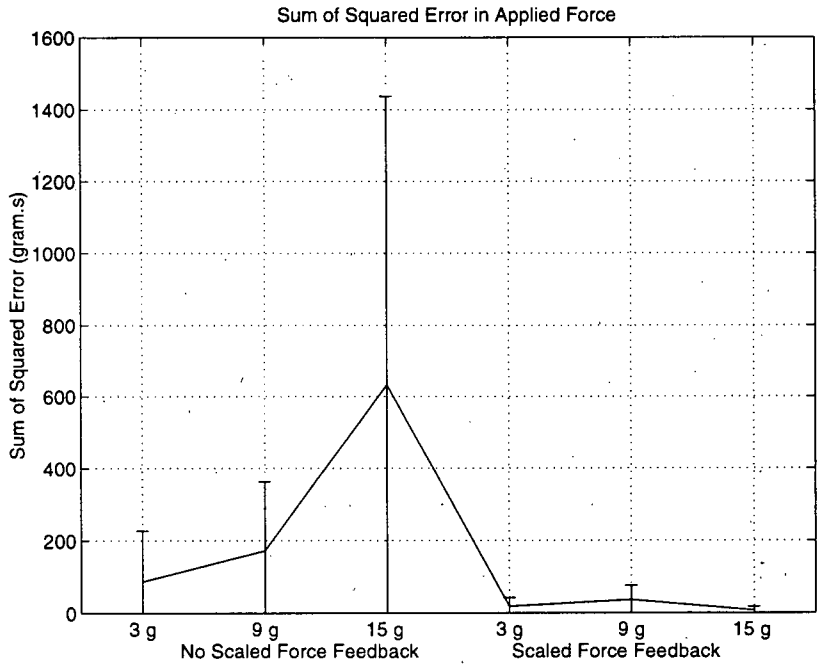

Figure 4.5: Sum of squared error in applied force for all test subjects

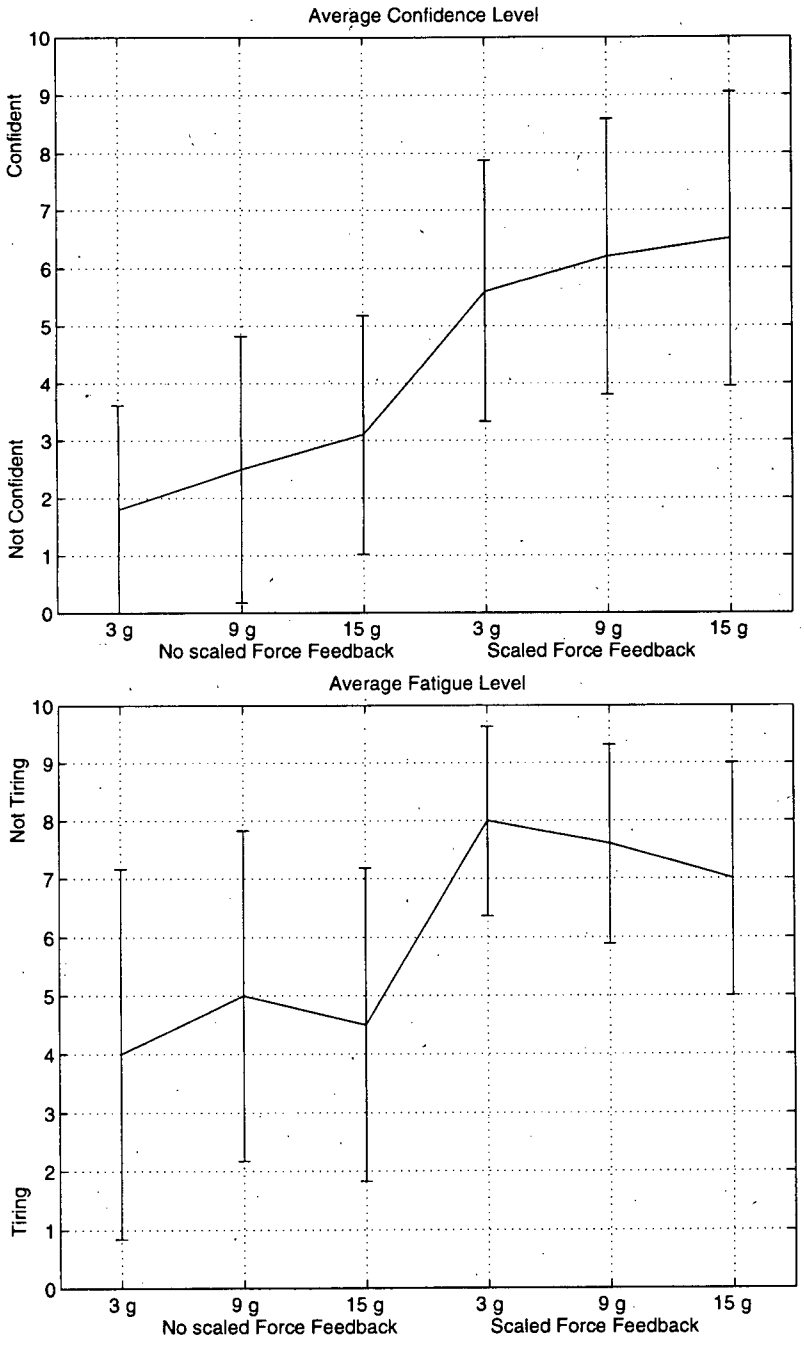

Figure 4.6: Average confidence levels (top) and fatigue levels (bottom) for all test subjects

4.5 Motions and Forces in Microsurgery

Presently, there is relatively little knowledge of the motions and forces used in microsurgery. Indeed, the single problem of instrumenting tools for measuring these motions and forces is non-trivial. As a result, up to now, these types of measurements have only been obtained in a limited manner [23, 38]. A good understanding of the motions and forces that are used in microsurgery would be valuable in many ways:

- measurements of motions and forces could be used to assist the training of microsurgeons;
- information regarding workspace and tool-tissue forces would be invaluable for the design and evaluation of microsurgical instrumentation;
- measurements can be used to construct accurate computer models of living tissue for microsurgery planning and training;
- and measurements could be used to determine the mechanical properties of different types of vessels and tissues (e.g., artery, vein, nerve), thereby enabling the microsurgeon to reduce the possibility of trauma to tissues if force-sensitive instruments such as the microgripper are used.

Clearly, new devices are needed to accurately measure tool-tissue forces in a wide range of microsurgical tasks. The hand-held microgripper (refer to Figure 2.12) is one such device. It is simple to operate, and could easily be used in place of conventional forceps. Equipped with the ATI force/torque sensor, the microgripper enables the measurement of microsurgical forces resolved into gripping force and 6-DOF "wrist" force components. For illustration, the next section presents an experiment that was conducted using the hand-held microgripper to measure tool-tissue forces during a simulated microsurgical task.

4.6 Simulated Microsurgery Experiment

In this experiment, tool-tissue forces are recorded while a simulated microsurgical task is performed. The task involves gently grasping and pulling the adventitia of a blood vessel, simulated here by a thin sheet of latex. This type of activity is extremely common in reconstructive microsurgery, where one primary activity is vascular anastomosis. The adventitia and any other superfluous perivascular tissue must be removed before the vessel can be sutured.

4.6.1 Apparatus

The experimental set-up consists of a sheet of latex taken from a surgical glove mounted on a rigid paper frame, with a 15 mm-long slit made in the latex. This "slit latex" set-up is commonly used by microsurgeons for training in suturing. The task involves approaching the operating site, grasping the edge of the slit, pulling it gently, and then releasing it (see Figure 4.7). Visual feedback is provided through a Carl Zeiss OpMi-8 stereo operating microscope with power zoom and focus.

The hand-held microgripper equipped with the ATI force/torque sensor is used to measure tool-tissue forces in seven degrees of freedom while the task is executed. Ideally, tool positions would also be measured on-line using a 6-DOF motion-tracking system [39]. Since this was unavailable, the task was repeated using the motion-scaling teleoperation system, and position data was recorded in order to provide a general idea of the motions involved.

4.6.2 Results

The data obtained from the hand-held microgripper are shown in Figure 4.8. The top plot shows the gripping force while the "adventitia" is grasped and released, and the

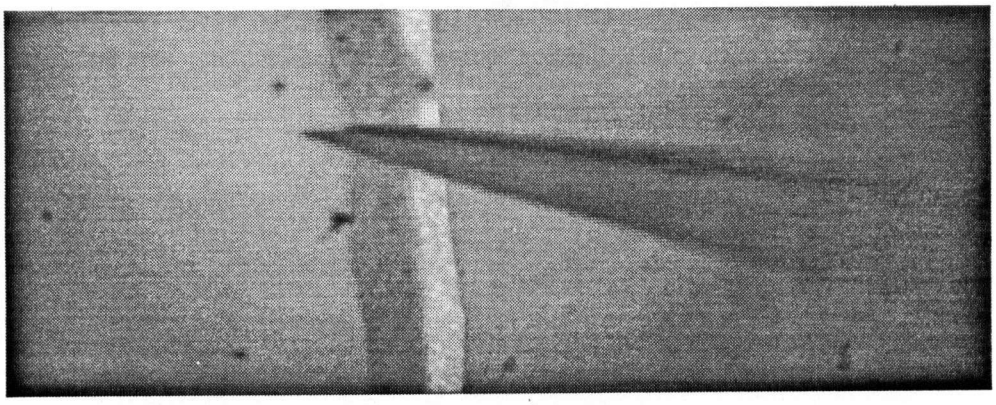

Figure 4.7: Simulated adventitia grasped and pulled

other plots show the "wrist" forces and torques. Figure 4.9 shows the same parameters recorded when the teleoperation system was used to perform the task. The slave manipulator position and orientation are also given in Figure 4.9. Note that the positions and orientations are expressed with respect to the stator coordinate frame, which is rotated 60° from the horizontal plane (refer to Figure 4.2).

Since the experimental environment was artificial and the test subject was untrained in microsurgery, the motions and forces exercised here may not necessarily correspond to those used by a trained microsurgeon under real conditions. However, the results show that accurate measurement of these parameters is possible. Future experiments involving experienced microsurgeons working in real microsurgical environments should yield valuable information.

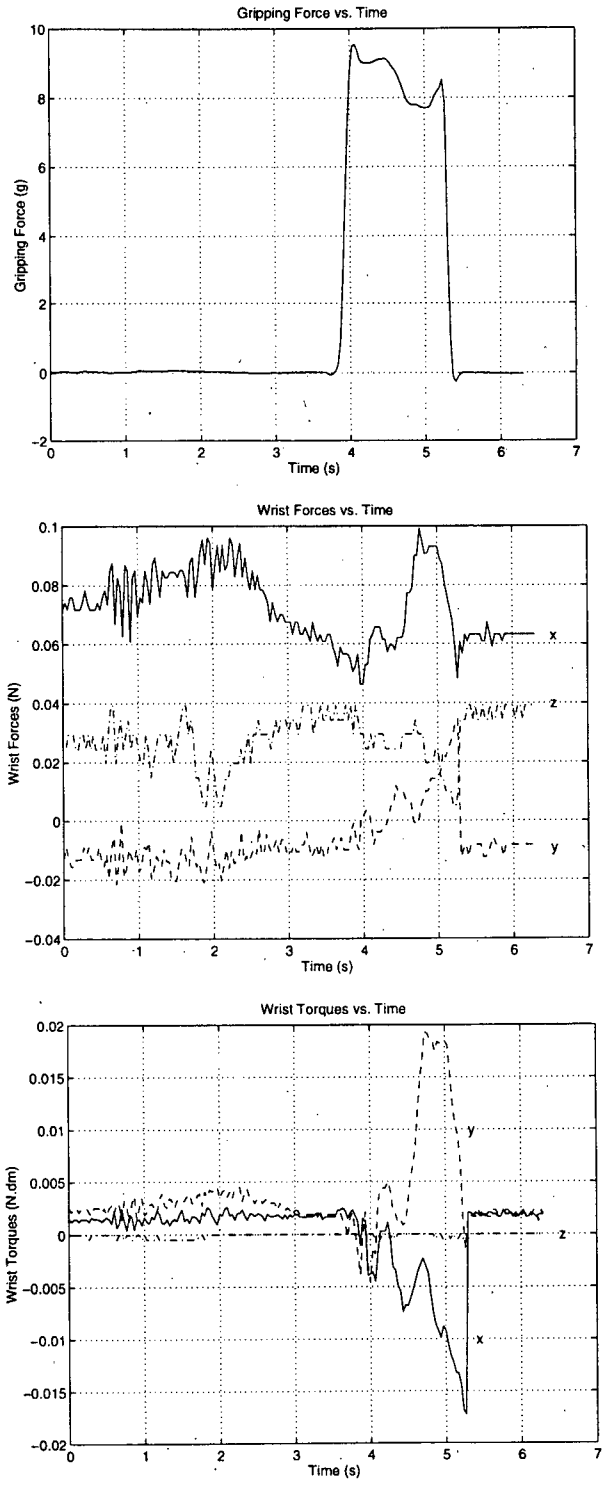

Figure 4.8: Hand-held microgripper: gripping force (top); wrist forces (middle); and wrist torques (bottom)

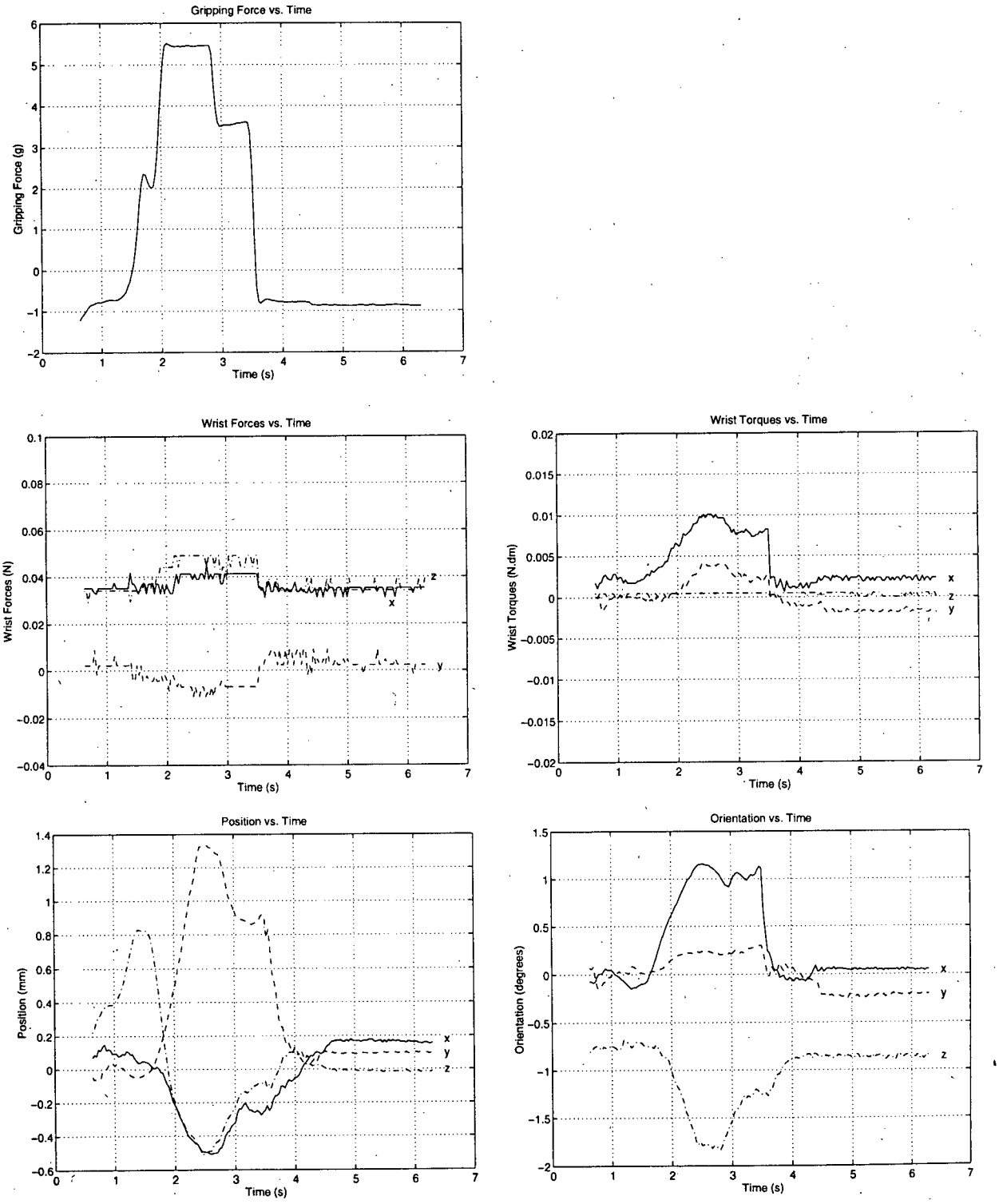

Figure 4.9: Teleoperation system: gripping force, wrist forces and torques (left); position orientation of slave manipulator (right)

Chapter 5

Conclusions

5.1 Contributions

The contributions of this work are three-fold. First, the design of a teleoperated microgripper has been presented, and different approaches to control have been demonstrated. This lightweight, compact device can be used as the end-effector of a hand-held instrument, a "third-hand" tool, or a telerobotic motion-scaling system. The microgripper and its teleoperation master possess several useful features, and offer some advantages over conventional forceps:

1. Scaling and digital filtering of the force measured at the surgeon's fingers can minimize the effect of hand tremor on the motion of the microgripper. This alone could greatly extend the resolution with which a microsurgeon can achieve smooth, controlled gripping motions.

2. Force sensing enables the application of programmable force limits to reduce the possibility of trauma to tissues. Furthermore, control methods can be used to emulate different physical mechanisms such as a hemostat.

3. The microgripper enables the measurement of microsurgical forces resolved into gripping force and 6-DOF wrist force components. The mechanical decoupling of the surgeon's finger motion from that of the microgripper also makes it possible for the microsurgeon to employ different grasps of the tool.

4. The microgripper handle is stiffer than conventional forceps, and requires only a light squeeze to control the microgripper. This should reduce hand fatigue and enable steadier fine-resolution control.

5. The microgripper design is compact, lightweight, and scalable. Stroke and force are relatively high compared to other designs, and control of gripping force is fast and simple. The basic design can be modified to make other alternative instruments for microsurgery and micro-manipulation.

6. The microgripper can be inexpensively manufactured, making commercialization a viable possibility.

Second, force/torque sensing at the master and slave has been integrated with the fine-motion stage of the UBC Motion-Scaling Teleoperation System, and three different controllers have been implemented for bilateral control. These controllers each possess attributes that could potentially be useful for microsurgery: high-fidelity force reflection, remote centre of compliance emulation, and static friction emulation.

Finally, the experimental evaluation of motion-scaling teleoperation performance has been discussed, as has the measurement of motions and forces in microsurgery. Experimental results indicate that motion scaling can dramatically improve the accuracy with which one can execute a task that requires controlled sub-millimetre movements. Furthermore, scaled force feedback can improve a person's ability to control tool-tissue forces. Other benefits include increased confidence and reduced fatigue.

5.2 Future Work

The microgripper and teleoperation system described here offers the possibility of improved dexterity for fine-motion manipulation by providing scaled motion and scaled

kinesthetic feedback. The following are recommended as directions for future work:

- Some of the individual components of the teleoperation system possess strong potential for use in a broad range of applications in research and in industry. Now is a good opportunity to refine their design, control, and construction in order to make them practical for a variety of commercial applications.

  For example, the microgripper would be an inexpensive instrument that could provide a practical means for manipulating delicate objects in minimally-invasive surgery, biological research, industrial robotics, and other areas. Migrating the original design to commercial production would not be difficult, and may serve as a catalyst for the design of other alternative instruments for small-scale manipulation. In addition, modifications to the original microgripper design could yield other useful tools. For example, the gripping arms could be altered in order to perform tasks such as cutting, coagulating, and needle-holding. As mentioned earlier, the design could be miniaturized for use in laparoscopy, and different force and displacement capabilities can be achieved using different geometries and actuation methods.

- A force-feedback master for the microgripper should not be difficult to construct using, for example, a miniature solenoid actuator. Visual and auditory displays of gripping force can also be tried.

- The motion-scaling teleoperation system offers a great opportunity for work in teleoperation, enabling the implementation and evaluation of different controllers. In future work on teleoperation controller design, quantitative measures of system performance, such as those proposed by Hannaford [40], would be useful.

- Further human-factors experiments will provide a better understanding of how manual dexterity is affected by scaled motion, scaled force feedback, and teleoperation in a variety of tasks relevant to microsurgery. The experiments presented here show how teleoperation performance can be quantified experimentally. Future experiments should reveal the practical merits of different control schemes (e.g., RCC, static friction emulation), and should provide valuable insight into various human-factors related design issues.

- The measurement of microsurgical tool-tissue forces in 7-DOF is now possible using specially instrumented tools such as the hand-held microgripper. Experiments that measure the motions and forces experienced during microsurgery would enable a more thorough understanding of microsurgery and anatomy. This could be valuable for training microsurgeons, and for the further development of instrumentation for microsurgery.

Bibliography

[1] S.E. Salcudean and J. Yan, "Towards a force-reflecting motion-scaling system for microsurgery," in *Proceedings of the 1994 IEEE International Conference on Robotics and Automation*, vol. 3, pp. 2296–2301, May 1994.

[2] R.K. Daniel and J.K. Terzis, *Reconstructive Microsurgery.* Little, Brown and Company, 1977.

[3] J.M. Parel, G.W. Crock, B.M. O'Brien, P.N. Henderson, and J.E.K. Galbraith, "Prototypal electro-microsurgical instruments," *The Medical Journal of Australia*, vol. 1, pp. 709–714, 1970.

[4] H.J. Buncke and W.P. Schulz, "Total ear reimplantation in the rabbit utilizing microminature vascular anastomoses," *British Journal of Plastic Surgery*, vol. 19, pp. 15–22, 1966.

[5] I.W. Hunter, S. Lafontaine, P.M.F. Nielsen, P.J. Hunter, and J.M. Hollerbach, "A microrobot for manipulation and dynamical testing of single living cells," in *Proceedings of the IEEE Workshop on Micro Electro Mechanical Systems*, (Salt Lake City), pp. 102–106, February 1989.

[6] R.L. Hollis, S. Salcudean, and D.W. Abraham, "Toward a tele-nanorobotic manipulation system with atomic scale force feedback and motion resolution," in *Proceedings of the IEEE Workshop on Micro Electro Mechanical Systems*, pp. 115–119, 1990.

[7] S. Charles, R.E. Williams, and B. Hamel, "Design of a surgeon-machine interface for teleoperated microsurgery," in *IEEE Engineering in Medicine and Biology Society 11th Annual International Conference*, 1989.

[8] P.S. Schenker, E.C. Barlow, C.D. Boswell, H. Das, S. Lee, T.R. Ohm, E.D. Paljug, G. Rodriguez, and S. Charles, "Development of a telemanipulator for dexterity enhanced microsurgery," in *MRCAS '95*, pp. 81–88, 1995.

[9] M. Mitsuishi, T. Watanabe, H. Nakanishi, T. Hori, H. Watanabe, and B. Kramer, "A tele-micro-surgery system with co-located view and operation points and a rotational-force-feedback-free master manipulator," in *MRCAS '95*, pp. 111–118, 1995.

[10] T. Sato, J. Ichikawa, M. Mitsuishi, and Y. Hatamura, "A new micro-teleoperation system employing a hand-held force-feedback pencil," in *Proceedings of the 1994 IEEE International Conference on Robotics and Automation*, vol. 2, pp. 1728–1733, 1994.

[11] J.A. McEwen, "Solo surgery with automated positioning platforms," in *Presentation for New Frontiers in Minimally Invasive and Interventional Surgery Conference*, October 1992.

[12] R. Hurteau, S. DeSantis, E. Begin, and M. Gagner, "Laparoscopic surgery assisted by a robotic cameraman: Concept and experimental results," in *Proceedings of the 1994 IEEE International Conference on Robotics and Automation*, vol. 3, pp. 2286–2289, 1994.

[13] L.R. Kavoussi, R.G. Moore, J.B. Adams, and A.W. Partin, "Comparison of robotic versus human laparoscopic camera control," in *MRCAS '95*, pp. 284–287, 1995.

[14] T. Fukuda, K. Tanie, and T. Mitsuoka, "A new method of master-slave type of teleoperation for a micro-manipulator system," in *Proceedings – IEEE Micro Robots and Teleoperators Workshop. Investigation of Micromechanical Structures, Actuators, and Sensors*, November 1987.

[15] T. Maruyama, S. Kanda, M. Sato, and T. Uchiyama, "Development of hand-eye system with 3-d vision and microgripper and its application to assembling flexible wires," in *Proceedings of CVPR '89, IEEE Computer Society Conference on Computer Vision and Pattern Recognition*, pp. 680–685, 1989.

[16] Microflex Technology, Inc., "Mg-1000 microgripper product literature." Distributed by Bunton Instrument Co., Inc., 615 South Stonestreet Avenue, Rockville, MD 20850, (301) 762-5115.

[17] K. Ikuta, A. Kawahara, and Y. Tsutsui, "Development of minature cybernetic actuator driven by piezoelectric device," in *IEEE/RSJ International Workshop on Intelligent Robots and Systems IROS '91*, pp. 1151–1156, 1991.

[18] J.S. Schoenwald, P.M. Beckham, R.A. Rattner, B. Vanderlip, and B.E. Shi, "End effector actuation with a solid state motor," in *Proceedings of the 1988 IEEE International Conference on Robotics and Automation*, vol. 1, pp. 108–113, 1988.

[19] K. Ikuta, "Micro/miniature shape memory alloy actuator," in *Proceedings of the 1990 IEEE International Conference on Robotics and Automation*, vol. 3, pp. 2156–2161, 1990.

[20] J. Yan, "Design and control of a bilateral motion-scaling system using magnetic levitation," Master's thesis, The University of British Columbia, 1994.

[21] Chia-Tung Chen. UBC Maglev Wrist assembly drawing.

[22] S.E. Salcudean, N.M. Wong, and R.L. Hollis, "A force-reflecting teleoperation system with magnetically levitated master and wrist," in *Proceedings of the 1992 IEEE International Conference on Robotics and Automation*, pp. 1420–1426, 1992.

[23] S. Charles and R. Williams, "Measurement of hand dynamics in a microsurgery environment: Preliminary data in the design of a bimanual telemicro-operation test bed," in *NASA Conference on Space Telerobotics Proceedings*, pp. 109–118, 1989.

[24] International Standards Organization, "Iso10993 – biological evaluation of medical devices." available from the Standards Council of Canada.

[25] Toxicological Subgroup of the Tripartite Subcommittee for Medical Devices, "Tripartite biocompatibility guidance for medical devices." in Health Protection Branch Information Letter No. 737, Health Canada.

[26] S. Majima and K. Matsushima, "On a micro-manipulator for medical application—stability consideration of its bilateral controller," *Mechatronics*, vol. 1, no. 3, pp. 293–309, 1991.

[27] J. Palm and K. Thomas, "Design equations for curved springs," in *Spring Design and Application* (N.P. Chironis, ed.), pp. 108–109, McGraw-Hill, 1961.

[28] F. Tendick and L. Stark, "Analysis of the surgeon's grasp for telerobotic surgical manipulation," in *IEEE Engineering in Medicine and Biology Society 11th Annual International Conference*, pp. 914–915, 1989.

[29] Zeppelin Micro-Instrumente, "Product information." Zeppelin Medizintechnik GmbH, 8000 München 5, Germany.

[30] R. L. Hollis, S. E. Salcudean, and A. P. Allan, "A six-degree-of-freedom magnetically levitated variable compliance fine-motion wrist: design, modeling, and control," *Proceedings of the 1991 IEEE International Conference on Robotics and Automation*, vol. 7, pp. 320–332, June 1991.

[31] S.E. Salcudean and T. Vlaar, "On the Emulation of Stiff Walls and Static Friction with a Magnetically Levitated Input-Output Device," in *Proceedings of the International Mechanical Engineering Congress and Exposition*, vol. DSC-Vol. 55-1, (Chicago, USA), pp. 303–309, November 6-11 1994.

[32] P.J. Hacksel, "Observer based velocity and environment force estimation for rigid body control," Master's thesis, The University of British Columbia, 1993.

[33] P.J. Hacksel and S.E. Salcudean, "Estimation of environment forces and rigid-body velocities using observers," in *Proceedings of the 1994 IEEE International Conference on Robotics and Automation*, vol. 2, pp. 931–936, May 1994.

[34] T. Vlaar, "Mechanism emulation with a magnetically levitated input/output device," Master's thesis, The University of British Columbia, 1994.

[35] B. Hannaford, L. Wood, D. McAffee, and H. Zak, "Performance evaluation of a six-axis generalized force-reflecting teleoperator," *IEEE Transactions on Systems, Man, and Cybernetics*, vol. 21, pp. 620–633, May/June 1991.

[36] W.S. Kim, B. Hannaford, and A.K. Bejczy, "Force-reflection and shared compliant control in operating telemanipulators with time delay," *IEEE Transactions on Robotics and Automation*, vol. 8, pp. 176–185, April 1992.

[37] D.W. Repperger, S.J. Remis, and G. Merrill, "Performance measures of teleoperation using an exoskeleton device," in *Proceedings of the 1990 IEEE International Conference on Robotics and Automation*, pp. 552–557, 1990.

[38] C.C. Collins, A. Jampolsky, A.B. Alden, M.B. Clarke, S.T. Chung, and S.V. Clarke, "Length-tension recording system for strabismus surgery," *IEEE Transactions on Biomedical Engineering*, vol. 38, March 1991.

[39] Kinetic Sciences Inc., "Eagle eye 7d motion tracking software," 1995. 3520 Main Mall, Vancouver, B.C. V6T 1W5.

[40] B. Hannaford, "A design framework for teleoperators with kinesthetic feedback," *IEEE Transactions on Robotics and Automation*, vol. 5, pp. 426–434, August 1989.

[41] R.F. Morrissey and G.B. Phillips, eds., *Sterilization Technology: A Practical Guide for Manufacturers and Users of Health Care Products.* Van Nostrand Reinhold, 1993.

[42] Sytek. 116 - 980 West 1st Street, North Vancouver, B.C., V7P 3N4.

[43] W.L. Gore & Associates, Inc., Electronic Products Division. 4747 East Beautiful Lane, Phoenix, AZ, 85044-9914, (602) 431-0077.

[44] Flex-Link Products, Inc. 599 Fourth Street, San Fernando, CA 91340, (818) 898-1451.

[45] Merix Corporation. 1521 Poplar Lane, P.O. Box 3000 FI-394, Forest Grove, Oregon 97116.

[46] Advanced Circuit Technology, Inc. 118 Northeastern Boulevard, Nashua, NH 03062, (603) 880-6000.

[47] Noble USA, Inc. 5450 Meadowbrook Industrial Court, Rolling Meadows, IL 60008.

[48] Digi-Key Corporation. 701 Brooks Ave. S., P.O. Box 677, Thief River Falls, MN 566701-0677, 1-800-344-4539.

[49] Phoenix Wire, Inc. 31 Tracey Road, P.O. Box 186, South Hero, Vermont 05486.

[50] Calmont Engineering & Electronics Corp. 420 East Alton Avenue, Santa Ana, CA 92707.

[51] Assurance Technologies, Inc., *Installation and Operations Manual for F/T.* 1993.

[52] Motorola, *MC68230 Parallel Interface/Timer.* 1983.

[53] Xycom, *XVME-200 I/O Interface Board.* 1987.

Appendix A

Microsurgical Instrumentation and Procedures

Instrumentation

Forceps are available in various shapes and sizes, and are usually made of non-magnetic stainless steel or titanium since magnetized instruments are undesirable in the presence of steel microneedles. The No. 5 jeweler's forceps is commonly used for general manipulation of delicate tissue (see Figure A.1).

Microsurgical needle holders have been designed to provide a solid grip on a microneedle. Most needle holders possess scissor-like shanks, and tapered, curved jaws whose flat surfaces close together to form a secure gripping surface with the microneedle (see Figure A.1). The No. 5 forceps is not used to drive microneedles since the inner surface of its tips, or "bit", possesses insufficient gripping surface to maintain a firm hold on a microneedle. However, the No. 2 forceps offers greater gripping surface, and is actually preferred by some microsurgeons over scissor-like needle holders for several reasons: cost; simplicity of the mechanism; reduced chance of suture entanglement; and ease of knot tying since both suture placement and tying can be accomplished with the same instrument.

Microsutures are used primarily to hold tissues together until natural healing can do so permanently. A typical application is *vascular anastomosis*, which involves the suturing of vessels. Virtually all microsutures used today are each composed of a stainless steel microneedle swaged (i.e., crimped) onto a nonabsorbable suture material, usually made

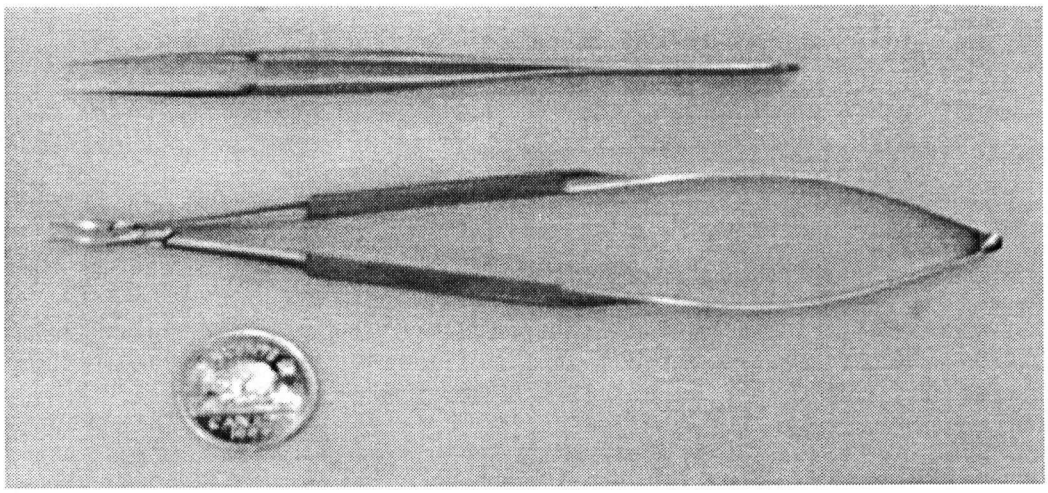

Figure A.1: Forceps (top) and needle holder (bottom)

from a form of nylon.

Clamps are used primarily to temporarily occlude blood flow in vessels in order to permit suturing. Although total occlusion of blood flow is necessary, it is also important to not apply excessive force to the vessel. 30 g/mm is generally accepted as the maximum pressure tolerable by small vessels in order to avoid significant endothelial trauma, which could lead to thrombosis[1]. The commonly used Acland clamp is available in closing tensions of 10, 15, or 25 g. Angled clamps, such as the Heifetz clamp, are also frequently used in conjuction with "wrappers" (e.g., Saran Wrap) in order to provide watertight closure and support for the sutured vessel in arterial anastomosis.

A *clamp-approximator* consists of two clamps mounted on a bar or frame (see Figure A.2). Both movable and non-movable models exist. Clamp-approximators serve two purposes: to temporarily occlude blood flow from the ends of the vessel to be sutured; and to hold and align ("approximate") the ends of the vessel to facilitate suturing. The Acland clamp-approximator shown in Figure A.2 features an optional frame with cleats

[1]The aggregation of platelets at an injury site into a solid mass (thrombus) that could obstruct blood flow.

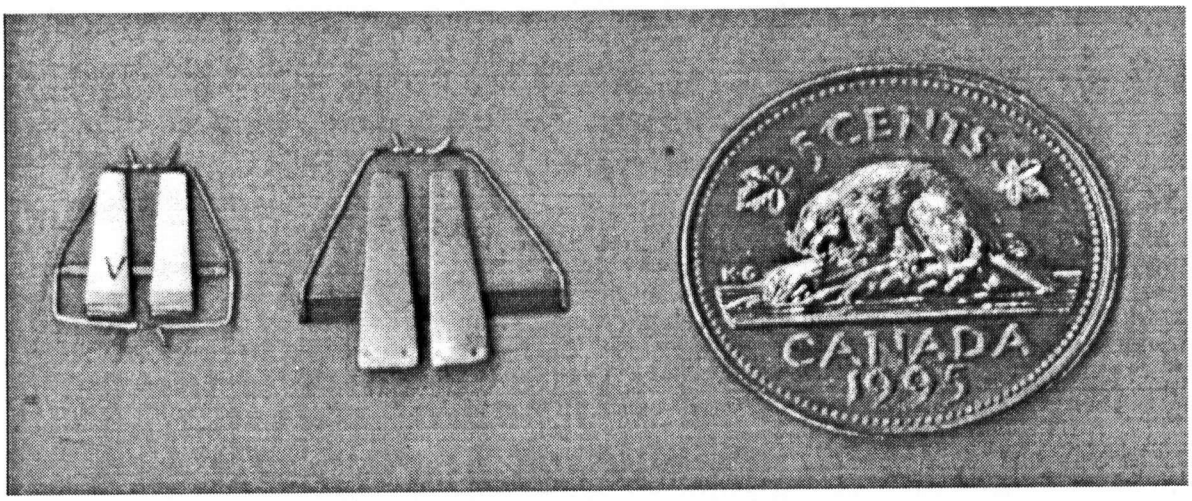

Figure A.2: Acland clamp-approximators

that can be used to secure guide sutures.

Tasks in Microsurgery

In order to provide an idea of the types of tasks used in microsurgery, the following is a description of the steps involved in end-to-end arterial anastomosis, a procedure extremely common in reconstructive microsurgery, where repairing severed vessels is necessary.

1. *Isolate* the vessel from the surrounding tissue. Vessels usually produce spasms as a result of trauma. This can be treated with a topical applicaiton of lidocaine. Saline solution must be used to keep the vessel constantly warm and moist.

2. *Clamp* the vessel using a clamp-approximator to stop bleeding and enable accurate alignment of the severed vessel. Some clamps must be used in conjunction with special "clip forceps".

3. *Insert* a piece of background material underneath the vessels to improve visibility.

4. Using microscissors, *remove* any perivascular tissue, and transect the vessel ends to obtain a clean interface for suturing.

5. *Remove* extraneous adventitia from the ends of the vessel by gently pulling on the adventitia using fine-tipped forceps and cutting it away using microscissors.

6. *Irrigate* the open ends of the vessel using heparinized saline solution (delivered from a blunt needle or plastic catheter held close to the vessel opening) to remove any blood clots or debris.

7. *Cannulate*, or gently dilate, the vessel ends using fine-tipped forceps to faciliate suturing.

8. *Approximate*, or align, the vessel ends in preparation for suturing.

9. *Inspect* the vessel to determine the appropriate location, bite, and number of sutures to be used.

10. *Grasp* the microneedle with the needle holder, and insert the first "guide" suture through the anterior wall of one of the vessel segments. While driving the microneedle through the wall of the vessel, counterpressure is usually provided using forceps (in the nondominant hand) by delicately grasping the adventitia or by gently holding the vessel open as was done for cannulation.

11. *Pass* the microneedle through the wall of the other vessel segment, making sure that the bite and alignment are correct.

12. *Tie* a series of single-throw knots to secure the suture. This is commonly performed using either a needle holder and forceps or two forceps.

13. *Cut* the suture material, leaving a 15 mm tail for applying traction.

14. *Place* another guide suture, and then place one or more interrupted sutures between the guide sutures. Typically, either two or three guide sutures are eventually placed equally spaced around the perimeter of the vessel.

15. *Turn over* the clamp-approximator, and suture the other side of the vessel.

16. *Wrap* the anastomosis with a clear plastic film, and clamp the material in place with an angled clamp. Note: wrappers are not always used.

17. *Remove* the clamp-approximator to restore blood flow in the vessel.

18. Approximately 20 minutes later, *remove* the wrapper, and perform a "patency" test to determine whether or not the anastomosis was successful. The patency can be evaluated either by direct inspection or by a test that involves using two forceps to control blood flow across the anastomosis.

Appendix B

Sterilization Methods

The following is a brief outline of sterilization methods in common use. A more comprehensive treatment of current sterilization theory, instrumentation, and practices is covered in [41].

Dry Heat

This method involves exposing the product to hot air in a chamber whose temperature uniformity is regulated by a fan/blower system. Typically, a temperature of $140 - 170°C$ and an exposure time of $60 - 180$ minutes are required to achieve a 10^{-6} SAL.

In addition to its simplicity, sterilization using dry heat has the advantages of penetrating power, and lack of toxic residues. However, the high temperature and relatively long processing time required may make it unsuitable for certain materials. Products typically sterilized using dry heat include vials, ampules, oils, petrolatum, heat-stable powder pharmaceuticals, and heat-stable products that are sensitive to moisture or cannot be penetrated by steam.

Steam Under Pressure

This technique uses dry saturated steam at a particular temperature and pressure. The uniformity of the temperature distribution is regulated using simple gravity displacement or a vacuum system, which generally produces better steam penetration. A temperature

of $121 - 132°C$ and a pressure of $15 - 19$ psi over $5 - 45$ minutes are typically used.

Although slightly more complex than the dry heat method, using "moist heat" allows lower temperatures and shorter processing times. As with the dry heat method, there are no toxic residues. However, this method is not effective on products that cannot be readily penetrated by steam (e.g., packages with enclosed cavities), and it is unsuitable for materials that are sensitive to moisture. Typical products sterilized using this method include surgical dressings, water for injection, and contact lenses.

Radiation

In radiation sterilization, a dose of gamma rays or accelerated electrons is administered to the product. ^{60}Co and ^{137}Cs are the usual gamma ray sources. A typical dose is $1.5 - 3.5$ Mrad.

This method is expensive, and it requires complex facilities that comply to strict safety standards. Furthermore, the result of a malfunction or accident could be quite serious. Nonetheless, steam, high temperatures, and toxic agents are not required, making this a viable alternative sterilization method for certain materials. Sutures, syringes, dressings, surgical staplers, gloves, gowns, and face masks are commonly sterilized using radiation.

Ethylene Oxide

Ethylene oxide (EtO) is a toxic, mutagenic, and possibly carcinogenic gas that is widely used as a sterilizing agent (sterilant) for non-liquid products. Because EtO is flammable and explosive, it is usually mixed with an inerting agent such as Freon-12^{TM}.

A temperature of $25 - 75°C$, pressure up to 25 psi, and exposure time of $1 - 12$ hours are typically used. In addition, the relative humidity (RH) in the EtO chamber is usually maintained at $40 - 80\%$ in order to ensure good penetration of the gas throughout the

product or packaging.

The environmental implications of using chlorofluorocarbon (CFC) gases such as Freon-12^{TM} make this method undesirable unless sterilization using heat, steam, or radiation are unsuitable. Furthermore, the high cost of the EtO gas is compounded by the cost of implementing the strict environmental controls and proper evacuation and aeration systems necessitated by the toxicity of the gas. Also, improper aeration can result in the presence of unacceptable toxic residuals in the product itself.

The low processing temperature and the wide range of compatible materials are the main advantages of sterilization using EtO. Products commonly sterilized using this method include blood oxygenators, catheters, mechanical heart valves, sutures, tubing sets, and adhesive bandages.

Alternative Gases/Vapours

The toxicity of EtO has lead to the use of alternative gases or vapour sterilization methods. Chlorine dioxide (ClO_2), hydrogen peroxide (H_2O_2), formaldehyde (CH_2O), peracetic acid (PAA), and ozone (O_3) are some sterilants currently used. These substances do not penetrate into many materials as EtO does; thus, residual removal is usually less of a problem than with EtO. However, this reduced penetration also means that these alternative substances can be less effective than EtO.

In addition to possessing the advantages and drawbacks associated with EtO sterilization, these alternative sterilants have the added advantage that only ambient temperatures ($20 - 35°C$) and relatively short exposure times ($0.5 - 3$ hours) are needed.

Chemical Solutions

Liquid chemical germicides are widely used for sterilization, disinfection, decontamination, and antesepsis[1]. Their effectiveness as sterilants yields at best an SAL of 10^{-3}, 1000 times less reliable than heat sterilization (SAL 10^{-6}). Thus, chemical germicides are commonly only used to disinfect some medical devices, instruments, and environmental surfaces. The cost and complexity of this method is relatively low. However, because it is also less reliable, the consequences of improper disinfection can be far more serious than those of improper sterilization using other methods.

Aseptic Processing

Although this method only applies to the sterilization of liquids, it is mentioned here for sake of completeness. Asceptic filtration involves passing the liquid through a sterile microbiological filter. This method does not involve toxic agents and does not cause any thermal stress on the product. However, the processes and controls involved to achieve an SAL of 10^{-3} or better are complex and can be quite costly.

[1] *Sterilization* eliminates all microbial life; *disinfection* destroys virtually all known pathogenic microorganisms on a given inanimate object, but does not necessarily destroy all microbial forms (e.g., bacterial endospores); *decontamination* renders an object safe to handle, but not necessarily safe for patient reuse; and *antisepsis* inhibits or destroys microorganisms on skin or living tissue.

Appendix C

Force/Torque Sensor Wiring and Interface

Wiring

The slave maglev manipulator required flexible cables to wire the flotor coils and LEDs to the stator without creating excessive mechanical loading. For the same reason, flotor-mounted devices such as the ATI force/torque sensor and microgripper needed similar flexible cables.

The availability of miniature, multi-conductor, flat cables was investigated. They had to be small, lightweight, and limp (i.e., not stiff). The latter proved to be the most challenging requirement. Unfortunately, very few off-the-shelf (OTS) products exist. Most of the products reviewed are custom manufactured and only available in very large quantities.

Flat-Conductor Cables

The electrical wiring between the slave flotor and stator was initially accomplished using thin, Kapton-film flat-conductor cables salvaged from a hard disk drive. This type of etched-conductor, flexible PC board is commonly used in devices such as disk drives, printers, and photocopiers, where a moving part must be connected using a flexible, multi-conductor cable. It is also used in touch-panels and notebook computers in order to fit thin, printed circuits into tight spaces. The Kapton substrate provided good flexibility, but its mechanical stiffness introduced significant mechanical loading on the flotor, and

it can only withstand temperatures up to 125 °C.

Companies such as Sytek [42], *W.L. Gore & Associates* [43], Flex-Link Products [44], and Merix [45] custom manufacture a variety of different flat-conductor products using different flexible substrates. However, kapton and mylar-based off-the-shelf flat-conductor circuits are only available with thicker and stiffer, non-etched conductors.

Advanced Circuit Technology [46] and *Noble* ("pinflex" product line) [47] are two sources of off-the-shelf products. *Advanced Circuit Technology* also sells some OTS "flex circuits", and a "prototyper's lab kit" containing a variety of different flexible circuits can be purchased for US$99. "Flex cable" products manufactured by companies such as Amp and Parlex are also available through suppliers such as Digi-Key[48].

Round-Conductor Ribbon Cable

Phoenix Wire [49] manufactures a wide range of miniature TFE-Teflon-insulated wires that are available as flat or twisted multi-conductor cables. *Gore* manufactures a similar 32 AWG PTFE-insulated ribbon cable. The stranded conductors are very flexible, and the insulation offers good flexibility and immunity to chemicals and high temperatures (up to 260 °C). However, the it is still relatively stiff.

Temp-Flex Cable manufactures flexible ribbon cable with conductors as small as 46 AWG, and insulation materials such as FEP and PFA. Although the tiny 46 AWG cable is much lighter and less stiff than all other products seen, its conductor size limits its current-carrying capacity, making it impractical for wiring the flotor of the slave manipulator. The stiffness of the larger-gauge cables is simliar to that of Teflon. Furthermore, the insulation material is only rated to 105 °C.

Calmont Engineering & Electronics Corp. [50] manufactures a silicone-jacketed ribbon cable composed of 34 AWG stranded (40/50) bare copper conductors. Its silicone insulation and stranded conductors make it flexible and very limp even in tight bends,

and the insulation is stable to high temperatures (up to 150 °C). Since the cable is only available in large quantities, a sample length was purchased at considerable expense. This cable was used for the umbilical cables linking the flotor coils and LEDs, force/torque sensor, and microgripper to the stator.

Force/Torque Sensor Wiring

The ATI nano-transducer was purchased without the standard bulky connector and cable, so that it could be wired with the more flexible silicone-jacketed cable. Unfortunately, the eighteen 32 AWG enamel-coated wires leaving the transducer were bent to a sharp 90° angle to accomodate the standard connector and cable assembly. Therefore, a collar made from PVC plastic was constructed to protect the delicate wires.

Figure C.1 and Table C.1 describe the wiring that was performed at the transducer, as well as the connection of the transducer to the ATI multiplexer (MUX) box. In order to simplify wiring, all V+ wires were bussed together and all ground wires were bussed together, both at the transducer and at the MUX box. Specifics regarding the wiring and operation of the force/torque sensing system are provided in [51].

Interface to XVME-200

The ATI force/torque sensor is typically sold with a standard RS-232 serial interface. With six-axis force/torque measurements transmitted in binary format at 38.4 kbaud, the speed of I/O is limited to 369 Hz:

$$(6\ axes \times 2\ bytes/axis) + (1\ byte\ error\ flag) = 13\ bytes \tag{C.38}$$

$$13\ bytes \times 8\ bits/byte\ \div\ 38.4k\ bits/second = 2.7\ ms \Longrightarrow 369\ Hz \tag{C.39}$$

Table C.1: Wiring of the ATI Nano-Transducer

ATI Nano-Transducer				*ATI MUX box*
Group	*Description*	*Wire Colour*	*Stripe Colour*	*Wire Colour*
1T	V+	Red	—	Red
	Ground	Dark Green	—	Black
	Signal	Copper	Gold	White
1S	V+	Red	—	Red
	Ground	Yellow	—	Yellow
	Signal	Light Green	Silver	Green
2T	V+	Red	—	Red
	Ground	Dark Green	—	Black
	Signal	Copper	Black	White
2S	V+	Red	—	Red
	Ground	Yellow	—	Yellow
	Signal	Light Green	Green	Green
3T	V+	Red	—	Red
	Ground	Dark Green	—	Black
	Signal	Copper	Blue	White
3S	V+	Red	—	Red
	Ground	Yellow	—	Yellow
	Signal	Light Green	Violet	Green

Therefore, the ATI interface box was purchased with the additional parallel interface option. This interface provides faster I/O speeds since 16 bits (two bytes) are transmitted in parallel. At maximum speed ("fast" mode), the parallel interface should be capable of transmitting six-axis data at a rate of 7.07 kHz:

$$(6\ axes \times 2\ bytes/axis) + (2\text{-}byte\ error\ flag) = 7\ 2\text{-}byte\ words \tag{C.40}$$

$$7\ words \times 20.2\ \mu s/word = 141.4\ \mu s \Longrightarrow 7.07\ kHz \tag{C.41}$$

The *Xycom* XVME-200 digital I/O (DIO) board was used to provide an interface between the ATI parallel interface and the VME-bus CPUrunning VxWorks. Tables C.2

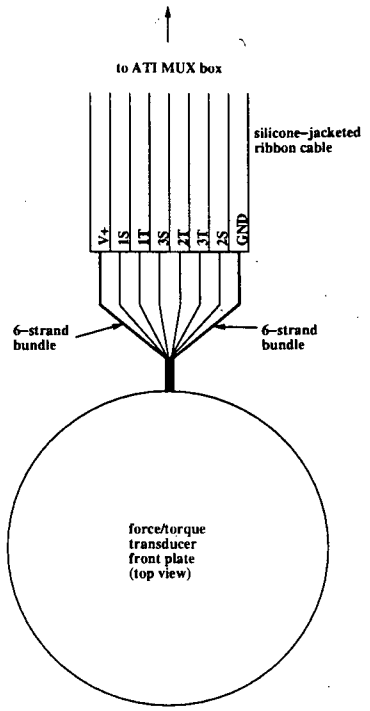

Figure C.1: Top view of ATI nano-transducer front plate, wires, and cable

and C.3 describe the wiring between the XVME-200 and the ATI interface.

Table C.2: Wiring of the XVME-200 (Input) to the ATI Parallel Interface (Output)

XVME-200			*ATI Parallel Interface*			
			Automatic Handshake		*Manual Handshake*	
Connector	*Pin*	*Description*	*Pin*	*Description*	*Pin*	*Description*
JK1	1	N/C	—		—	
	2	Ground	1	Ground	1	Ground
	3	H4 out-1	49	IBF	—	
	4	Ground	1	Ground	1	Ground
	5	H2 out-1	—		—	
	6	Ground	1	Ground	1	Ground
	7	TMR out-1	—		—	
	8	Ground	1	Ground	1	Ground
	9	H2 in-1	—		—	
	10	Ground	1	Ground	1	Ground
	11	H3 in-1	50	$\overline{\text{STB}}$	50	$\overline{\text{STB}}$
	12	Ground	1	Ground	1	Ground
	13	H1 in-1	—		—	
	14	Ground	1	Ground	1	Ground
	15	TMR in-1	—		—	
	16	Ground	1	Ground	1	Ground
	17	PB7-1	10	Output bit 15	10	Output bit 15
	18	Ground	1	Ground	1	Ground
	19	PB6-1	9	Output bit 14	9	Output bit 14
	20	Ground	1	Ground	1	Ground
	21	PB5-1	8	Output bit 13	8	Output bit 13
	22	Ground	1	Ground	1	Ground
	23	PB4-1	7	Output bit 12	7	Output bit 12
	24	Ground	1	Ground	1	Ground
	25	PB3-1	6	Output bit 11	6	Output bit 11

Table C.2: Continued

XVME-200			*ATI Parallel Interface*			
			Automatic Handshake		*Manual Handshake*	
Connector	*Pin*	*Description*	*Pin*	*Description*	*Pin*	*Description*
JK1	26	Ground	1	Ground	1	Ground
	27	PB2-1	5	Output bit 10	5	Output bit 10
	28	Ground	1	Ground	1	Ground
	29	PB1-1	4	Output bit 9	4	Output bit 9
	30	Ground	1	Ground	1	Ground
	31	PB0-1	3	Output bit 8	3	Output bit 8
	32	Ground	1	Ground	1	Ground
	33	PA7-1	39	Output bit 7	39	Output bit 7
	34	Ground	1	Ground	1	Ground
	35	PA6-1	40	Output bit 6	40	Output bit 6
	36	Ground	1	Ground	1	Ground
	37	PA5-1	41	Output bit 5	41	Output bit 5
	38	Ground	1	Ground	1	Ground
	39	PA4-1	42	Output bit 4	42	Output bit 4
	40	Ground	1	Ground	1	Ground
	41	PA3-1	43	Output bit 3	43	Output bit 3
	42	Ground	1	Ground	1	Ground
	43	PA2-1	44	Output bit 2	44	Output bit 2
	44	Ground	1	Ground	1	Ground
	45	PA1-1	45	Output bit 1	45	Output bit 1
	46	Ground	1	Ground	1	Ground
	47	PA0-1	46	Output bit 0	46	Output bit 0
	48	Ground	1	Ground	1	Ground
	49	N/C	—		—	
	50	Ground	1	Ground	1	Ground

Table C.3: Wiring of the XVME-200 (Output) to the ATI Parallel Interface (Input)

XVME-200			*ATI Parallel Interface*			
			Automatic Handshake		*Manual Handshake*	
Connector	*Pin*	*Description*	*Pin*	*Description*	*Pin*	*Description*
JK2	1	N/C	—		—	
	2	Ground	1	Ground	1	Ground
	3	H4 out-2	19	$\overline{\text{OBF}}$	19	$\overline{\text{OBF}}$
	4	Ground	1	Ground	1	Ground
	5	H2 out-2	—		—	
	6	Ground	1	Ground	1	Ground
	7	TMR out-2	—		—	
	8	Ground	1	Ground	1	Ground
	9	H2 in-2	—		—	
	10	Ground	1	Ground	1	Ground
	11	H3 in-2	20	$\overline{\text{ACK}}$	20	$\overline{\text{ACK}}$
	12	Ground	1	Ground	1	Ground
	13	H1 in-2	—		—	
	14	Ground	1	Ground	1	Ground
	15	TMR in-2	—		—	
	16	Ground	1	Ground	1	Ground
	17	PB7-2	18	Input bit 15	—	
	18	Ground	1	Ground	1	Ground
	19	PB6-2	17	Input bit 14	—	
	20	Ground	1	Ground	1	Ground
	21	PB5-2	16	Input bit 13	—	
	22	Ground	1	Ground	1	Ground
	23	PB4-2	15	Input bit 12	—	
	24	Ground	1	Ground	1	Ground
	25	PB3-2	14	Input bit 11	—	

Table C.3: Continued

XVME-200			*ATI Parallel Interface*			
			Automatic Handshake		*Manual Handshake*	
Connector	*Pin*	*Description*	*Pin*	*Description*	*Pin*	*Description*
JK2	26	Ground	1	Ground	1	Ground
	27	PB2-2	13	Input bit 10	—	
	28	Ground	1	Ground	1	Ground
	29	PB1-2	12	Input bit 9	—	
	30	Ground	1	Ground	1	Ground
	31	PB0-2	11	Input bit 8	49	IBF
	32	Ground	1	Ground	1	Ground
	33	PA7-2	31	Input bit 7	31	Input bit 7
	34	Ground	1	Ground	1	Ground
	35	PA6-2	32	Input bit 6	32	Input bit 6
	36	Ground	1	Ground	1	Ground
	37	PA5-2	33	Input bit 5	33	Input bit 5
	38	Ground	1	Ground	1	Ground
	39	PA4-2	34	Input bit 4	34	Input bit 4
	40	Ground	1	Ground	1	Ground
	41	PA3-2	35	Input bit 3	35	Input bit 3
	42	Ground	1	Ground	1	Ground
	43	PA2-2	36	Input bit 2	36	Input bit 2
	44	Ground	1	Ground	1	Ground
	45	PA1-2	37	Input bit 1	37	Input bit 1
	46	Ground	1	Ground	1	Ground
	47	PA0-2	38	Input bit 0	38	Input bit 0
	48	Ground	1	Ground	1	Ground
	49	N/C	—		—	
	50	Ground	1	Ground	1	Ground

Device Driver

A set of library routines was written to handle communication between the XVME-200 and the ATI interface under VxWorks. The procedures enable the caller to send commands, as well as receive sensor data using an interrupt-driven routine. All code resides in the directory shyank/proj/xvme200.

The routines rely on a modified version of a VxWorks XVME-200 device driver (originally written by Alison Taylor). Details regarding the operation of the XVME-200 can be found in [52] and [53]. Initially, the device driver was altered to support 16-bit double-buffered input with automatic interlocked input handshaking through PI/T 1 (Mode 1, Port A Submode XX, Port B Submode X0), and 16-bit double-buffered output with automatic interlocked output handshaking through PI/T 2 (Mode 1, Port A Submode XX, Port B Submode X1).

In these modes of operation, there were no problems with data transfer and output handshaking from the XVME-200 to the ATI. However, the input handshaking performed by the XVME-200 did not perform predictably. The general sequence of events while reading data should proceed as follows:

1. The ATI parallel interface presents data to the input port of the XVME-200;
2. The ATI parallel interface asserts the $\overline{\text{STB}}$ line, indicating that data is ready to be read;
3. The data is read from the port, triggering the automatic generation of a handshake pulse at the H4 line of the XVME-200;
4. The handshake pulse is held for t_{ibf}, then lowered.

In order to meet the timing requirements of the ATI parallel interface, the IBF handshake pulse must have a minimum width of 0.12 μs (t_{ibf}), and the time from $\overline{\text{STB}}$ assertion

to IBF lowering (t_{sir}) must not be less than 0.8 μs [51]. Using an oscilloscope, it was observed that t_{ibf} was not consistent, occasionally violating the minimum timing requirement for t_{sir}. This usually occurred at the beginning of a sequence of data transmitted from the ATI interface to the XVME-200. Since this issue could not be resolved, the automatic handshaking using the H4 line was bypassed, and handshaking was performed manually. Manual handshaking required an output line; however, no extra output lines were available.

Fortunately, the ATI parallel interface reads data 16-bits at a time, but always expects the most significant byte to be zero. Therefore, the input lines corresponding to the most significant byte of the ATI were tied to logical ground. PI/T 2 of the XVME-200 was reconfigured to provide 8-bit double-buffered output with automatic interlocked output handshaking (Mode 0, Port A Submode 01), and 8-bit double-buffered output with no handshaking (Mode 0, Port B Submode 01). The least significant bit (LSB) of Port B was connected to the IBF line of the ATI for manual handshaking, and the remaining seven Port B output lines were not used. The sofware was altered to support manual handshaking. The resulting wiring change is included in Tables C.2 and C.3.

Using manual handshaking and the library routines described above executing on a SPARC 1-e CPU, a maximum sampling rate of 1 kHz was achieved for 6-axis force/torque measurements. Each sampling cycle involved sending a "fast output" command (^N) to the ATI parallel interface, and then receiving the resulting 14-byte data in binary form.